9-18-2017 12:15 PM

Numerical Simulations of Two-Phase Flows in the Liquid Solid Circulating Fluidized Bed

Hao Luo, *The University of Western Ontario*

Supervisor: Chao Zhang, *The University of Western Ontario*
Co-Supervisor: Jesse Zhu, *The University of Western Ontario*
A thesis submitted in partial fulfillment of the requirements for the Master of Engineering
Science degree in Mechanical and Materials Engineering
© Hao Luo 2017

Abstract

The liquid-solid circulating fluidized bed (LSCFB) has many potential applications in biochemical and petroleum industries, as well as in wastewater treatments, given its higher contact efficiency and being able to accommodate two reactions under one system. With extensive experimental results becoming available, there is clearly a need for computational fluid dynamics (CFD) modeling to expand our understandings of LSCFBs and to predict the hydrodynamic behaviors of the two-phase flows within LSCFB.

In this research, the Eulerian-Eulerian two-phase model combined with the kinetic theory for the granular phase is applied to simulate the two-phase flows in LSCFBs. The key factors affecting the simulation results including the drag model, near wall treatment and boundary condition are investigated and the CFD model is validated by comparing the numerical results with the experimental data. Then, the hydrodynamics of LSCFBs under different operating conditions are investigated numerically.

Among the seven different drag models examined in this study, the adjusted Syamlal O'Brien drag model and the irregular particle drag model were found to provide the best numerical solutions for spherical and irregular particles, respectively. For the three different near wall treatments tested, the Menter-Lechner near wall treatment was found to provide the best predictions for the near wall region. It is also found that the numerical results are insensitive to the restitution and specularity coefficients, which are used in the boundary conditions for the solid phase. In addition, the proposed CFD model with the best drag model and near wall treatment is applied to simulate the two-phase flows in LSCFBs under different operating conditions, including different superficial liquid velocities, superficial solid velocities and particle densities. The numerical predictions show correct trends and good agreements with the experimental data.

Keywords

Acknowledgments

I will like to take this opportunity to express the gratitude and appreciation to those who have always been helping and supporting me in the whole period of master's study.

Firstly, my sincerest gratitude is to my supervisors Profs. Zhang and Zhu, who believed my potential and provided generous advice, encouragement and support throughout my research. I attribute the thesis to their guidance which ensured the successful fulfilment of this study.

Then, my gratefulness is from all the members from research groups of Profs. Zhang and Zhu, especially Zeneng Sun, Huirui Han, Yunfeng Liu and Tian Nan for their help and friendship in both academic and daily life.

Finally, great gratitude is to my parents for their consistent and unreserved support throughout the entire process.

Table of Contents

List of Tables

List of Figures

List of Appendices

Nomenclature

Notation

Ap   Cross-sectional area of a particle (m^2)

Ar   Archimedes number

$C_{1\varepsilon}$ Constants

$C_{2\varepsilon}$ Constants

C_D Drag coefficient, dimensionless

d_p Mean particle diameter, m

D Riser diameter, m

H Riser height, m

e Specularity coefficient, dimensionless

e_{sw} Restitution coefficient for particle-wall collisions', dimensionless

g Acceleration due to gravity, m/s^2

g_o Radial distribution function, dimensionless

k Turbulent kinetic energy, m^2/s^2

K_{sl} Interphase momentum exchange coefficient, $kg/m^3 s$

P_s Solids pressure, Pa

P Fluid pressure, Pa

R_e Reynolds number, dimensionless

t Time, s

U_t Particle terminal velocity, m/s

U_l Superficial liquid velocity, m/s

U_s Superficial solid velocity, m/s

v Velocity, m/s

Greek letters

α_s local solids volume fraction, dimensionless

ε Turbulent energy dissipation rate, m^2/s^3

$k_{\Theta s}$ Granular conductivity, $kg/m^3 s$

ϕ_{ls} Interphase energy exchange, kg/ms^3

γ_Θ Collisional energy dissipation rate, kg/ms^3

λ Solids bulk viscosity, kg m/s

μ Viscosity, kg/m-s

υ Kinematic viscosity, m^2/s

Θ Granular temperature, m^2/s^2

ρ Density, kg/m^3

$\sigma_k, \sigma_\varepsilon$	Constants		ψ	Shape factor
τ	Shear stress, kg/s^2			

Subscripts

l	Liquid phase		a	Auxiliary
s	Solid phase		mf	Minimum fluidization
f	Fluid		t	Terminal

Chapter 1

1   General Introduction

1.1   Background

Fluidization is characterized as a process in which solid particles are suspended in a moving fluid and converted from the solid-like state to the fluid-like state. With the characterization of higher fluid-solid contact efficiency, better fluid-solid and solid-solid mixing, the fluidization has been widely applied in various industries, including the wastewater treatment, biochemical technology, petrochemical and metallurgical industries.

Based on the characterization of the fluid media, fluidization can be cataloged as gas-solid fluidization, liquid-solid fluidization and gas-liquid-solid fluidization. Liquid-solid fluidization can be divided into four regimes, the fixed bed regime, the conventional fluidization regime, the circulating fluidization regime and the dilute transport regime. When a liquid stream is introduced from the bottom of a bed with solid particles, it will pass through the bed via the spaces between static particles. If the liquid velocity is low which cannot balance the weight of particles, particles tend to stay static at the bottom of the bed, which is called the fixed bed regime. With the increase of the liquid velocity, the drag force acting on particles increases correspondingly and gradually counteracts the effect of gravity. When the fluid velocity reaches the minimum fluidization velocity, U_{mf}, where the drag force, gravity and buoyancy force reach balance, particles start suspending in the fluid and transforming to fluid-like state. Indicating the start of the conventional fluidization regime where the particles are not entrained out of the bed. With further increase in the fluid velocity, so as the drag force, the fluidization becomes more intense and particles are moving upward along with the bed expansion. Finally, it reaches the circulating fluidization regime where most particles can be entrained out of the bed and need to be recirculated back to the bottom of the bed. Further increasing the liquid velocity, the bed goes into the dilute liquid transport regime.

The conventional fluidization regime has been studied extensively by lots of researchers. In terms of the flow structures, a clear boundary between the dense region with a higher solid concentration at the bottom of the bed and the freeboard region with a lower solids

concentration at the top of the bed can be widely observed in experiments, and with the increase in the liquid flow rate, the boundary raises with the expansion of the bed. In 1985, Couderc [1] found the conventional fluidization can be considered as a dispersed homogenous fluidization where particles are uniformly distributed in both the axial and radial directions in the dense region. As for the mathematical models describing the flow characteristics, Richardson and Zaki [2] proposed an important relationship between the operating liquid velocity and the bed voidage, which has been widely adopted and modified for the drag correlation between the liquid and particles.

Due to the restricted operating range and back-mixing problems of the conventional fluidization, the circulating fluidized bed (CFB) was proposed in late 1960s. The gas-solid circulating fluidized bed (GSCFB) has been extensively studied, it was found the back-mixing phenomenon in GSCFBs can be significantly reduced [3] and the contact efficiency is also increased due to the increased slip velocity between the two phases [4]. However, compared to GSCFBs, only in recent years, the liquid-solid circulating fluidized bed (LSCFB) has gained more attention. The studies of hydrodynamics in LSCFBs have been mostly carried out at Tsinghua University [5-9] and University of Western Ontario [10-13].

In LSCFBs, all particles can be entrained out of the bed with the high liquid velocity, which is usually higher than the particle terminal velocity. Hence, it is essential to feed particles at the bottom of the fluidized bed continuously, which is normally done by feeding new particles or recirculating the entrained particles back to the bottom of the bed. The schematic of a typical LSCFB is shown in Fig 1.1, which comprises of a riser, a downer, a liquid-solid separator, a top solid-return pipe and a bottom solid-feed pipe [14]. The particles are injected from the solids feed pipe, due to the auxiliary liquid and primary liquid, the particles are moving upward and entrained out of the riser, then separated from liquid in the liquid-solid separator and ejected into the downer, finally reach to the solids feed pipe again and complete one circulation.
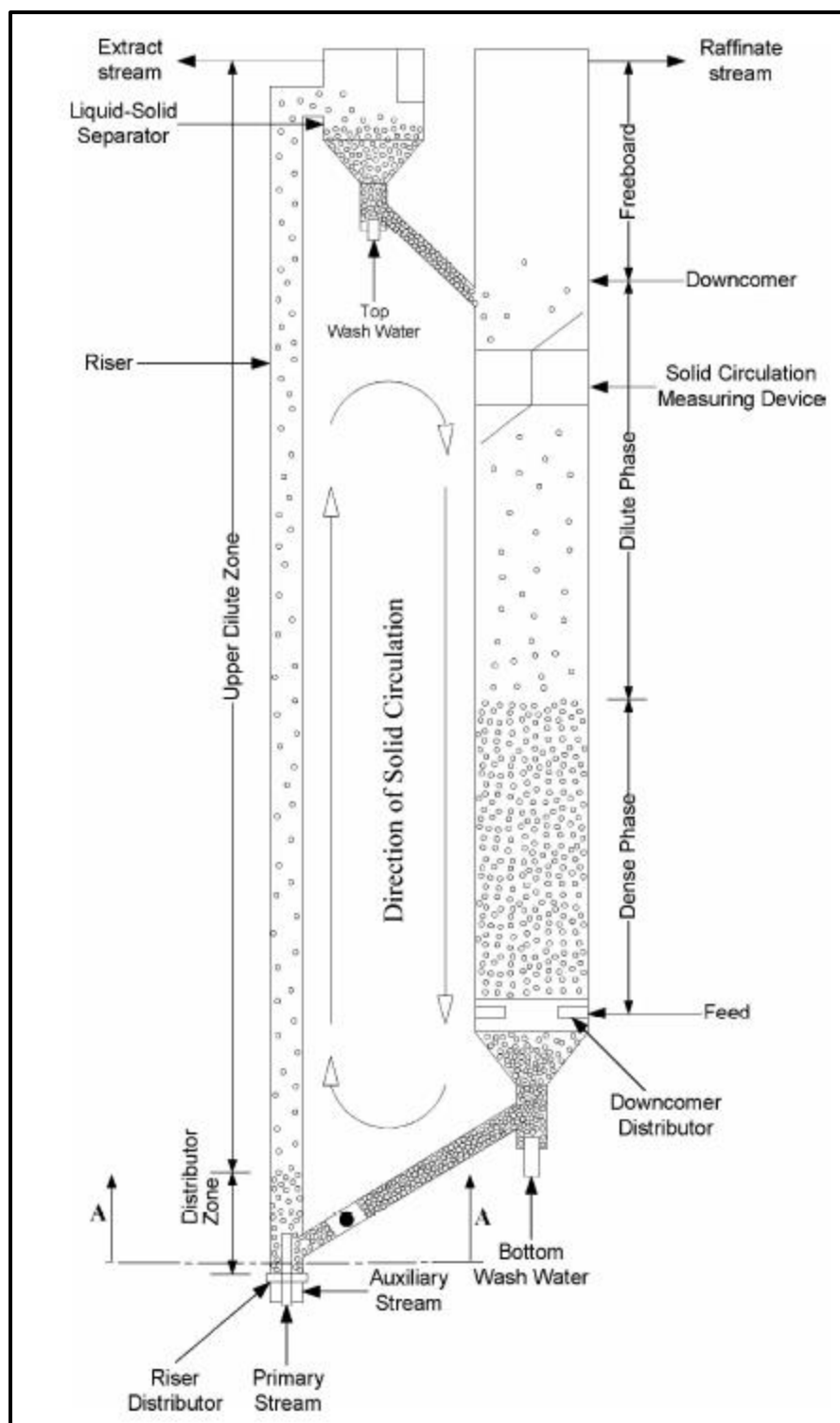
Figure 1.1: Schematic diagram of a liquid-solid circulating fluidized bed

To properly design a LSCFB system for industrial applications, it is necessary to understand the hydrodynamics of the LSCFB system. Liang and Zhu [9], Kuramoto [15], Zheng [10] and Razzak [16] have reported that the flow structure is almost uniform in the axial direction of LSCFBs for all types of particles, which is different from the conventional liquid-solid fluidized beds where exits a boundary between the bottom dense region and the top freeboard region. In addition, Liang et al. [8], Zheng [12], Razzak [16] and Sang [13] observed the non-uniformity of the flow structure in the radial direction of LSCFBs for different particles and operating conditions, which is different from the uniform distribution in conventional liquid-solid fluidized beds.

Modeling on the fluidized beds has become a new tool to investigate and scale up the complex flow structures. Starting from the 1950s, a series of mathematical models have been proposed, such as the two-phase model for the conventional fluidized beds and the core-annulus model for the circulating fluidized beds. However, those models cannot correctly and comprehensively solve the flow field of a complex system in fluidized beds. Hence, with fast development of computational techniques, computational fluid dynamics (CFD) has become a more reliable and effective way to simulate a complex flow system.

The literature review of recent research on the hydrodynamics of LSCFBs and CFD techniques are presented in next section, along with the gaps and some discrepancies, which leads to the objectives and thesis structure of this research work.

1.2   Literature review

The literature review section is conducted in two areas, (1) past experimental studies on the hydrodynamics of the LSCFB system and (2) the relevant CFD models for the multi-phase flow simulations.

1.2.1   Hydrodynamic characteristics of LSCFBs

Plenty of experimental studies have been conducted on the conventional liquid-solid fluidized bed since 1950s. As mentioned before, it is generally accepted that the liquid-solid fluidization is a uniformly dispersed homogeneous fluidization along both axial and radial directions under low liquid velocity [1]. In other words, the particles are distributed uniformly along the radial

and axial directions. This homogeneous fluidization phenomenon was first brought by Richardson and Zaki [2] along with the important correlation between the operating liquid velocity and the bed voidage, which is used as the basis of the liquid-solid fluidization theory. Later, many researchers have confirmed the homogeneous fluidization under all liquid-solid fluidized systems where the liquid velocity is lower than the particle terminal velocity [17-19].

Few works have been concentrated on the liquid-solid fluidization system under high liquid velocity. Zheng [10] reported there are two distinct regimes for circulating fluidization under a settled auxiliary liquid flow rate: (1) the initial zone where solids circulation rate increases significantly with the increase in the liquid flowrate and (2) the fully developed zone in which the solids circulation rate increases insignificantly with the increase in the liquid flowrate.

Liang and Zhu [9] reported that the axial solids volume fraction distributions in LSCFBs are uniform under different superficial liquid velocities and particle circulation rates for two low-density particles. Later, Zheng [10] extended the experimental studies to heavy particles and it was found that the axial solids volume fraction distribution is non-uniform for heavy particles as shown in Figure 1.2, but the overall flow structures in LSCFBs are still more uniform than GSCFBs. In addition, it was also found that a higher liquid velocity and longer transition regime are required for heavy particles when transiting from the conventional fluidization regime to the circulating fluidization regime. Razzak [16] investigated the influence of the particle diameter and shape on the behaviors of LSCFBs, it is shown in Figure 1.3 that the axial solids holdup distribution is almost uniform expect at the region near the distributor, while the overall cross-sectional average solid holdup increases with the increase in the particle diameter and the superficial solid velocity regardless of particle shapes.
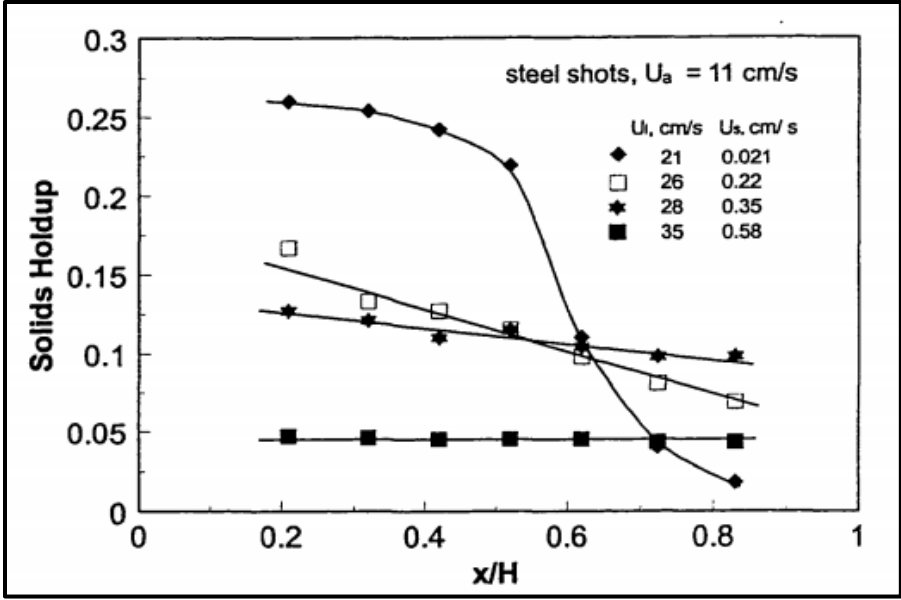
Figure 1.2: Axial distributions of the solids holdup in the LSCFB for steel shots under different superficial liquid velocities (Zheng et al., 1999)
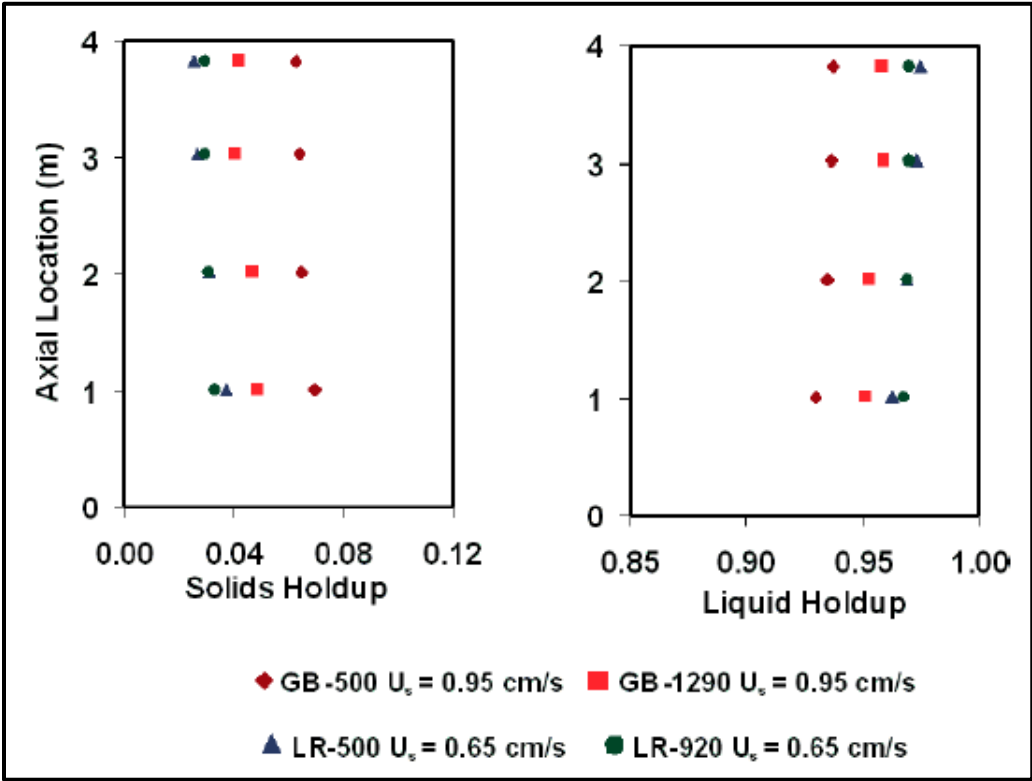
Figure 1.3: Axial profiles of the average cross-sectional solids and liquid holdup at U_l=22.4 cm/s (Razzak, 2009)

For the radial directions, Liang et al. [8] and Roy et al. [20] showed the non-uniform radial distribution of the solid holdup in the LSCFBs, i.e., it is lower at the central region while higher near the wall. Later, Zheng [12] conducted the experimental studies under different operating conditions and particle properties, it can be seen from Fig 1.4 that the radial nonuniformity decreases with the increase of the superficial liquid velocity and increases with the increase of the superficial solid velocity. Furthermore, more uniform distribution along the radius is observed for systems where lighter particles are used under the same cross-sectional average solids concentration. Later, the above phenomena were examined by Razzak [16] and the investigations were extended to different particle diameters and shapes. In terms of the particle size, it was reported the radial nonuniformity and local solid concentration are higher for smaller particles under the same operating conditions. In addition, by increasing the superficial solid velocity, the radial nonuniformity increases and the rate of the increase in the radial nonuniformity is higher for smaller particles. In terms of the particle shape, Razzak [16] observed the solids holdup of spherical glass beads is higher than irregular lava rocks, which is due to the reduction in the drag coefficient caused by the irregular shape of the particles. Sang [13] later investigated the effects of the particle density, size and sphericity on the hydrodynamic behaviors in LSCFBs and introduced a new criterion, the excess superficial liquid velocity $(U_l - U_t)$, which can give a better indication for the influence of the particle properties on the performance of the LSCFBs. Then, a mathematical expression was proposed [13] to predict the solids holdup and slip velocity in the circulating fluidization regime.
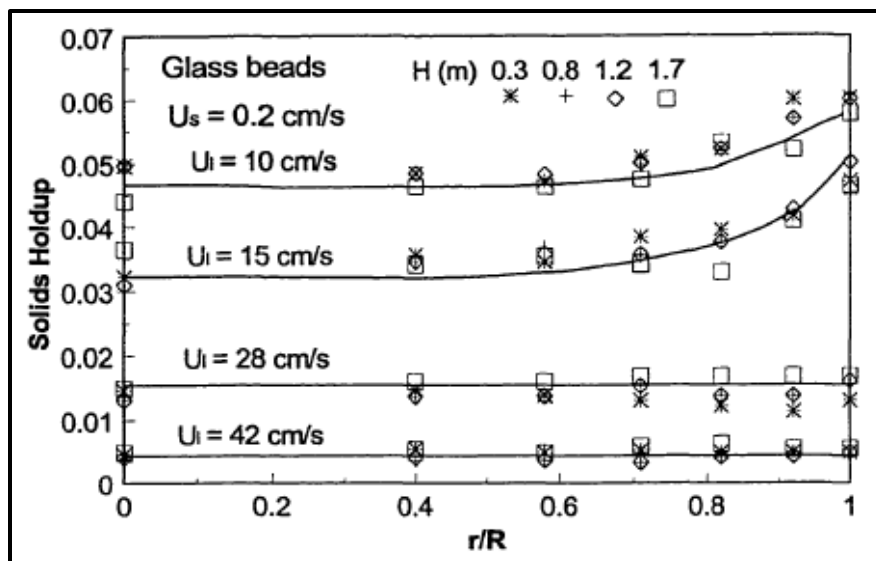
(a)
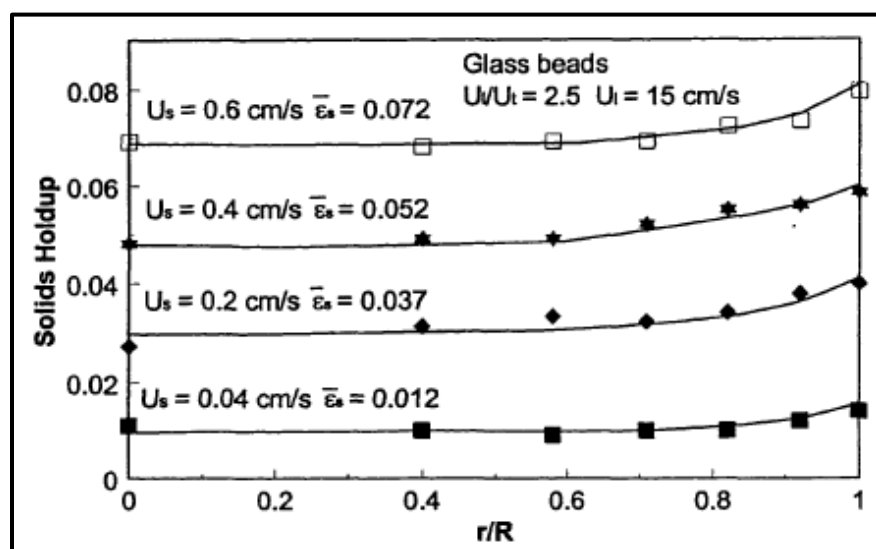
(b)

Figure 1.4: Radial profiles of the solids concentration at H=0.8m (Zheng et al., 2001)

(a) at different superficial liquid velocities and (b) at different solids flow rate
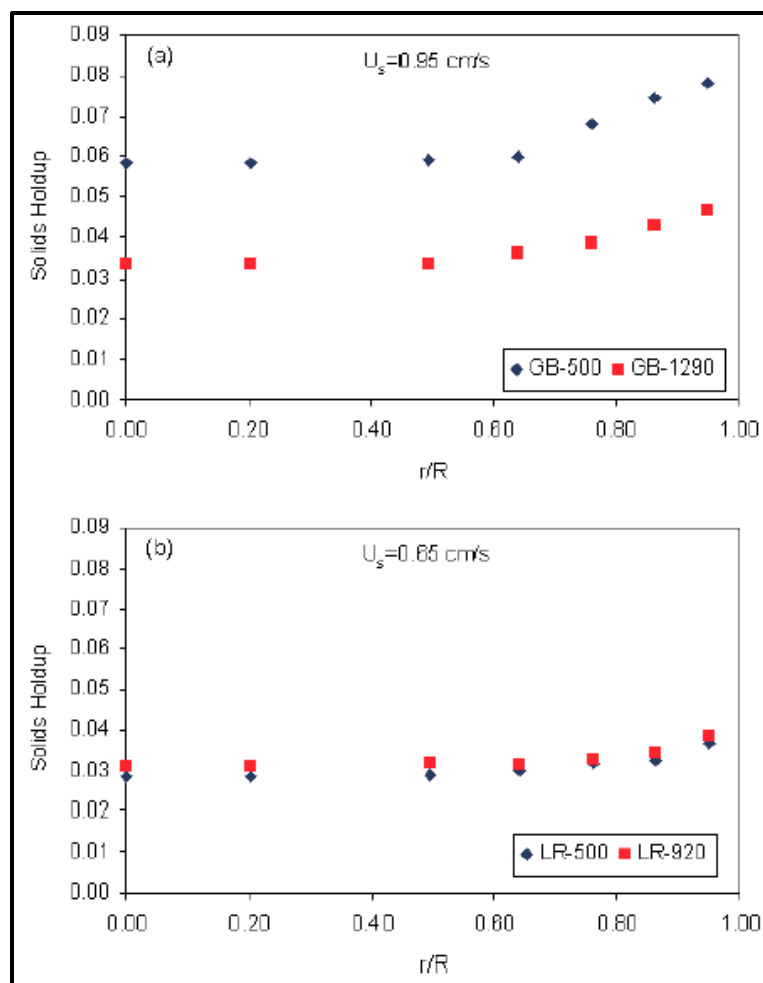
Figure 1.5: Comparison of the radial distributions of the solids holdup between glass beads and lava rock particles at H=2.02 m and U_p=22.4 cm/s (Razzak, 2009)

Although there are some radial or axial nonuniformities exist in LSCFBs under some operating conditions, the flow structures in liquid-solid circulating fluidized beds are more homogeneous than the distributions in gas-solid circulating fluidized beds.

1.2.2   Theory of the modeling of multi-phase flows in fluidized beds

In recent years, the computational fluid dynamics (CFD) modeling has become an effective tool to investigate the hydrodynamics in a CFB riser due to the fast development of computer technology and multiphase flow models [21-24]. Generally, there are two major theories of describing gas-solid and liquid-solid two-phase flows: (1) the Eulerian-Lagrangian (E-L) approach where the particulate trajectory model is used for the solid-phase and the particle-

particle interactions are neglected and (2) the Eulerian-Eulerian (E-E) approach where two-fluid model is used for both phases. In this work, the Eulerian-Eulerian approach is employed since the solid volume fraction in LSCFBs is high and the interactions between particles need to be considered.

The Eulerian two-phase flow theory was developed by Ishii [25], Delhaye and Achard [26], Boure and Delhaye [27], Soo [28], Dre and Lahey [29] and He and Simonin [30]. The general idea of Eulerian-Eulerian approach is to consider the fluid and solid phases as the interpenetrating continuum, and solve the mass and momentum governing equations which are closed by the constitutive equations within a fixed control volume containing both phases [31]. Furthermore, the liquid phase is closed by a turbulence model and the solid pressure, viscosity and solid phase stress tensor are described by the kinetic theory of granular phase (KTGP). By applying the E-E approach, a series of investigations and evaluations for multi-phase flows have been conducted in recent years.

Several turbulence models that are used to close the Reynolds-averaged Navier-Stokes equations for the fluid phase have been developed to represent the Reynolds stresses and can be cataloged into four groups.

(1) The zero-equation turbulence model. This model is developed from a simple algebraic equation proposed by Van Driest [32] to close the governing equations instead of using PDE to describe the turbulent stresses and fluxes. Then, Cebeci and Simth [33], and Baldwin and Lomax [34] refined and improved the model from Van Driest [32].

(2) The one-equation turbulence model. Based on the Boussinesq hypothesis [35] which relates the Reynolds stresses with the mean velocity gradients, the Spalart-Allmaras model [36] was developed to solve the turbulence kinetic energy k.

(3) The two-equation turbulence model. On the base of the one-equation turbulence model, the two-equation models, such as the k-ε and k–ω models, were proposed where two additional equations are solved for the turbulence kinetic energy k, and the turbulence dissipation rate ε in the k-ε turbulence model or the specific dissipation rate ω in the k–ω turbulence model.

(4) The Reynolds stress model (RSM). This turbulence model abandons the isotropic eddy-viscosity hypothesis and closes the Reynolds-averaged Navier-Stokes equations by solving transport equations for the six Reynolds stresses, together with an equation for the dissipation rate [37].

After decades of developments, the k-ε and k–ω turbulence models have become the most popular ones. With the characteristics of robustness, economy and reasonable accuracy for various turbulent flows, the k-ε turbulence model is widely used in industrial applications. Since the standard k-ε turbulence model is for high Reynolds number flows, it is necessary to modify it for flows in low Reynolds number regions or use wall functions near the wall. Correspondingly, the k–ω turbulence model, which accounts for the effects of low Reynolds number flows, compressibility and shear flow spreading, performs better for swirling flows and flows in the near wall region, but with the disadvantages of less range of applications and over predicting separations as well. As for the RSM model, it is much more computational expensive and mostly used to solve the flow with anisotropic turbulence such as highly swirling flows and stress-driven secondary flows [37].

For the kinetic theory of granular phase, to model the kinetic and collisional transport of particles while representing granular phase as interpenetrating continuum with fluid, the KTGP was developed in 1980s. It started from the collisional particle interactions of dense fluid flow which was presented by Chapman and Cowling [38] and has been widely applied in multiphase flow simulations, such as the works by Lun et al. [39], Ding and Gidaspow [24]. By analogizing the thermodynamic temperature of fluid, the granular temperature for solid particles was introduced, which is associated with the fluctuating velocity of solid particles. Thus, the solids viscosity and pressure can be determined by the granular temperature and the constitutive equation of the solid momentum equation can be closed by solids stress tensor. Furthermore, when dense gas molecules interact, the collisions are nearly elastic. However, for the particles which are a few orders larger than molecules, they will suffer a loss of momentum during collisions. Therefore, the restitution coefficient is introduced to describe the inelasticity of the collisions.

Within the Eulerian-Eulerian multiphase model, the interactions between particles and fluid is a dominate factor that should be considered. The dynamic balance of particles within a fluid depends on the drag, gravity and buoyancy forces. Hence, it is essential to have a drag model that is suitable for particle fluidization processes under different conditions, including different properties of solids and fluid, Reynolds number, volume fraction, etc., which has become the key challenge in multiphase flow simulations [40]. During the past decades, starting from the easiest single particle drag correlations [41] to the complex semi-empirical multi-particle drag models, researchers have proposed three approaches. The first approach is by correlating the pressure loss (drag force on a particle) with the voidage of the packed bed fluidization regime, such as the Ergun equation [42]. Then Gibilaro [43] extended its applicability to the dilute particle systems by relating the energy dissipation in the bed with the unrecoverable pressure loss, and hence obtained an expression of particle drag force under the fully expanded limit condition. The second approach is by correlating the slip velocity between the particle and liquid, with the bed voidage for different fluidized bed regimes, such as Richardson-Zaki [2], Garside and Al-Dibouni [44] and Wen-Yu [45]. Then Syamlal-O'Brien [46] obtained the drag model for the multi-particle system from a single particle drag correlation by non-dimensional analysis. The third approach is EMMS, which is based on the energy minimization multi-scale method. Beside the above three methods, Gidaspow [47] combined the first method (Ergun equation) and the second method (Wen-Yu) to obtain the drag coefficients on the dense fluidization regime ($\varepsilon<0.8$) and dilute fluidization regime ($\varepsilon>0.8$) respectively. Then, Huilin-Gidaspow [48] improved the discontinuity of the Gidaspow drag model [47] by introducing a blending function. Furthermore, since some operating conditions are significantly different from the original experimental conditions that Syamlal and O'Brien considered when deriving their drag model [46], the Syamal-O'Brien model can be adjusted by matching the predicted minimum fluidization velocity with the experimental data. It is called the adjusted Syamlal-O'Brien drag model [49].

Beside the drag model, in the near wall region of CFBs, due to the considerable influence of walls on turbulent flows, an accurate representation of the flow in the near wall region should be adopted to ensure the numerical solutions of the wall-bounded flow are accurate. Generally, there are two approaches to model the flow in the near-wall region [37]. The first one is by adopting a semi-empirical function to represent the viscosity affected region instead of solving

turbulence equations, such as the standard wall functions and the scalable wall functions. The second one is by modifying the turbulence model to resolve the near wall region flows, such as the enhanced wall treatment and the Menter-Lechner near wall treatment [37]. The standard wall functions are based on the work of Launder and Spalding [50] and the scalable wall functions is based on the standard wall functions by adding a selector for Y*. As for the second approach, the enhanced wall treatment is based on the two-layer model with a blend function while the Menter-Lechner near wall treatment adds a source term in the transport equation of the turbulence kinetic energy and introduces new momentum equations [48].

For the particle-particle collisions, Gidaspow and Huilin [51] introduced the "effective restitution coefficient" which is near 1 to represent the near elastic collision brought by the liquid film between particles which attenuates the energy loss within particle collisions. Cheng [52] also claimed the "elastic collisions" phenomenon exists in LSCFBs and found there is only minor difference in radial distribution of liquid velocity and solids holdup while particle restitution coefficient varies from 0.96 to 0.99. On the one hand, the collision is related to the materials of particles, the glass beads which were used in the works by Gidaspow and Huilin [51] and Cheng [52] shows the particle restitution coefficient equals to 1.0, while Ehsani [53] indicated particle restitution coefficient=0.9 is more suitable for the rougher stainless steel spherical particles. On the other hand, the fluid materials have considerable influence on the particle-particle collisions within the fluid-solid suspension as well. For example, gas can hardly form a lubricant film between particles which eases the particle collisions and the existence of clusters can also significantly influence the particle collisions in gas-solid systems.

For the boundary conditions, interactions between fluid and wall for the wall bounded flow need to be considered as well. In most of fluid flows, no-slip condition is applied on the wall. However, for the particles flow in a fluidized bed, the no-slip condition at the wall is not applicable. Hence, the specified shear is required to set at the wall if the shear stress is known. Otherwise, the conception of specularity coefficient introduced by Johnson and Jackson [54] can be used, which represents the fraction of collisions that transfer momentum from the granular flows to the wall. When it approaches zero, it stands for the complete elastic collision and the condition is equivalent to zero shear at the wall, while it closes to unity indicates there exists significant amount of lateral momentum transfer.

In the industrial applications of fluidized beds, irregular particles are used sometimes which can significantly affect the hydrodynamics of the fluidized bed. Generally speaking, the more irregular particle shape is, the greater the drag will be. Therefore, it is important to investigate the influence of particle shape on the modeling. The irregular particles can be various kinds of shapes. Hence, it is essential to introduce shape factors to characterize irregular particles. Wadell [55] introduced the sphericity, which is the ratio of the surface area of a sphere of the same volume and the surface area of the particle, and the circularity, which stands for how close the projected area of the particle is a circle. Analogously, Heywood [56] suggested a volumetric shape factor, which is related to the diameter of a sphere with the same volume and the diameter of a circle of the same area as the projected area of the particle. Later, people proposed other indirect methods to describe the sphericity. Austin [57] determined the shape factor by the specific surface and the arithmetic average of passing and retaining sieve, McCulloch and Moser [58] defined the "dynamic shape factor", which is based on hydraulic properties of the irregular particle.

On the base of the conception of the shape factor, efforts are made to develop the drag models for irregular particles. Starting from the 1970s, simple drag correlations for particles with fixed shapes and flow directions have been derived. For example, Huner and Hussey [59] and Ui et al. [60] studied cylinders moving in the axial direction, and Shail and Norton [61] studied discs. Undoubtedly, some drag models are accurate for particles with certain shapes under certain flow conditions, but they are not accurate for other circumstances. Therefore, a universal drag correlation using shape factors for irregular particles will be essential and changeling. The attempts to develop the drag model for single non-spherical particles were made by Haider and Levenspiel [62], Ganser [63], Swamee and Ojha [64], Chien [65], Tran-Cong et al. [66]. Those empirical correlations are mainly based on experimental data. However, all those models were obtained based on single particle drag correlation, and they still need to be improved and modified for the multi-particle systems in fluidized beds. Therefore, Richardson and Zaki [2] included the volumetric shape factor in their velocity-voidage function under the limited condition of $\text{Re} > 500$ for relatively large particles ($d > 100 \mu m$) with irregular shapes. Cleasby and Fan [67] incorporated the "n" value from the RZ equation [2] with a function of shape factor obtained from the experimental data for irregular particles of sand, anthracite and

flints. Then Dharmarajah [68] proposed the relationship between the bed voidage, sphericity, and superficial liquid velocity by introducing complicated terms of modified Reynolds number and coefficient A1. However, this relationship is not suitable for bed voidage higher than 0.9.

Comparing to GSCFBs, less CFD studies have been carried out on LSCFBs. Since both GSCFB and LSCFB are two phase flows, the difference is the carrying fluid property. So, the models for those two types of fluidized beds should be similar in principle. The following part is the literature reviews for the applications of CFD models on LSCFBs.

Roy et al [69] simulated the flow field in a LSCFB using the Eulerian two-phase model. The KTGF, Wen-Yu drag model [45], standard k-ε turbulence model, no-slip condition for the liquid and Johnson and Jackson boundary condition for the particles were chosen. The numerical results show satisfied agreements with the experimental data on the flow patterns. It was also found that the simulation result is not sensitive to the restitution coefficient in LSCFBs.

Abbas [14] employed a CFD model based on Eulerian-Eulerian multi-phase flow with KTGF to simulate a LSCFB reactor. Three different turbulence models, the mixture, dispersed and per-phase k-ε models, were investigated. It was reported both the dispersed and per-phase k-ε turbulence models showed qualitative agreements with the experimental data. However, the dispersed turbulence model was less computational expensive.

Cornelissen [70] studied the conventional fluidized bed and investigated the influence of the inlet distributor, restitution coefficients and two different drag models. It was reported that the uniform discrete orifices gave better hydrodynamic behaviors than the non-uniform distributor, the Gidaspow drag model [47] predicted a higher voidage than the Wen-Yu drag model [45], and there was no significant difference by varying restitution coefficient.

Cheng [52] did a parametric study on the particle-particle restitution and particle-wall restitution coefficient. The results showed that the particle-particle restitution coefficient did not have influence on the hydrodynamics due to the lubrication effect from the liquid film, and the higher particle-wall coefficient as 0.99 gave a better agreement with the experimental data.

1.3   Objectives and thesis structure

1.3.1   Objectives and new contributions

In view of the literature reviews presented in the previous section, several CFD models have been developed to simulate the hydrodynamics of liquid-solid circulating fluidized beds. Some parameters including drag models, turbulence models, particle-particle restitution coefficient, and boundary conditions are discussed. However, only a few studies have been carried out to investigate the applicability of the existing drag models for the LSCFBs and the influence of the near wall treatment on the turbulence modeling has not been considered. Therefore, the first objective of the present work is to conduct a comprehensive comparison of various widely used drag models for LSCFBs. Then, on the basis of the drag model study, the effects of different near wall treatments are incorporated and investigated. Besides, the Johnson and Jackson boundary condition [54] is investigated by varying the specularity coefficient and restitution coefficient. In addition, since irregular particles are often used in industrial applications, the drag models based on spherical particles might not suitable. Hence, to improve the accuracy of numerical predictions, the second objective is to develop a drag model that is suitable for irregular particle systems. Furthermore, due to the lack of the validations of the numerical results for LSCFBs under different operating conditions, the third objective is to validate the applicability of the CFD model and investigate the hydrodynamics of LSCFBs under different operating conditions.

The main contributions of the present work are (1) the systematical studies are carried out for the performance of the widely used drag models for the LSCFB systems, (2) the solids holdup distribution and other hydrodynamic behaviors have been successfully improved by incorporating suitable drag model, near wall treatments and boundary conditions, (3) a new drag model for irregular particles, which is a modified Syamlal O'Brien drag model, is proposed and it can improve the agreements between the numerical predictions and experimental data for the system with irregular particles, (4) the proposed CFD model is applied for the simulations of LSCFBs under different operating conditions. The predictions are compared with the experimental data and the agreements are good.

1.3.2 Thesis structure

The thesis is in the "Integrated-Article Format".

Chapter 1 - A comprehensive review on the hydrodynamics studies on the liquid-solid circulating fluidized bed system, the theory of CFD model for the multi-phase flows and some existing studies on CFD models for LSCFB simulations are presented.

Chapter 2 - The applicability of existing drag models for LSCFBs, the performance of the near wall treatment for the liquid phase due to the inapplicability of turbulence model in the close-to-wall region, and the Johnson and Jackson boundary condition for the solid phase are investigated. By analyzing and comparing the numerical and experimental data under different operating conditions, a comprehensive and improved numerical model for LSCFBs is proposed. Furthermore, considering that irregular particles are used in industrial applications, the Syamlal-O'Brien drag model is modified to include the sphericity effect and the numerical results using the modified drag model are compared with the experimental data.

Chapter 3 - The applicability of the proposed CFD model is validated. The hydrodynamics of the LSCFB under different operating conditions are investigated, including the effects of the superficial liquid velocity, superficial solid velocity and particle density.

Chapter 4 - The conclusions and recommendations for future works are provided.

References

[1] Couderc J.-P., 1985, Incipient fluidization and particulate systems,' Chapter 1 Fluidization, 2nd edn., eds. J. F. Davidson, R. Clift and D. Harrison, Academic Press, London, pp. 1-46

[2] Richardson JF, Zaki WN. Sedimentation and fluidization: Part I. Process Safety and Environmental Protection: Transactions of the Institution of Chemical Engineers, Part B. 1997;75: S82S100.

[3] Grace, J.R., "High Velocity Fluidized Bed Reactors", Chem. Eng. Sci. 45, 1953-1966 (1990).

[4] Yang, Y.-L., Y. Jin, Z.-Q. Yu., J.-X. Zhu and H.-T. Bi, "Local Slip Behaviour in the Circulating Fluidized Bed", AIChE Symp. Ser. 89,81-90 (1993).

[5] Liang, W. g., S. L. Zhang, Z. Q. Yu, Y. Jin and Q. W. Wu, "Liquid-Solids Circulating Fluidized Bed (I). Studies on the Phase Holdups and Solid Circulating Rate", J. Chem. Ind. & Eng. China (Chinese edition) 44, 666-671 (1993).

[6] Liang, W. G., Q. W. Wu, Z. Q. Yu, y. Jin and Z. W. Wang, "Hydrodynamics of Gas-Liquid-Solid Three-Phase Circulating Fluidized Bed", in "Fluidization '94'", Science and Technology, Chemical Industry Press, Beijing, China (1994), pp. 329-337.

[7] Liang W.-& Yu Z Q.J, in Y., Wang Z.-W., Wang Y., He M. and Min E., 1995, Synthesis of linear alkylbenzene in a liquid-solids circulating fluidized bed reactor, J. Chem. Technol. Biotechnol., 62,98-102

[8] Liang W.-G., Zhu J.-X., Jin Y., Yu 2.-Q., Wang LW. and Zhou J., 1996, Radial nonuniformity of flow structure in a liquid-solid circulating fluidized bed, Chem. Eng. Sci., 5 1,200 1-20 10.

[9] Liang, W. G., Zhang, S. L., Zhu, J. X., Yu, Z. Q., Jin, Y., & Wang, Z. W. (1997). Flow characteristics of the liquid-solid circulating fluidized bed. Powder Tech., 90, 95–102.

[10] Zheng Y. Flow structure in a liquid-solids circulating fluidized bed [dissertation]. London, Ont: Faculty of Graduate Studies, University of Western Ontario; 1999.

[11] Zheng, Y. and J. X. Zhu, "Microstructural Aspects of the Flow Behavior in a Liquid-Solids Circulating Fluidized Bed", Can. J. Chem. Eng. 78, 75-81 (2000).

[12] Zheng, Y., Zhu, J. X., Marwaha, N., & Bassi, A. S. (2002). Radial solid flow structure in a liquid-solid circulating fluidized bed. Chem Eng J., 88, 141–150.

[13] Sang L. Particle fluidization in upward and inverse liquid-solid circulating fluidized bed [dissertation]. London, Ont: School of Graduate and Postdoctoral Studies, University of Western Ontario; 2013.

[14] Dadashi A, Zhu J, Zhang C. A computational fluid dynamics study on the flow field in a liquid-solid circulating fluidized bed riser. POWDER TECHNOLOGY. 2014;260:528.

[15] Kuramoto K., Tanaka K., Tsutsumi A., Yoshida K. and Chiba T., 1998, Macroscopic flow structure of solid particle in circulating liquid-solid fluidized bed riser, J. Chem. Eng. Japan, 3 1,258-265.

[16] Razzak, S.A. 2009, Hydrodynamic studies in liquid-solid and gas-liquid-solid circulating fluidized beds, The University of Western Ontario (Canada).

[17] Wilhelm, R. M. and M. Kwauk, "Fluidization of Solids Particles", Chem. Eng. Prog. 44, 201-218 (1948).

[18] Mertes, T. S. and H. B. Rhodes, "Liquid-Particle Behaviour (Part 1)", Chem. Eng. Prog. 51, 429-432 (1955).

[19] Lapidus, L. and J. C. Elgin, "Mechanics of Vertical-Moving Fluidized Systems", AlChE J. 3, 63-68 (1957).

[20] Roy S.,Chen J.W.,Kunar S.B., Al-Dahhan M.H. and Dudukovic M.P., 1997, Tomographie and particle tracking studies in a liquid-solid riser, Ind. Eng. Chem. Res., 36,46664669-

[21] Wang, Wei, et al. "A review of multiscale CFD for gas–solid CFB modeling." International Journal of Multiphase Flow 36.2 (2010): 109-118.

[22] Hartge, Ernst-Ulrich, et al. "CFD-simulation of a circulating fluidized bed riser." Particuology 7.4 (2009): 283-296.

[23] Sinclair, J. L., and R. Jackson. "Gas-particle flow in a vertical pipe with particle-particle interactions." AIChE Journal 35.9 (1989): 1473-1486.

[24] Ding, Jianmin, and Dimitri Gidaspow. "A bubbling fluidization model using kinetic theory of granular flow." AIChE journal 36.4 (1990): 523-538.

[25] Ishii, M. (1975) Thermo-fluid Dynamic Theory of Two-phase Flow. Eyrolles, Paris.

[26] Delhaye, J. M. and Achard, J. L. (1977) On the use of averaging operators in two phase flow modeling. Thermal and Hydraulic Aspects of Nuclear Reactor Safety, 1: Light Water Reactors. ASME Winter Meeting.

[27] Boure, J. A. and Delhaye, J. M. (1982) In Handbook of Multiphase Systems, ed. G. Hetsroni, Section 1.2, pp. 1-36-1-95. McGraw-Hill, New York.

[28] Soo, S. L. (1990) Multiphase Fluid Dynamics. Science Press, Gower Technical, New York.

[29] Drew, D. A. and Lahey, R. T. (1993) In Particulate Two-phase Flow, Ch. 16, pp. 509-566, Butterworth-Heinemann, Boston.

[30] He, J. and Simonin, O. Mode1isation num6rique des 6coulements gaz-solides en conduit verticale. Rapport HE-44/94/021A, Laboratoire National d'Hydraulique, EDF, Chatou, France.

[31] H. Enwald et al. Eulerian two phase flow theory applied to fluidization. International Journal of Multiphase Flow 22(1), pp. 2166. 1996. DOI: 10.1016/S03019322(96)90004X.

[32] Van Driest, E. R. (1956), "On Turbulent Flow Near a Wall," Journal of the Aeronautical Sciences, Vol. 23, p. 1007.

[33] Cebeci, T. and Smith, A. M. O. (1974), Analysis of Turbulent Boundary Layers, Ser. In Appl. Math. & Mech., Vol. XV, Academic Press.

[34] Baldwin, B. S. and Lomax, H. (1978), "Thin-Layer Approximation and Algebraic Model for Separated Turbulent Flows," AIAA Paper 78-257, Huntsville, AL.

[35] Boussinesq, J. (1877), "Theorie de l'Ecoulement Tourbillant," Mem. Presentes par Divers Savants Acad. Sci. Inst. Fr., Vol. 23, pp. 46-50.

[36] P. Spalart and S. Allmaras. "A one-equation turbulence model for aerodynamic flows". Technical Report AIAA-92-0439. American Institute of Aeronautics and Astronautics. 1992.

[37] Ansys Fluent. Fluent 16.0 User's Guide.

[38] Chapman, S., & Cowling, T. G. (1970). The Mathematical Theory of Non-Uniform Gases. 3rd ed. Cambridge Univ. Press.

[39] Lun, C.K.K., Savage, S.B., Jeffrey, D.J. and Chepurniy, N., 1984, Kinetic theories for granular flow: inelastic particles in Couette flow and slightly inelastic particles in a general flow field, J Fluid Mech, 140: 223.

[40] Syamlal, M., W. Rogers and T. J. O'Brien, "MFIX Documentation Theory Guide," U.S. Department of Energy Office of Fossil Energy Morgantown Energy Technology Center, Morgantown, WV (1993).

[41] Lewis W K, Gilliland E R and Lang P M (1962). Entrainment from fluidized bed, chem. Eng. Prog. Symp. Ser., 58(38) 65-78.

[42] van Sint Annaland M, Bokkers GA, Goldschmidt MJV, Olaofe OO, van der Hoef MA, Kuipers JAM. Development of a multi-fluid model for poly-disperse dense gas–solid fluidized beds, part II: segregation in binary particle mixtures. Chem. Eng. Sci 2009; 64:4237–46.

[43] Gibilaro LG, Di Felice R, Waldram SP, Foscolo PU. Generalized friction factor and drag coefficient correlations for fluid particle interactions. Chemical Engineering Science. 1985;40(10):181723.

[44] Garside, J. and M. R. Al-Dibouni, "Velocity‒Voidage Relationship for Fluidization and Sedimentation," Ind. Eng. Chem. Proc. Des. Dev. 16(2), 206‒214 (1977).

[45] C.-Y. Wen and Y. H. Yu. "Mechanics of Fluidization". Chem. Eng. Prog. Symp. Series. 62.100-111.1966.

[46] M. Syamlal and T.J. O'Brien. The derivation of a drag coefficient formula from velocity-voidage correlations. Technical Note, U.S. Department of energy, Office of Fossil Energy, NETL, Morgantown, WV, April 1987.

[47] Gidaspow, D., 1994, Multiphase Flow and Fluidization: Continuum and Kinetic Theory Descriptions, Academy, Boston, MA.

[48] L. Huilin and D. Gidaspow. "Hydrodynamics of binary fluidization in a riser: CFD simulation using two granular temperatures". Chemical Engineering Science. 58. 3777-3792. 2003.

[49] Syamlal, M., and O'Brien, T., 2003, "Fluid Dynamic Simulation of O3 Decomposition in a Bubbling Fluidized Bed," AIChE J., 49_11_, pp. 2793–2801.

[50] B. E. Launder and D. B. Spalding. "The Numerical Computation of Turbulent Flows". Computer Methods in Applied Mechanics and Engineering. 3. 269-289. 1974.

[51] Gidaspow, D., Lu, H., 1998. A comparison of gas–solid and liquid–solid fluidization using kinetic theory and statistical mechanics. In: Fan, L.-S., Knowlton, T.M. (Eds.), Fluidization IX. Engineering Foundation, New York, pp. 661–668.

[52] Y. Cheng and J. (. Zhu, "CFD Modelling and Simulation of Hydrodynamics in Liquid–Solid Circulating Fluidized Beds," The Canadian Journal of Chemical Engineering, vol. 83, pp. 177-185, 2005.

[53] M. Ehsani et al, "Effects of Restitution and Specularity Coefficients on Solid Liquid Fluidized Bed Hydrodynamics," Chemical Engineering & Technology, vol. 38, pp. 1827-1836, 2015.

[54] P. C. Johnson and R. Jackson. "Frictional-Collisional Constitutive Relations for Granular Materials, with Application to Plane Shearing". J. Fluid Mech. 176. 67-93.1987.

[55] Wadell H (1933). Sphericity and Roundness of Rock Particles, J. Geol. 41 310-331.

[56] Heywood, H. J. Imp. Oollege Chem. Eng. Soc., 1948,4,17.

[57] Austin, L. G., Gardner, R. P. and Walker, P. L., Jr. The shape factors of coal ground in standard hardgrove mill. Fuel, Journal of Fuel Science, 42 (1963), 319-323.

[58] Briggs, L. T., McCulloch, D. S. and Moser, F- The hydraulic shape of sand particles. Journal of Sedimentary Petrology, 32 (1962), 645-657.

[59] B. Huner, R.G. Hussey, Phys. Fluids 20 _1977. 1211.

[60] T.J. Ui, R.G. Hussey, R.P. Roger, Phys. Fluids 27 _1984. 787.

[61] R. Shail, D.J. Norton, Proc. Camb. Phil. Soc. 65 _1969. 793.

[62] Haider A and Levenspiel O. Drag coefficient and terminal velocity of spherical and nonspherical particles. Powder Technol 1989; 58: 63–70.

[63] Ganser G. A rational approach to drag prediction of spherical and nonspherical particles. Powder Technol 1993; 77: 143–152.

[64] P.K. Swamee, C.P. Ojha, J. Hyd. Eng. 117 _1991. 660.

[65] Chien S. Settling velocity of irregularly shaped particles. Soc Petrol Eng Drilling Completion 1994; 9: 281–289.

[66] Tran-Cong S, Gay M and Michaelides E. Drag coefficients of irregularly shaped particles. Powder Technol 2004; 139: 21–32.

[67] Cleasby, J. L. and Fan, K. S. Predicting fluidization and expansion of filter media. Journal of the Sanitary Engineering Division, American Society of Civil Engineers, 107 (1981), 455-471.

[68] Dharmarajah, Anthonisamy Herman, "Effect of particle shape on prediction of velocity-voidage relationship in fluidized solid-liquid systems " (1982). Retrospective Theses and Dissertations. 7535.

[69] Roy, S.,& Dudukovic, M. P. (2001). Flow Mapping and Modeling of Liquid-Solid Risers. Ind. Eng. Chem. Res., 40, 5440-5454.

[70] J. T. Cornelissen et al, "CFD modelling of a liquid–solid fluidized bed," Chemical Engineering Science, vol. 62, pp. 6334-6348, 2007.

Chapter 2

2   Evaluations of CFD Models for the Liquid-Solid Circulating Fluidized Beds (LSCFBs)

2.1   Introduction

Fluidization is defined as an operation in which a bed of solid particles is suspended in gas and/or liquid media and converted from the solid-like state to the fluid-like state [1]. With the unique gas or liquid-solid contacting features, numerous advantages such as higher contact efficiency and excellent mass and heat transfer are introduced in fluidized beds. Characterized by the different fluid media, fluidization can be cataloged as gas-solid fluidization, liquid-solid fluidization and gas-liquid-solid fluidization. With decades of development, the liquid-solid fluidization has obtained extensive attractions in diverse fields of industrial processes, such as biochemical technology, wastewater treatment, petroleum and metallurgical industries [2].

The liquid-solid fluidization can be divided into four regimes. With the increase in the liquid velocity, the fluidization will go through the fixed bed regime, the conventional fluidization regime, the circulating fluidization regime and the dilute transport regime. When a liquid is introduced from the bottom of a bed, it will pass through the bed via the spaces between static particles. If the liquid velocity is lower than the minimum fluidization velocity, it is within the fixed bed regime. When the liquid velocity is higher than the minimum fluidization velocity, particles start to suspend in the fluid and transform to the fluid-like state, which is the beginning of the conventional fluidization regime. However, the particles are not entrained out of the bed in this regime. With further increase in the liquid velocity, the fluidization becomes more intense and reaches the circulating fluidization regime where most particles can be entrained out of the bed and needed to recirculate back to the bottom of the bed. Further increasing the liquid flow rate, the dilute transport regime is formed.

The hydrodynamics of each regime are different. In the past, the circulating fluidization regime has been relatively less studied compare to the conventional fluidization regime.

Therefore, to have a better understanding of the liquid-solid circulating fluidized bed (LSCFB), a detailed numerical study on the hydrodynamics of the LSCFBs is carried out in the present work.

Start from 1950s, modeling of fluidized bed has become a new tool to investigate and scale up the complex fluidized bed flow structures. A series of mathematical models, such as the two-phase model for the conventional fluidized bed and core-annulus model for the circulating fluidized bed were proposed. However, those models cannot accurately describe the complicated flow fields for fluidized beds. Therefore, the computational fluid dynamics (CFD) modeling has become an effective tool to investigate the hydrodynamics inside a CFB riser due to the fast development of the computer technology and multiphase flow models [3-6].

Generally, there are two major theories for describing multiphase flows: (1) Eulerian-Lagrangian (E-L) approach where the particulate trajectory model is used for the solid-phase and the particle-particle interactions are neglected and (2) Eulerian-Eulerian (E-E) approach where the two-fluid model is used, i.e. both phases are treated as fluid phase. In the present work, the Eulerian-Eulerian approach is employed since the solid volume fraction in LSCFB is high and the interactions between particles need to be considered. In the Eulerian-Eulerian approach, the fluid and solid phases are considered as the interpenetrating continuum, and the mass and momentum governing equations, which are closed by the constitutive equations, are solved for both phases [7].

Studies have been conducted on the dynamics of particles flowing in a fluid, including the mechanisms of the drag force due to the velocity difference between secondary and primary phases, the buoyant force due to the pressure gradient of the fluid, the lift force due to the velocity gradient of the fluid, and the virtual mass force due to the acceleration of secondary phase to primary phase. Among those forces, the drag force is the most important one. Several drag correlations have been proposed in the past several decades. From the simplest single particle drag correlations [8] to the complex semi-empirical drag correlations, those drag models can be catalogued into three groups: the Ergun equation [9] and Gibilaro drag model [10] which are based on the pressure drop of the fixed beds; the Richardson-Zaki

equation [11], Wen-Yu [12], and Syamlal et al [13] models which are based on the velocity-voidage correlations; and the latest EMMS which is based on the energy minimization multi-scale method. Besides, the Gidaspow [14] and Huilin-Gidaspow [15] models were obtained based on the work of Ergun [9] and Wen-Yu [12], and the adjusted Syamlal-O'Brien drag model [16] was proposed to extend the applicability of the Syamal-O'Brien model [13] by adjusting the velocity-voidage function parameters to match the experimental minimum fluidization velocity.

For the wall bounded flows, due to the considerable influence of the walls on the turbulent flows, an accurate representation of the flow in the near wall region should be adopted to ensure accurate numerical solutions. Generally, there are two approaches to model the near-wall region. The first one is by adopting semi-empirical functions to represent the viscosity affected region instead of solving turbulence equations, such as the standard wall functions and scalable wall functions. The second one is by modifying the turbulence model to resolve the flow in the near wall region, such as the enhanced wall treatment [17] and Menter-Lechner near wall treatment [17]. However, the influence of the near wall treatments on the numerical solutions has not been fully discussed. Therefore, it will be investigated in this study and a suitable near wall treatment will be selected and incorporated with the drag model.

For the boundary conditions, the no-slip boundary condition at the wall is used for the liquid phase, which is not suitable for the solid phase. Therefore, the Johnson and Jackson [18] boundary condition which contains the specularity coefficient and restitution coefficient is used to describe the interaction and energy loss between the granular flow and the wall. To ensure the boundary conditions are correctly used, the effects of the specularity coefficient and restitution coefficient are investigated.

In addition, irregular particles can be used in fluidized beds in some industrial applications, which might significantly affect the hydrodynamic behaviors of the fluidization process. Therefore, studies have been conducted to investigate the influence of particle shapes on the flows in fluidized beds. Firstly, different shape factors were introduced, such as the sphericity and circularity by Wadell [19], volumetric shape factor by Heywood [20], and

other indirect methods including the "dynamic shape factor" defined by McCulloch and Moser [21]. Secondly, the shape factors were incorporated into drag models. Start form 1970s, simple drag correlations for particles with fixed shape and flow direction have been derived, such as those by Huner and Hussey [22], Ui et al. [23], and Shail and Norton [24]. Then, attempts were made to extend their applicability by developing a universal drag correlation for flows under different operating conditions, such as the drag models developed by Haider and Levenspiel [25], Ganser [26], Swamee and Ojha [27], Chien [28], and Tran-Cong et al. [29]. However, they are not suitable for the fluidized bed since it is a multi-particle system. Therefore, Richardson and Zaki [11] incorporated the volumetric shape factor into their velocity-voidage function under the limited condition of $Re > 500$ for relatively large irregular particles ($d > 100 \mu m$). Cleasby and Fan [30] incorporated the "n" value from the RZ equation [11] with a function of shape factor obtained from the experimental data for irregular particles of sand, anthracite and flints. Then Dharmarajah [31] proposed the relationship between the bed voidage, sphericity, and superficial liquid velocity by introducing complicated terms such as modified Reynolds number and A_1. However, this relationship is not suitable for bed voidage beyond 0.9.

Despite the numerous studies for the multi-phase flows in the literature, none of those studies has comprehensively compared the applicability of different drag models for the LSCFB system. And none of the studies has investigated the influence of near wall treatments and boundary conditions incorporating with drag models. In addition, the drag model for particles with irregular shapes has not been investigated for LSCFB systems. Therefore, the present work employs the Eulerian-Eulerian CFD model based on KTGP to systematically study the following four aspects: the influence of drag models, near wall treatments for the turbulence model, specularity coefficient, restitution coefficient and the drag model for particles with irregular shapes.

2.2 Experimental setup of the LSCFB system

The experimental data on the liquid-solid two-phase flows in LSCFB by Razzak [1] and Sang [32] will be used in the present work to verify the numerical models.

The schematic diagram of the experimental setup is presented in Fig 2.1. It consists of two main sections: riser and downer. The riser is made of Plexiglas with 5.4m in height and 0.0762m in diameter, and the downer is made of Plexiglas as well with 5.05m in height and 0.2m in diameter. The liquid-solid separator is located at the top of the riser for separating the entrained solids from the liquid and the solids circulation rate measurement device is located near the top of the downer. At the bottom of the riser, there are two liquid distributors, the seven primary liquid distributors occupy 19.5% of the cross-sectional area, and the auxiliary liquid distributor which is a porous plate with 4.8% of opening area and controls the recirculating particles flow rate.

The particles are injected from the solids feed pipe, by adjusting the auxiliary liquid flow rate, the quantity of recirculating particles from the storage vessel can be controlled. When auxiliary liquid velocity is zero, there will be no particles enter the riser. Introducing the auxiliary liquid flow to start feeding particles and with the lifting effect from both auxiliary liquid and primary liquid, all particles can be fluidized and entrained out of the riser. Then they are separated from the liquid in the liquid-solid separator, and ejected into the downer, finally reach to the solids feed pipe again and complete the circulation.
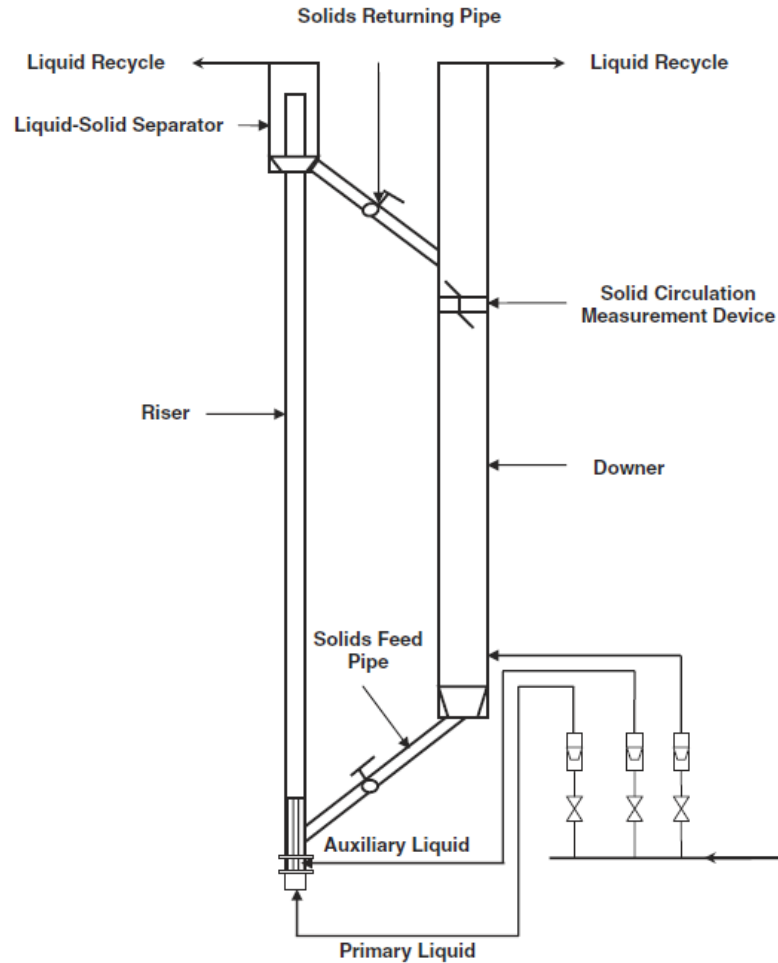
Figure 2.1: Experimental setup of the LSCFB riser

In this study, two different operating conditions with spherical glass beads operated by Razzak [1] are selected to study the effects of different drag models, near wall treatments, specularity coefficient and restitution coefficient, and one operating condition with irregular plastic beads from Sang [32] is chosen to investigate the drag model for irregular particles. All the simulations are conducted under the ambient temperature and tap water. The detailed operation conditions and physical properties of the particles and liquid are listed in Table 2.1.

Table 2.1: Operation conditions and physical properties of the particles and liquid

Parameters	Liquid phase density (kg/m³)	Liquid phase viscosity (kg/m⁻ˢ)	Particle density (kg/m³)	Particle diameter (μm)	Particle sphericity	Superficial liquid velocity (cm/s)	Superficial solid velocity (cm/s)
Operating condition #1	998.2	0.001003	2500	500	1	11.2	0.747
Operating condition #2	998.2	0.001003	2500	500	1	35	1.193
Operating condition #3	998.2	0.001003	1520	580	0.7	28	0.4

2.3 Numerical models

The Eulerian-Eulerian based CFD model is used to solve the governing equations for both continuous liquid phase and discrete solid phase. The governing equation for the continuous liquid phase is closed by the k-ε turbulence model and the governing equation for the discrete solid phase is closed by the models based on kinetic theory of granular phase (KTGP). Those constitutive equations are derived based on different theoretical assumptions and empirical correlations.

2.3.1   Governing equations

The continuity and momentum equations are given as:

$$\frac{\partial}{\partial t}\left(\alpha_q \rho_q\right)+\nabla\bullet\left(\alpha_q \rho_q \overrightarrow{v_q}\right)=0, \quad \sum_q \alpha_q =1 \tag{1}$$

$$\frac{\partial}{\partial t}\left(\alpha_l \rho_l \overrightarrow{v_l}\right)+\nabla\bullet\left(\alpha_l \rho_l \overrightarrow{v_l}^2\right)=-\alpha_l \nabla p +\nabla\bullet\overline{\overline{\tau_l}}+\alpha_l \rho_l \overrightarrow{g}+K_{sl}\left(\overrightarrow{v_s}-\overrightarrow{v_l}\right)$$

$$\overline{\overline{\tau_l}}=\alpha_l \mu_l \left(\nabla\bullet\overrightarrow{v_l}+\nabla\bullet\overrightarrow{v_l}^T\right)$$

$$\frac{\partial}{\partial t}\left(\alpha_s \rho_s \overrightarrow{v_s}\right)+\nabla\bullet\left(\alpha_s \rho_s \overrightarrow{v_s}^2\right)=-\alpha_s \nabla p +\nabla p_s +\nabla\bullet\overline{\overline{\tau_s}}+\alpha_s \rho_s \overrightarrow{g}+K_{ls}\left(\overrightarrow{v_l}-\overrightarrow{v_s}\right)$$

$$\overline{\overline{\tau_s}}=\alpha_s \mu_s \left(\nabla\bullet\overrightarrow{v_s}+\nabla\bullet\overrightarrow{v_s}^T\right)+\alpha_s \left(\lambda_s -\frac{2}{3}\mu_s\right)\nabla\bullet\overrightarrow{v_s}\overline{\overline{I}} \tag{2}$$

where α_q is the volume fraction of phase q.

For the continuous liquid phase, a k-ε turbulence model is employed to close the governing equations. Since the dispersed k-ε model is computationally less expensive and predicts the hydrodynamics equally well as the per-phase turbulence model [33], it is used in the simulations and is given as:

$$\frac{\partial}{\partial t}\left(\alpha_l \rho_l k_l\right) + \nabla \bullet \left(\alpha_l \rho_l \vec{v}_l k_l\right) = \nabla \bullet \left(\alpha_l \frac{\mu_{t,l}}{\sigma_k} \nabla k_l\right) + \alpha_l G_{k,q} - \alpha_l \rho_l \varepsilon_l - K_{sl}\left(2k_l - \sqrt{2k_l}\sqrt{3\Theta_s}\right)$$

$$\frac{\partial}{\partial t}\left(\alpha_l \rho_l \varepsilon_l\right) + \nabla \bullet \left(\alpha_l \rho_l \vec{v}_l \varepsilon_l\right) = \nabla \bullet \left(\alpha_l \frac{\mu_{t,l}}{\sigma_\varepsilon} \nabla \varepsilon_l\right) + \alpha_l \frac{\varepsilon_l}{k_l}\left(C_{1\varepsilon} G_{k,l} - C_{2\varepsilon} \rho_l \varepsilon_l\right) - C_{2\varepsilon} \frac{\varepsilon_l}{k_l} K_{ls}\left(2k_l - \sqrt{2k_l}\sqrt{3\Theta_s}\right) \quad (3)$$

For the solid phase, the KTGP is employed to model the viscosity, stresses and pressure of solid phase which are used in the momentum conservation equation. Based on the KTGP, the viscosity, pressure and stresses for the solid phase can be determined by the granular temperature, which is the mean square of a random particle velocity. The constitutive equations for the solid phase are summarized in Table 2.2.

Table 2.2: Constitutive equations for the solid phase

Solids pressure	$P_s = \alpha_s \rho_s \Theta_s + 2\rho_s(1+e_{ss})\alpha_s^2 g_{O,ss}\Theta_s$	(Lun et al. [34])
Radial distribution function	$g_{O,ss} = \left[1 - \left(\dfrac{\alpha_s}{\alpha_{s,\max}} \right)^{1/3} \right]^{-1}$	(Ding and Gidaspow [6])
Solids shear stress	$\mu_s = \mu_{s,col} + \mu_{s,kin} + \mu_{s,fr}$	
Collisional viscosity	$\mu_{s,col} = \dfrac{4}{5}\alpha_s \rho_s d_s g_{O,ss}(1+e_{ss})\sqrt{\dfrac{\Theta_s}{\pi}}$	(Gidaspow et al. [14])
Kinetic viscosity	$\mu_{s,kin} = \dfrac{\alpha_s \rho_s d_s \sqrt{\Theta_s \pi}}{6(3+e_{ss})}\left[1 + \dfrac{2}{5}(1+e_{ss})(3e_{ss}-1)\alpha_s g_{O,ss} \right]$	(Syamlal et al. [35])
Frictional viscosity	$\mu_{s,fr} = \dfrac{P_s \sin\phi}{2\sqrt{I_{2D}}}$	(Schaeffer [36])
Bulk viscosity	$\lambda_s = \dfrac{4}{3}\alpha_s^2 \rho_s d_s g_{O,ss}(1+e_{ss})\sqrt{\dfrac{\Theta_s}{\pi}}$	(Lun et al. [34])
Granular conductivity	$k_{\Theta s} = \dfrac{15 d_s \rho \alpha_s \sqrt{\Theta_s \pi}}{4(41-33\eta)}\left[1 + \dfrac{12}{5}\eta^2(4\eta-3)\alpha_s g_{O,ss} + \dfrac{16}{15\pi}(41-33\eta)\eta\alpha_s g_{O,ss} \right]$ $\eta = \dfrac{1}{2}(1+e_{ss})$	(Syamlal et al. [35])
Collisional dissipation of energy	$\gamma_{\Theta s} = \dfrac{12(1-e_{ss}^2)g_{O,ss}}{d_s \sqrt{\pi}}\rho_s \alpha_s^2 \Theta_s^{3/2}$	(Lun et al. [34])

2.3.2   Drag models

The drag force is one of the dominate terms in the momentum equation and represents the momentum exchange between phases. Six widely used drag models are investigated in this study.

Syamlal O'Brien drag model [13]

The Syamlal O'Brien drag model gives the correlation between the multi-particle system and single particle system by the velocity-voidage function.

For a particle flows in a fluid, the drag force can be written as

$$F_{drag} = \frac{1}{2} \rho_g C_D \left(u_g - u_s \right)^2 A_p = K_{ls} \left(u_g - u_s \right) \tag{4}$$

where A_p is the cross-sectional area of a particle and K_{ls} represents the fluid-solid exchange coefficient. For a multi-particles flow, assuming there are n particles inside a control volume, which are related to the bed voidage as

$$n = \frac{6 \left(1 - \alpha_g \right)}{\pi d_p^3} \tag{5}$$

Therefore, K_{ls} can be rewritten as

$$K_{ls} = \frac{3 \rho_g \alpha_g \left(1 - \alpha_g \right)}{4 d_p} C_D \left| \vec{u_s} - \vec{u_g} \right| \tag{6}$$

However, this equation doesn't take particle interactions into consideration, while the fluidized bed is a multi-particle system which is far more complicated than the individual particulate flow. Therefore, Syamlal O'Brien employed the velocity-voidage function to bridge the two different systems [13].

For a single particle under terminal settling conditions, the drag force equals to the buoyant weight.

$$C_{Dts} \frac{\pi d_p^2}{4} \frac{\rho_f U_t^2}{2} = \frac{\pi d_p^3}{6} \left(\rho_s - \rho_f \right) g \tag{7}$$

where C_{Dts} is the drag coefficient of a single particle under the terminal settling condition. Eq. (7) can be rewritten as

$$\frac{3}{4} C_{Dts} \operatorname{Re}_{ts}^2 = Ar \tag{8}$$

where Ar is Archimedes number, which is only related to the properties of the fluid and solids. Similarly, the relationship for a multi-particle system can be expressed as

$$\frac{3}{4} C_{Dt} \operatorname{Re}_t^2 = Ar \tag{9}$$

where C_{Dt} is the drag coefficient for a multi-particle system. Based on Eqs. (8) and (9), the following correlation can be obtained,

$$C_{Dt} = \left(\frac{\operatorname{Re}_{ts}}{\operatorname{Re}_t} \right)^2 C_{Dts} \tag{10}$$

Using the velocity-voidage function $Vr = \dfrac{U_t}{U_{ts}} = \dfrac{\operatorname{Re}_t}{\operatorname{Re}_{ts}} = \varepsilon^{n-1}$ defined by Richardson-Zaki [11], Eq. (10) becomes,

$$C_{Dt}(\operatorname{Re}_t, \varepsilon) = \frac{C_{Dts}(\operatorname{Re}_{ts})}{V_r^2} = \frac{C_{Dts}(\operatorname{Re}_t / V_r)}{V_r^2} \tag{11}$$

By dropping the subscript t in Eq. (11), the general expression of C_D can be obtained for a multi-particle system.

$$C_D(\text{Re}, \varepsilon) = \frac{C_{Ds}(\text{Re}/V_r)}{V_r^2} \tag{12}$$

Therefore, the fluid-solid exchange coefficient K_{ls} for Syamlal O'Brien drag model [13] is defined as

$$K_{ls} = \frac{3\alpha_s \alpha_l \rho_l}{4 v_{r,s}^2 d_s} C_D \left(\frac{\text{Re}}{v_{r,s}} \right) \left| \vec{v}_s - \vec{v}_l \right| \tag{13}$$

where the drag coefficient is from Dalla Valle [37]

$$C_D = \left(0.63 + \frac{4.8}{\sqrt{\text{Re}_s}} \right)^2 = \left(0.63 + \frac{4.8}{\sqrt{\text{Re}/v_{r.s}}} \right)^2 \tag{14}$$

And the relative Reynolds number has the form as

$$\text{Re} = \frac{\rho_l d_s \left| \vec{v}_s - \vec{v}_l \right|}{\mu_l} \tag{15}$$

The velocity-voidage correlation $v_{r,s}$ is from Garside and Al-Dibouni [38].

$$\frac{v_{r,s} - A}{B - v_{r,s}} = 0.06 \text{Re}_s \tag{16}$$

where

$$A = \alpha_l^{4.14}$$

$$B = \begin{cases} c_1 \alpha_l^{1.28} & \alpha_l \leq 0.85 \quad c_1 = 0.8 \\ \alpha_l^{d_1} & \alpha_l > 0.85 \quad d_1 = 2.65 \end{cases}$$

By substituting $v_{r,s} = \text{Re}/\text{Re}_s$ in Eq. (16), we have

$$v_{r,s} = 0.5 \left(A - 0.06 \text{Re} + \sqrt{(0.06 \text{Re})^2 + 0.12 \text{Re}(2B - A) + A^2} \right) \tag{17}$$

Gidaspow drag model [14]

To cover all flow situations, Gidaspow [14] combined the Ergun equation [9] and Wen-Yu drag model [12].

When $\alpha_l > 0.8$, the Wen-Yu drag model [12] is adopted:

$$K_{sl} = \frac{3}{4} C_D \frac{\alpha_s \alpha_l \rho_l \left| \vec{v}_s - \vec{v}_l \right|}{d_s} \alpha_l^{-2.65}$$

(18)

where

$$C_D = \frac{24}{\alpha_l \, \mathrm{Re}_s} \left[1 + 0.15 \left(\alpha_l \, \mathrm{Re}_s \right)^{0.687} \right]$$

When $\alpha_l \leq 0.8$, the Ergun equation [9] is adopted:

$$K_{sl} = 150 \frac{\alpha_s \left(1 - \alpha_l \right) \mu_l}{\alpha_l d_s^2} + 1.75 \frac{\rho_l \alpha_s \left| \vec{v}_s - \vec{v}_l \right|}{d_s}$$

(19)

Huilin-Gidaspow drag model [15]

To avoid the discontinuity of the Gidaspow drag model [14] at $\alpha_l = 0.8$, a blending function was used in Huilin-Gidaspow drag model [15], which is defined as

$$K_{sl} = \psi K_{sl-Ergun} + \left(1 - \psi \right) K_{sl-Wen-Yu}$$

(20)

where

$$\psi = \frac{1}{2} + \frac{\arctan \left(262.5 \left(\alpha_s - 0.2 \right) \right)}{\pi}$$

Gibilaro drag model [10]

Based on the Ergun equation [9], Gibilaro [10] extended its applicability to the dilute particle system by relating the energy dissipation in the fluidized bed with the

unrecoverable pressure loss to obtain the particle drag force under the fully expanded limit condition. The Gibilaro drag model is shown below [10].

$$K_{sl} = \left(\frac{18}{\text{Re}} + 0.33 \right) \frac{\rho_f \left| \vec{v}_s - \vec{v}_l \right|}{d_p} \alpha_s \alpha_l^{-1.8} \tag{21}$$

where the Reynolds number is defined as

$$\text{Re} = \frac{\alpha_l \rho_l d_p \left| \vec{v}_s - \vec{v}_l \right|}{\mu_l}$$

Single particle drag correlation [8]

The liquid-solid fluidization is homogeneous. Hence, the single particle drag correlation is also considered and the results are compared with the multi-particle drag models. The single particle drag correlation used here is from Lewis et al. [8].

$$\begin{cases} C_{Ds} = \dfrac{24}{\text{Re}} & \text{Re} < 0.4 \\[2mm] C_{Ds} = \dfrac{10}{\text{Re}^{0.5}} & 0.4 < \text{Re} < 500 \\[2mm] C_{Ds} = 0.43 & 500 < \text{Re} < 200000 \end{cases} \tag{22}$$

2.3.3　Adjustment of the drag model

Adjusted Syamlal-Obrien drag model [16]

With wide use of the Syamlal-O'Brien drag model [13], people encountered the situation where the operating conditions are remarkably differed from the original experimental conditions. To extend its applicability, the Syamlal-O'Brien drag model [13] can be adjusted by matching the predicted minimum fluidization velocity with the experimental data and the constants c_1 and d_1 can be modified correspondingly.

Under the minimum fluidization conditions, the Eq. (16) can be rewritten as

$$\text{Re}_{mf} = \text{Re}_{mfs}\left[\frac{A+0.06B\,\text{Re}_{mfs}}{1+0.06\,\text{Re}_{mfs}}\right] \tag{23}$$

The minimum fluidization condition and terminal settling condition can be considered the same for a single particle. Therefore, the terminal settling Reynolds number Re_{ts} is defined by substituting Eq. (14) in Eq. (8).

$$\text{Re}_{ts} = \left[\frac{\left(4.8^2 + 2.52\sqrt{4Ar/3}\right)^{0.5} - 4.8}{1.26}\right]^2 \tag{24}$$

where the Archimedes number is related to the drag coefficient and the Reynolds number

$$Ar = \frac{\rho_l}{\mu_l^2}d_s^{\ 3}\left(\rho_s - \rho_l\right)g \tag{25}$$

The minimum fluidization Reynolds number for the multi-particle system Re_{mf} can be determined by the experimental measuring data. Furthermore, the drag coefficient and velocity-voidage correlation are the same as those in the Syamlal-O'Brien drag model [13] and the relationship between coefficient c_1 and d_1 is defined as follow to ensure the continuity of B.

$$d_1 = 1.28 + \frac{\log_{10}^{\ c1}}{\log_{10}^{\ 0.85}} \tag{26}$$

For most cases, once the particle properties and the minimum fluidization condition are known, c_1 and d_1 can be determined

Drag model for irregular particles

The drag force between the liquid and solid mainly depends on the local slip velocity, bed voidage, liquid properties, and solid properties, including particle density, size, and shape. However, the six drag models mentioned above are all derived based on spherical particles,

it is essential to take the sphericity into consideration for the irregular particle cases. Therefore, a new drag model, which is a modified Syamlal-O'Brien drag model, is proposed in the work. The numerical results from the new drag model are validated by comparing them with the experimental data from Sang [32] where the experiments were conducted using plastic beads with irregular shapes.

Since the Syamlal-O'Brien drag model [13] is based on the single particle drag model and the velocity-voidage function for spherical particles, the idea of modification is to replace them by the correlations for irregular particles.

There are different shape factors and corresponding empirical drag correlations for single non-spherical particles. Therefore, the single non-spherical particle drag coefficient proposed by Haider and Levenspiel [25] are employed in this research.

$$C_D = \frac{24}{\text{Re}} \left[1 + \left\{ 8.1716 \exp\left(-4.0655\psi\right) \right\} \times \text{Re}^{(0.0964+0.5565\psi)} \right] + \frac{73.69 \, \text{Re} \exp\left(-5.0748\psi\right)}{\text{Re} + 5.378 \exp\left(6.2122\psi\right)} \quad (27)$$

The shape factor $\psi = \dfrac{s}{S}$, where s is the surface area of a sphere having the same volume as the irregular particle, and S is the actual surface area of the irregular particle [19].

The correlation for the velocity-voidage function, which is a function of the shape factor, is from Cleasby and Fan [30].

$$V_r = \frac{U}{U_t} = \varepsilon^{n-1}$$

where $n = n_{sperical} \times \left(\psi\right)^{\gamma}$ and $\gamma = -2.9237 \, \text{Re} t^{-0.363} \left(\psi\right)^{0.884}$. The $n_{spherical}$ is the "n" value form RZ equation [11].

$$\begin{cases} n_{sperical} = 4.65 + 20d/D & \mathrm{Re}t \leq 0.2 \\ n_{sperical} = (4.4 + 18d/D)\,\mathrm{Re}t^{-0.03} & 0.2 < \mathrm{Re}t \leq 1 \\ n_{sperical} = (4.4 + 18d/d)\,\mathrm{Re}t & 1 < \mathrm{Re}t \leq 200 \\ n_{sperical} = 4.4\,\mathrm{Re}t^{-0.1} & 200 < \mathrm{Re}t \leq 500 \\ n_{sperical} = 2.4 & \mathrm{Re}t > 500 \end{cases} \tag{28}$$

Therefore, by applying Eq. (12), the drag coefficient for irregular multi-particle systems can be obtained.

$$C_D = \frac{24}{\mathrm{Re}Vr}\left\{ 1 + \left[8.1716\exp(-4.0655\psi)\right] \times \left(\frac{\mathrm{Re}}{Vr}\right)^{0.0964+0.5565\psi} \right\} + \frac{73.69\,\mathrm{Re}\exp(-5.0748\psi)}{Vr^2\,\mathrm{Re} + 5.378Vr^3\exp(6.2122\psi)}$$

$$(29)$$

2.3.4   Near wall treatment

In this study, three different near wall treatments are implemented and examined. The first one is the scalable wall function [17], which is a Y^+ independent wall function and it is a modified version of the standard wall function. The second one is the enhanced wall treatment [17], which is based on the two-layer models with a blend function. The third one is the Menter-Lechner near wall treatment [17], in which a source term is introduced in the transport equation of the turbulence kinetic energy and the modified momentum equations are used.

Scalable Wall Functions [17]

The scalable wall function can avoid the computational deterioration when y*<11 by adding a selector.

$$y^* = MAX\left(y^*, y^*_{\text{limit}}\right) \tag{30}$$

where $y^*_{\text{limit}} = 11.225$. Hence, if y*>11.225, the standard and scalable wall functions are identical. It should be noted that the y* and Y^+ are approximately equal in the equilibrium turbulent boundary layer. Therefore, the y* is used in ANSYS Fluent.

Enhanced Wall Treatment [17]

By modifying the turbulence model, the enhanced wall treatment ensures to resolve the viscous sublayer with a refined mesh where the first wall-adjunct grid meets Y$^+$=1. The two-layer approach is employed to specify both ε and the turbulent viscosity in the near-wall cells [17].

Menter-Lechner ε **- *Equation*** [17]

To avoid the drawbacks of the enhanced wall treatment, such as mistreat the region with low values of turbulence kinetic energy as the near wall region, the errors with the calculations for pressure gradient (non-equilibrium) flows and the oscillation if a coarse first mesh is used, the Menter-Lechner near wall treatment is introduced. In the Menter-Lechner wall treatment, a source term is added to the $k - \varepsilon$ turbulence model instead of replacing ε and turbulent viscosity from separate equations in the near wall region.

2.4 Numerical methodology

To simulate the two-phase flows in the LSCFB shown in Fig 2.1, the riser is simplified to a 2D-planar as shown in Fig 2.2 and the mesh information can be seen from Table 2.3. Due to the potential instantaneous non-axisymmetric flow structures within LSCFBs, the 2D planar mesh is created and the results are time averaged for 20s after reaching the stable condition. In addition, with the use of enhanced wall treatment, the Y$^+ \leq 1$ should be satisfied for the first wall adjacent grid. Therefore, the finer grid is used in the near wall region with an expand ratio of 1.05 for the cell size from the wall to the center of the bed. Besides, to correctly represent the complex flow structures at the inlet, the mesh in the inlet region has been refined as shown in Fig 2.3 and the expand ratio is set as 1.05 as well.

The mesh independence is examined for the operating condition #3 using three different grids, 60×1500, 100×2500 and 120×2500, in the x and y directions, respectively. The radial profiles of the solids concentration at different bed heights, H=1.01m, 2.02m, 3.03m and 3.82m, are compared. It is found that the difference in the results for all three meshes is less than 0.5%. Therefore, the medium mesh (100×2500) is used to reduce the

calculation time while ensure the accuracy. The mesh information for different operating conditions is given in Table 2.3.

For the boundary conditions, at the inlet, which is located at the bottom of the riser, both the liquid and particles are of uniform velocities. At the outlet, outflow condition is used due to the fully developed flow condition at the outlet. On the wall, the no-slip condition is used for the liquid phase, and partial slip Johnson and Jackson [18] boundary condition is used for the solid phase. The dispersed k-ε turbulence model is used for the liquid phase while the particle-particle collision restitution coefficient is set as 0.95 for the solid phase. The phase coupled SIMPLE scheme is used for the pressure-velocity coupling, the power law is chosen to discretize the convection terms for the k-ε turbulence model and granular temperature while the QUICK is chosen for mass and momentum governing equations. Besides, the time step size is set as 1×10^{-04} s and the convergence criteria is set as 5×10^{-05}.

The parameters in the proposed drag model for irregular particles can be determined based on the sphericity of the particles used in the experimental work by Sang [32], which is 0.7. The proposed drag model is compiled into Fluent solver by User Defined Function (UDF) and the UDF file is given in Appendix B.
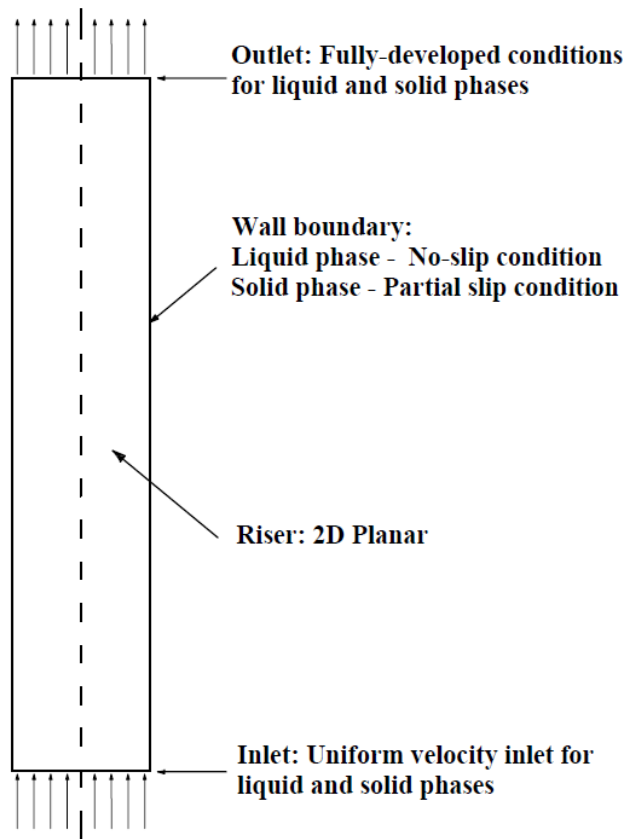
Figure 2.2: Schematics of the LSCFB riser
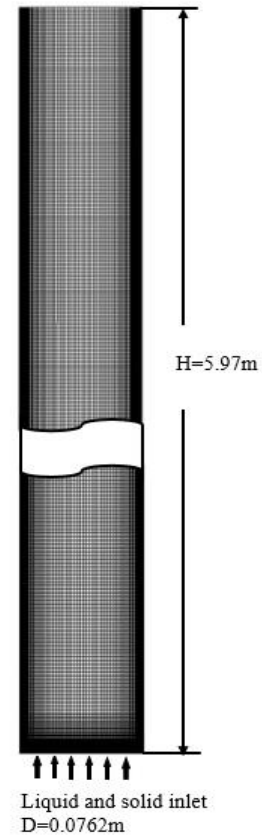
Figure 2.3: Diagram of the mesh created for simulations

Table 2.3: Mesh information for different operating conditions

Parameters	Domain size (m)	Number of control volumes	Wall space for first grid (m)	Increasing ratio along radius	Increasing ratio along axis	Maximum aspect ratio
Operating condition #1	0.0762×5.97	100×2500	0.00015	1.05	1.05	16.73
Operating condition #2	0.0381×5.97	100×2500	0.000052	1.05	1.05	41.12
Operating condition #3	0.0762×5.2	100×2500	0.000064	1.05	1.05	29.48

2.5   Results and discussion

The numerical models described above are employed to predict the flow field and hydrodynamics of a LSCFB riser. The effects of the drag models for spherical and irregular particles, the near wall treatments for the turbulence flow and the coefficients for the Johnson and Jackson [18] boundary conditions are examined by comparing the numerical results with the experimental data. Besides, the effects of some critical parameters affecting the predictions are analyzed.

2.5.1   Studies of the drag models for spherical particles

To investigate the influence of drag models on the numerical results for spherical particle systems, the simulations are conducted using six different drag correlations with the enhanced wall treatment under two operating conditions, Operating Conditions #1 and #2 as shown in Table 2.1. For the adjusted Syamlal-O'Brien drag model [16], the parameters for the velocity-voidage correlation c_1 and d_1, which only depend on the properties of particles and fluid, are adjusted to 0.304 and 8.605, respectively, for both operating conditions to match with the experimental data.

The comparisons for the radial solids holdup profiles using different drag modes with the enhanced wall treatment are shown in Figs 2.4 and 2.5 under two operating conditions, respectively.

Figure 2.4: Comparisons of the radial distributions of the solids holdup using different drag models under U_l= 11.2 cm/s and U_s= 0.747 cm/s

(a) H= 1.01m and (b) H= 3.82m
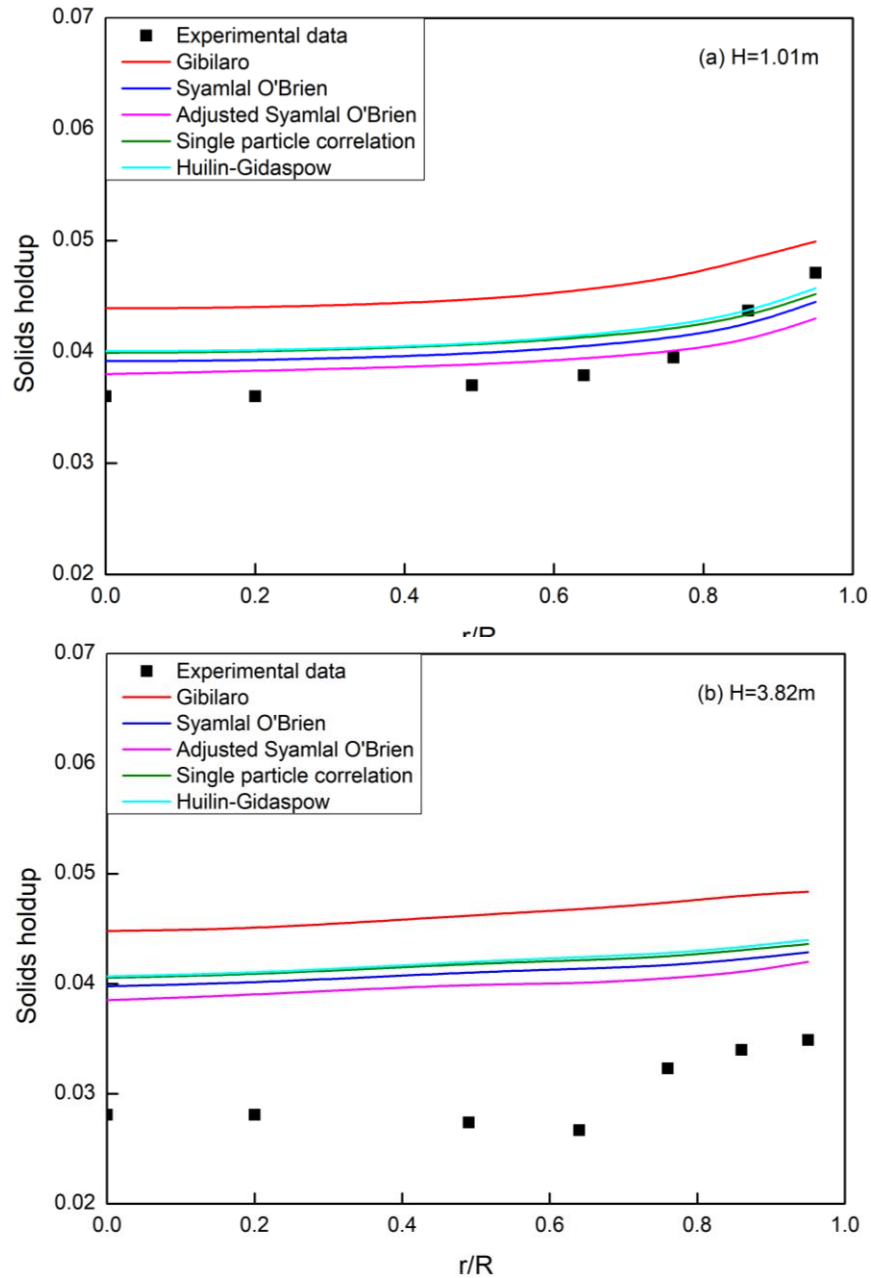
Figure 2.5: Comparisons of the radial distributions of the solids holdup using different drag models under U_l= 35 cm/s and U_s= 1.193 cm/s

(a) H= 1.01m and (b) H= 3.82m

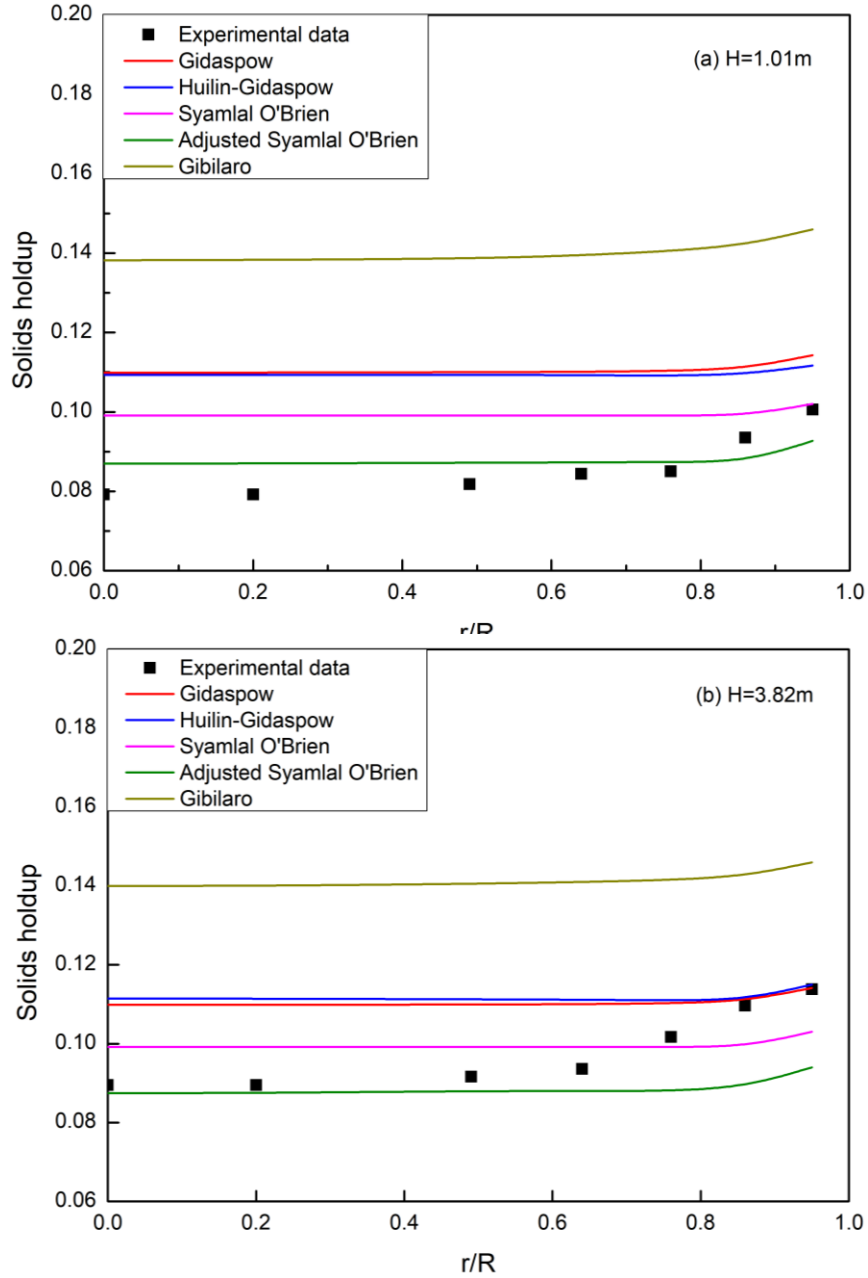All the predicted radial solids holdup distributions have the same trend. It is due to the frictions and no slip conditions between the liquid and the wall in wall bounded flows. The

liquid velocity decreases towards the wall and finally approaches to 0 near the wall, which leads to the same trend for the solid velocity. Therefore, the solids concentration is higher at the near wall region and lower at the central region. However, all the simulations tend to overestimate the solids holdup compared to the experimental data and the increase in the solids holdup towards the wall is not as obvious as that shown in the experiment. The difference between the numerical results and experimental data are listed in Tables 2.4 and 2.5 under different operating conditions.

Table 2.4: Difference between the numerical results and experimental data using different drag models H=3.82m under U_l= 11.2 cm/s and U_s= 0.747 cm/s

r/R	Experimental solids holdup	Gibilaro	Syamlal O'Brien	Adjusted Syamlal O'Brien	Gidaspow	Huilin-Gidaspow
0	0.0895	56.42%	10.85%	2.23%	22.73%	24.49%
0.2	0.0895	56.42%	10.85%	2.23%	22.75%	24.50%
0.49	0.0916	53.38%	8.31%	3.93%	20.02%	21.48%
0.64	0.0936	50.64%	5.99%	5.98%	17.55%	18.74%
0.76	0.1017	39.13%	2.45%	11.50%	8.39%	9.12%
0.86	0.1096	30.02%	9.48%	17.88%	1.09%	1.40%
0.95	0.1138	28.30%	9.49%	17.40%	0.31%	1.05%

Table 2.5: Difference between the numerical results and experimental data using different drag models at H=1.01m under U_l= 35 cm/s and U_s= 1.193 cm/s

r/R	Experimental solids holdup	Gibilaro	Syamlal O'Brien	Adjusted Syamlal O'Brien	Single particle correlation	Huilin-Gidaspow
0	0.036	22.03%	8.83%	5.56%	10.92%	11.33%
0.2	0.036	22.08%	8.92%	6.39%	11.03%	11.39%
0.49	0.037	20.46%	7.51%	4.86%	9.76%	9.89%
0.64	0.0379	20.18%	6.83%	3.96%	8.89%	9.47%
0.76	0.0395	18.03%	4.46%	1.34%	6.46%	7.24%
0.86	0.0437	10.59%	3.02%	6.18%	1.14%	0.25%
0.95	0.0471	5.99%	5.52%	8.70%	4.06%	2.91%

It is clear from the Tables 2.4 and 2.5, for the central region, among different drag models, the adjusted Syamlal O'Brien drag model [16] gives the best result while the Gibilaro model [10] shows the worst result. The results from Gidaspow [14] and Huilin-Gidaspow [15] models are almost the same and located between the Syamlal O'Brien drag model [13] and Gibilaro model [10]. As for the near wall region, due to the lower radial solids holdup increase towards to the wall in the numerical results as shown in Figs 2.4 and 2.5, the difference between the numerical results and experimental data becomes smaller in the near wall region. However, the smaller difference between the numerical and experimental results does not represent a better numerical prediction since the increase trend on the radial solids holdup towards to the wall is not correctly predicted by the numerical model. Therefore, a better numerical prediction should give a lower solids concentration at the central region (which is obtained by employing the adjusted Syamlal O'Brien drag model) and a higher solids holdup at the near wall region, which leads to the investigations of the near wall treatment.

The granular temperature is also an important parameter. By applying the kinetic theory of granular phase, solids pressure and solids viscosity can be determined by the granular temperature. Generally, the granular temperature represents the random kinetic energy of particles per unit mass and it greatly depends on the particle velocity fluctuations. Therefore, a higher granular temperature reflects a higher velocity fluctuation and more intense particle collision, which results in a lower solids velocity and higher solids concentration. Figs 2.6 and 2.7 show the radial granular temperature distribution under two different operating conditions. It is obvious that the predicted granular temperature from the adjusted Syamlal O'Brien drag model [16] is lower than that from the Syamlal O'Brien drag model [13]. The granular temperatures from the Gidaspow [14] and Huilin-Gidaspow [15] drag models are almost identical and higher than that from the Syamlal O'Brien model [16]. Besides, the Gibilaro drag model [10] provides the highest radial granular temperature distribution and results in the highest solids concentration as shown in Fig 2.7.

Figure 2.6: Comparison of the radial distributions of the granular temperature using different drag models at H= 3.82m under U_l= 11.2 cm/s and U_s= 0.747 cm/s
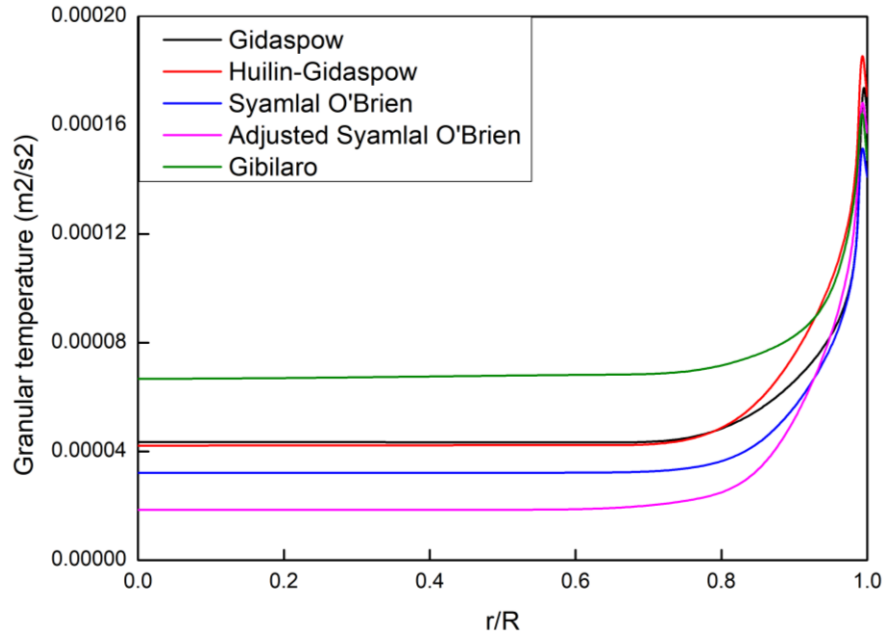

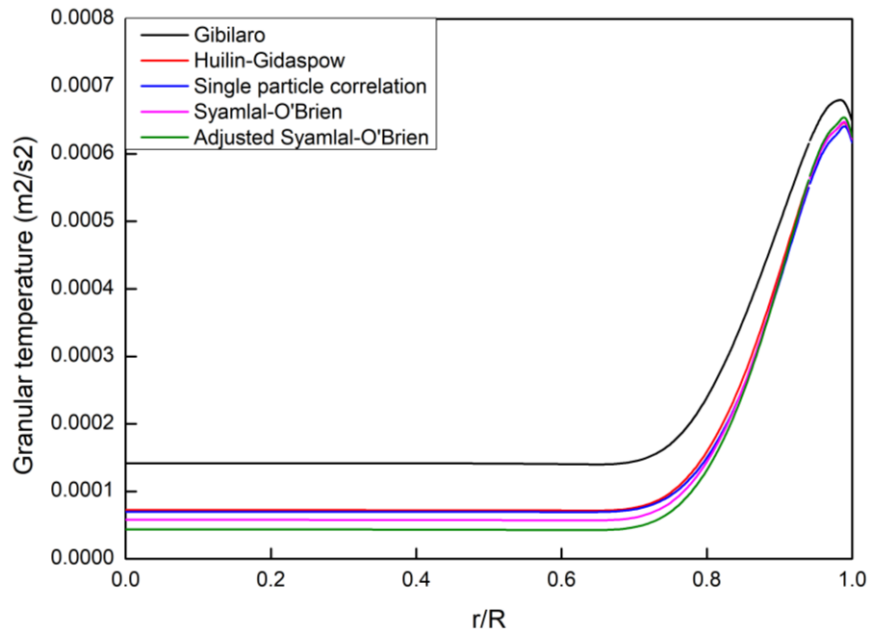**Figure 2.7: Comparison of the radial distributions of the granular temperature using different drag models at H= 1.01m under U_l= 35 cm/s and U_s= 1.193 cm/s**

From both solids holdup and granular temperature comparisons, it can be seen among all the drag models, the Gibilaro model [10] tends to provide the least accurate results. It is probably due to the fact that it was developed from the Ergun equation [9], which was based on the pressure drops of different fixed beds. Even it was modified by considering the fully expanded bed condition, it still cannot correctly represent the flow filed in LSCFBs. Besides, it is also noticed from the validation of the drag model by Gibilaro [10] that within a liquid solid fluidized bed system, it prominently improves the accuracy of the Ergun equation [9]. However, there is still significant gap between the model predictions and the experimental data. The second least accurate drag models are Gidaspow model [14] and Huilin-Gidaspow model [15]. Those two models are almost identical and were developed based on the semi-empirical correlation of Ergun equation [9] and Wen-Yu model [12]. For the LSCFB under the two operating conditions considered in this study, the bed voidage is always greater than 0.85, hence, the Wen-Yu drag model [12] is used in the Gidaspow and Huilin-Gidaspow models [14, 15]. Therefore, it is found the Wen-Yu drag model [12] performs better than Gibilaro drag model [10] but still need to improve to be applied in LSCFBs. As for the Syamlal O'Brien drag model [13], the derivation of the semi-empirical correlation was based on both gas-solid and liquid-solid fluidized beds, therefore, it can provide better predictions for the LSCFBs. However, the general drag models cannot always provide satisfactory predictions for different cases. By adjusting the parameters of $v_{r,s}$ correspondingly, the adjusted Syamlal-O'Brien drag model [16] can provide better predictions. In addition, the single particle correlation [8] can provide relatively satisfactory results, it is mainly due to the low solids concentration and homogeneous flow structures in the LSCFB, which is similar to the dilute single particulate flow.

2.5.2   Studies of the near wall treatments

Based on the comparisons between different drag models, it can be seen the distribution of the solids holdup at the central region is improved by using a more accurate drag model. However, there is no significant improvement at the near wall region. For a wall bounded flow, an accurate representation at near wall region can significantly improve the numerical results. Therefore, three different near-wall treatment methods, the scalable wall function

[17], enhanced wall treatment [17] and Menter-Lechner method [17] are investigated in this study. The comparisons for the radial solids holdup and granular temperature profiles are shown in Figs 2.8 and 2.9 under Operating Condition #2, and the difference between numerical results and experimental data is presented in Table 2.6.

Figure 2.8: Comparison of the radial distributions of the solids holdup using different near wall treatments at H= 1.01m under U_l= 35 cm/s and U_s= 1.193 cm/s

Table 2.6: Difference between the numerical results and experimental data using different near wall treatments at H=1.01m under U_l= 35 cm/s and U_s= 1.193 cm/s

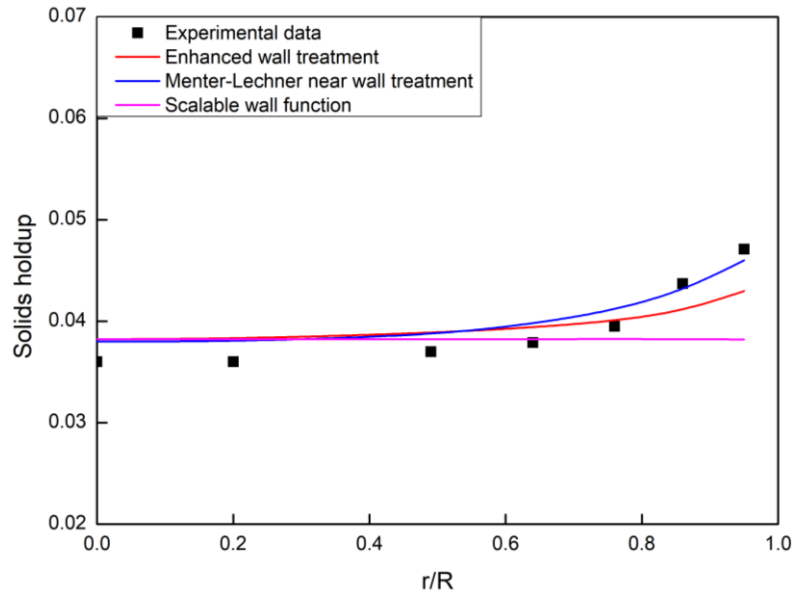| r/R	Experimental solids holdup	Enhanced wall treatment	Menter-Lechner near wall treatment	Scalable wall function
0	0.036	6.22%	5.56%	6.17%
0.2	0.036	6.31%	5.56%	6.19%
0.49	0.037	4.95%	4.35%	3.30%
0.64	0.0379	3.93%	4.85%	0.92%
0.76	0.0395	1.34%	4.00%	3.16%
0.86	0.0437	6.20%	1.60%	12.49%
0.95	0.0471	8.73%	2.34%	18.87%
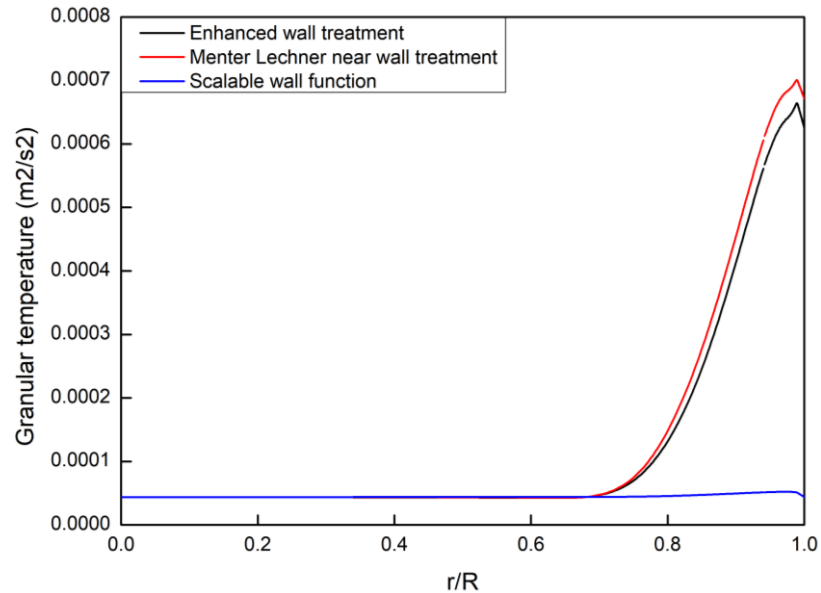
Figure 2.9: Comparison of the radial distributions of the solids granular temperature using different near wall treatments at H= 1.01m under U$_l$= 35 cm/s and U$_s$= 1.193 cm/s

It can be seen from Fig 2.8 that the Menter-Lechner near wall treatment gives the best agreement with the experimental data and the solids volume fraction at the near wall region is significantly increased. The scalable near wall function results in an almost flat solids distribution, i.e. no increase in the solids holdup at the near wall region. With the adjusted Syamlal O'Brien drag model, the solids holdup distributions at the central region using all near wall treatments show good agreements, while the difference between the numerical results using the Menter-Lechner near wall treatment and experimental data at the near wall region decreases significantly, which represents the improvement in the numerical predictions. Furthermore, from the comparison of the granular temperature shown in Fig 2.9, there is a modest increase in the granular temperature near the wall by using the Menter-Lechner near wall treatment compared with that from the enhanced wall treatment, which results in a higher velocity fluctuation and more intense particle collisions, and leads to a lower solids velocity and higher solids concentration near the wall. As for the scalable wall function, it is clear that the distributions of both solids holdup and granular

temperature are almost flat, which does not agree with the experimental data. Therefore, the scalable wall function is not suitable for the fine mesh (Y^+ is less than 1) used in this study.

To evaluate the influence of the near wall treatment on the performance of different drag models, the simulations using different drag models with the Menter-Lechner near wall treatment [17] are carried out in this study. The comparison of the radial solids holdup is shown in Fig 2.10 and the difference between numerical results and experimental data is shown in Table 2.7.
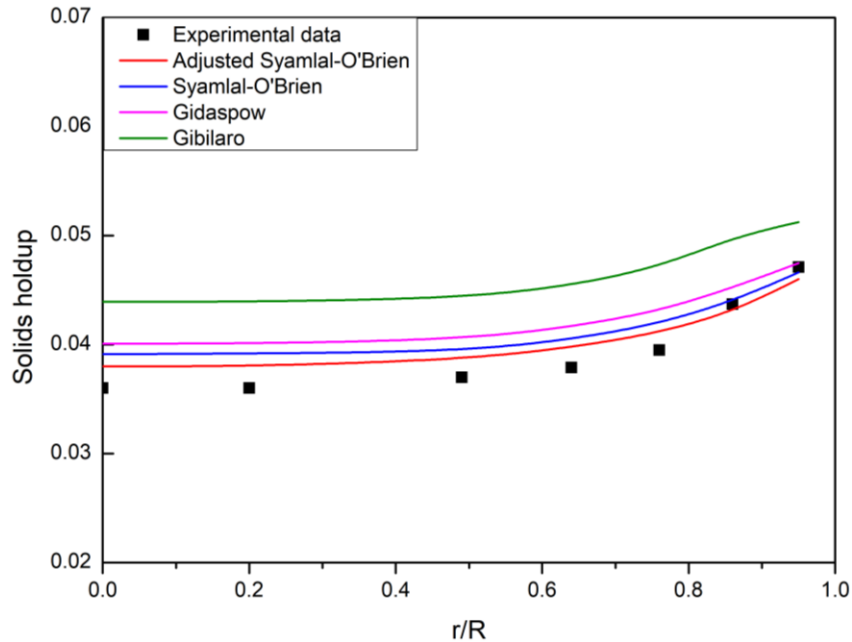
Figure 2.10: Comparison of the radial distributions of the solids holdup using different drag models at H=1.01m under U_l= 35 cm/s and U_s= 1.193 cm/s

Table 2.7: Difference between the numerical results and experimental data using different drag models at H=1.01m under U_l= 35 cm/s and U_s= 1.193 cm/s

r/R	Experimental solids holdup	Adjusted Syamlal-O'Brien	Syamlal-O'Brien	Gidaspow	Gibilaro
0	0.036	5.56%	8.67%	11.36%	22.00%
0.2	0.036	5.56%	8.83%	11.36%	22.00%

0.49	0.037	4.35%	6.41%	9.32%	19.57%
0.64	0.0379	4.85%	6.78%	9.82%	19.82%
0.76	0.0395	4.00%	6.10%	9.04%	19.27%
0.86	0.0437	1.60%	0.64%	3.46%	14.03%
0.95	0.0471	2.34%	1.04%	0.81%	8.81%
Averaged difference		4.04%	5.50%	7.88%	17.93%

It is noticed that the trend of the performance of different drag models using the Menter-Lechner near wall treatment [17] is the same as that shown in Fig 2.5 where the enhanced wall treatment was applied, i.e. the adjusted Syamlal-O'Brien drag model still provides the best numerical predictions compared with other drag models. However, it is observed the solids holdup at the near wall region is significantly improved by using the Menter-Lechner near wall treatment. In addition, it is clear as shown in Table 2.7 that using the adjusted Syamlal O'Brien drag model and Menter-Lechner near wall treatment will result in the best agreements for the numerical predictions with the experimental data.

2.5.3   Studies of the specularity and restitution coefficients

The boundary conditions are very important for the wall bounded flows, such as the multiphase flows in LSCFBs. For the liquid phase, the near wall treatment is used to resolve the flow in the near wall region. While for the solid phase, the interactions between the particles and the wall are modeled using the specularity coefficient and restitution coefficient, which are discussed in this section.

The restitution coefficient stands for the ratio of the velocity change during the collision between the particles and the wall, which is implemented in the Johnson-Jackson granular boundary conditions [18]. It varies from 0 to 1, from the inelastic collision to the elastic collision. It is found the restitution coefficient is close to unity for particles and the wall in LSCFBs due to the lubrication effect brought by liquid film [39]. Therefore, the restitution coefficients of 0.85, 0.9, 0.95 and 0.99 are investigated in this paper. Similarly, the specularity coefficient is also specified in the Johnson-Jackson boundary conditions [18]. When it is zero, the condition is described as zero shear at the wall, while the unity represents there is a significant amount of lateral momentum transfer at the wall [17]. To

investigate the sensitivity of predicted hydrodynamics to the specularity coefficient, the specularity coefficient of 0.00005, 0.0005, 0.005, 0.05 and 0.5 are selected. The comparisons of radial solids holdup distributions using different restitution and specularity coefficients are shown in Figs 2.11 and 2.12.
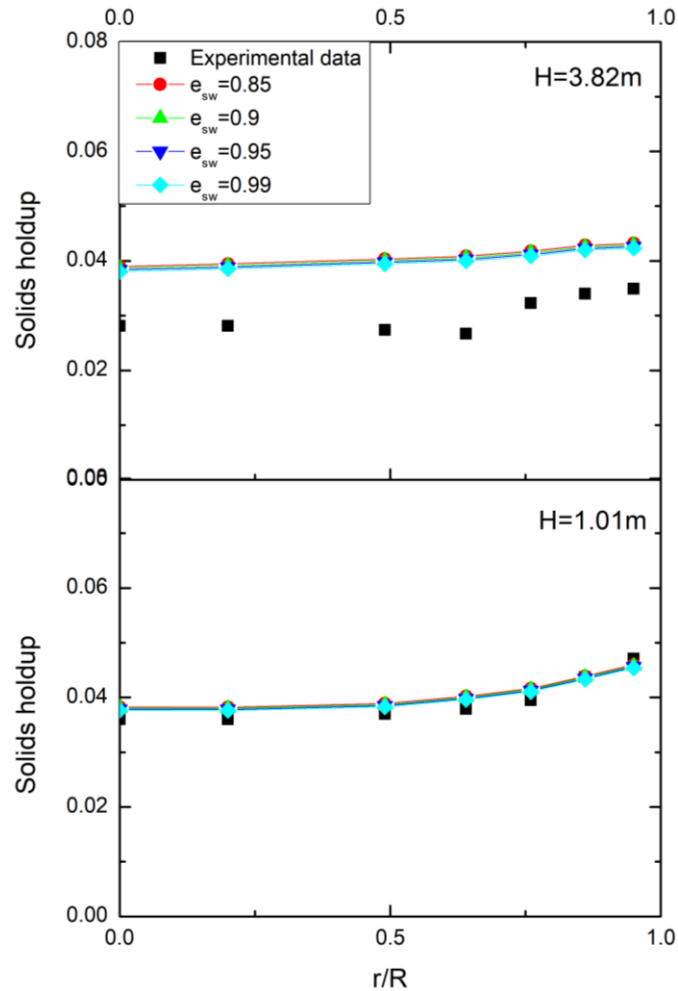
Figure 2.11: Comparisons of the radial distributions of the solids holdup using different restitution coefficients for the specularity coefficient of 0.0005 under U_l= 35 cm/s and U_s= 1.193 cm/s
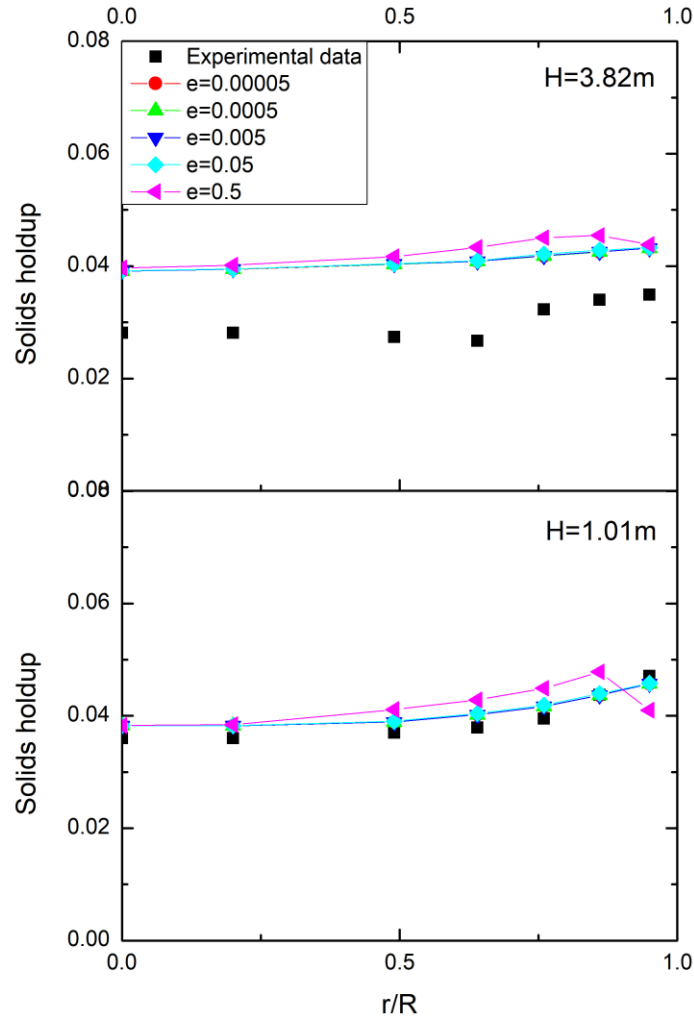
Figure 2.12: Comparisons of the radial distributions of the solids holdup using different specularity coefficient for the restitution coefficient of 0.95 under U$_l$= 35 cm/s and U$_s$=1.193 cm/s

For the restitution coefficient, it can be seen from Fig 2.11 that there is no notable variation for the radial solids holdup distributions under different restitution coefficients at both locations along the riser, which indicates the flow field in the LSCFB is not sensitive to the restitution coefficient between the particles and wall. As for the specularity coefficient, Fig 2.12 shows the comparison of the radial solids holdup under different specularity coefficients. It can be clearly seen that there is not much difference when the specularity coefficient is between 0.00005 and 0.05. However, the solids holdup increases significantly at the near wall region when the specularity coefficient is 0.5, which means within the

LSCFB system, the solids distribution is not sensitive to the specularity coefficient until it reaches a critical value. However, specularity coefficient at 0.5 is not physically possible since the particle-wall collisions in LSCFBs should be close to elastic. Therefore, the specularity coefficient and restitution coefficient are chosen as 0.0005 and 0.95 for the rest of calculations.

At last, the numerical solutions with the adjusted Syamlal-O'Brien drag model [16], the Menter-Lechner near wall treatment and the optimal values for the restitution and specularity coefficients under two different operating conditions are shown in Figs 2.13 and 2.14.
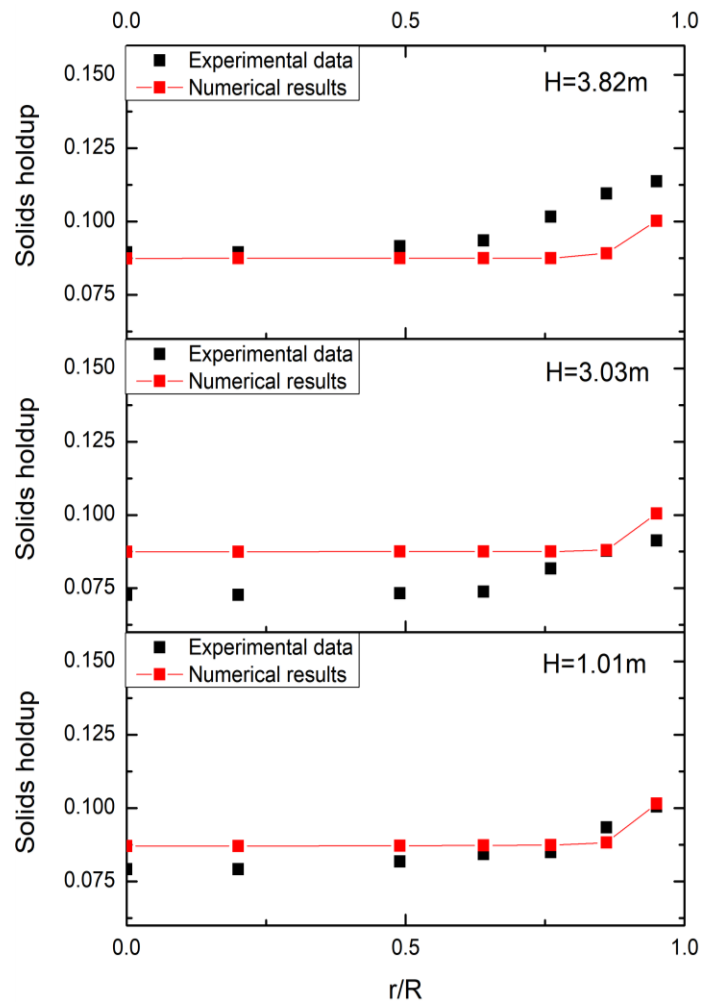
Figure 2.13: Comparisons of the radial distributions of the solids holdup under

U_l = 11.2cm/s and U_s= 0.747cm/s at different axial locations
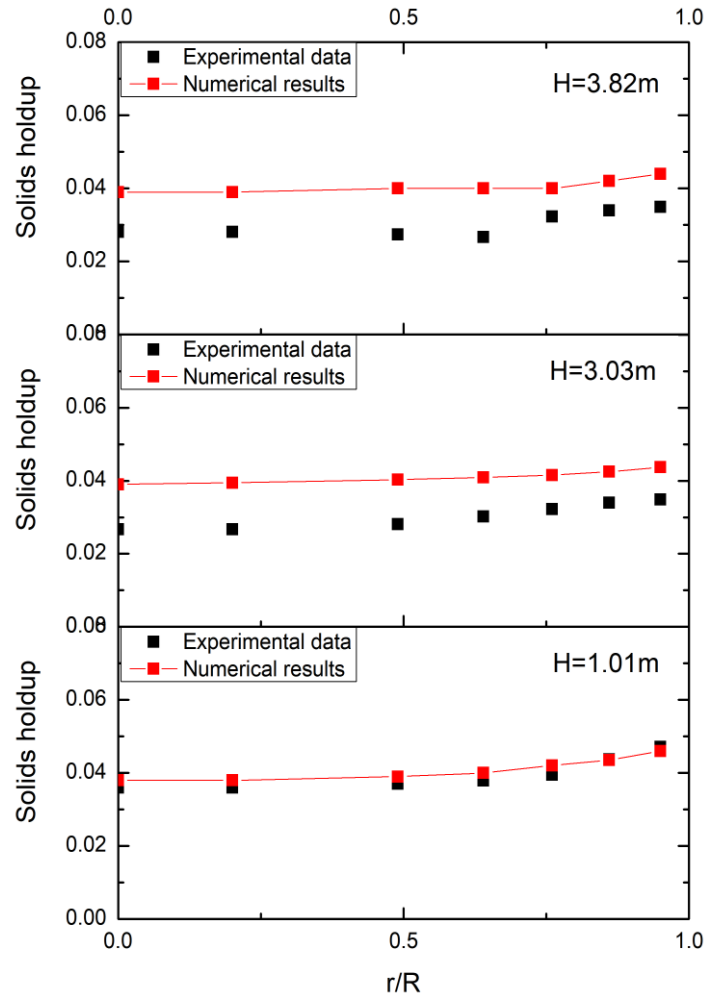
Figure 2.14: Comparisons of the radial distributions of the solids holdup under
U_l = 35cm/s and U_s =1.193cm/s at different axial locations

It can be seen the simulation results of both operating conditions at different heights have good agreements with the experimental data, i.e. lower solids concentration at the central region and higher solids concentration near the wall. However, with the increase of the height along the riser, the agreement between the numerical results and experimental data is not as good as those at the lower part of the riser.

2.5.4   Studies of the drag model for irregular particles

Since irregular particles are often used in industrial applications and the sphericity of the particles will affect the hydrodynamics within the LSCFB system, it is essential to take the

sphericity into consideration during the design or scale-up of the fluidized bed. In the present work, to investigate the influence of the particle shapes on the drag models. The simulations are carried out by employing the modified drag model for irregular particles with the Menter-Lechner near wall treatment and Johnson-Jackson boundary conditions under the Operating Condition #3 in Table 2.1. The numerical results are compared with the experimental data. In addition, the adjusted Syamlal O'Brien model [16], where c_1 and d_1 are adjusted to 0.282 and 9.074, respectively, for Operating Condition #3 with irregular particles, is also implemented to see how it works for irregular particles in the LSCFB system.

The comparisons for radial solids holdup profiles using different drag models are shown in Fig 2.15.
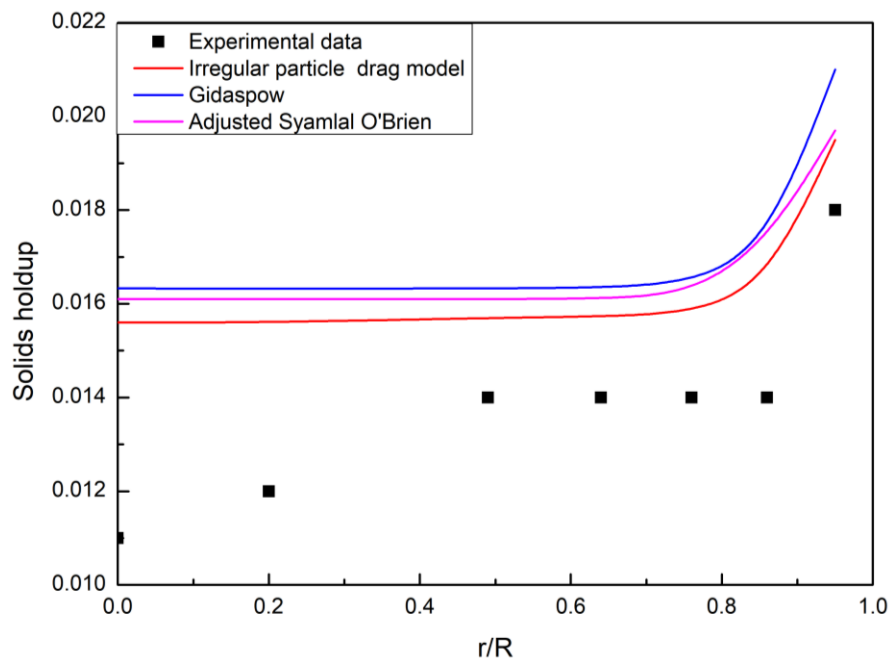
Figure 2.15: Comparison of the radial distributions of the solids holdup for different drag models at H=3.98m under U_l=28 cm/s and U_s=0.4 cm/s with irregular particles

It is clear the radial solids holdup distribution for irregular plastic beads has the analogous manner as spherical glass beads, i.e. lower solids concentration at the central region and higher solids concentration near the wall, which indicates different particle shapes will not

alter the basic hydrodynamic behaviors of the LSCFB system. For the numerical predictions, all the simulations tend to overestimate the solids holdup compare to the experimental data. Among those different drag models, it is obvious the irregular particle drag model gives the best results, the adjusted Syamlal O'Brien model [16] is the next best one, and followed by the Gidaspow model [14]. Besides, due to the use of the Menter-Lechner near wall treatment, the radial solids concentration near the wall shows good agreement with the experimental data.

The radial granular temperature distributions using different drag models under Operating Condition #3 are shown in Fig 2.16.
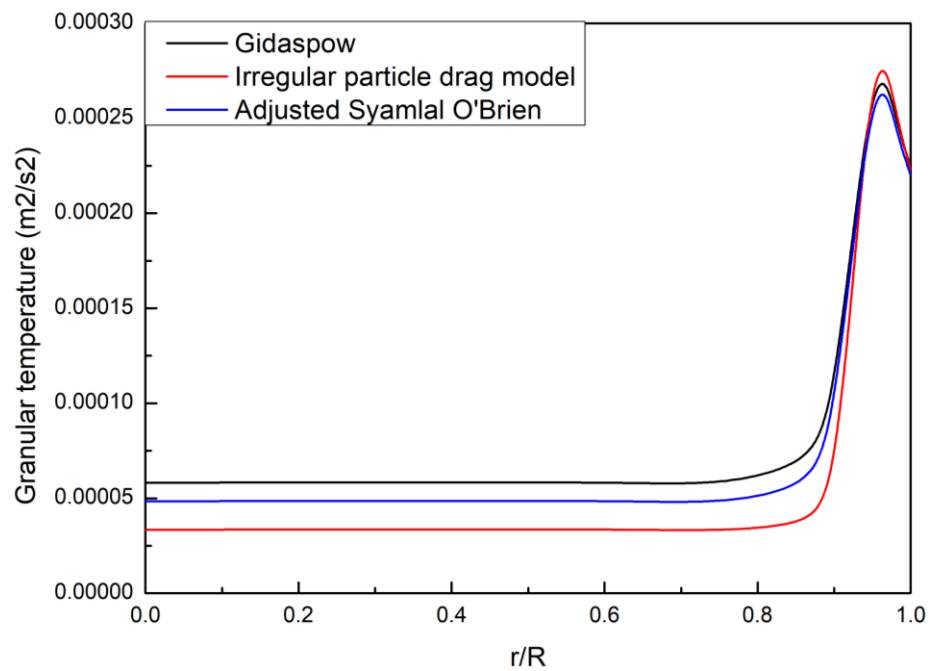
Figure 2.16: Comparison of the radial distributions of the granular temperature using different drag models at H=3.98m under U$_l$=28 cm/s and U$_s$=0.4 cm/s with irregular particles

It is obvious that the granular temperature from the irregular particle drag model is lower than the adjusted Syamlal O'Brien model [16] drag model and the Gidaspow [14] drag model gives the highest granular temperature distribution. The predictions of the granular temperature are consistent with the solids holdup distributions.

It can be seen among all the drag models, the Gidaspow drag model [14] always gives the least accurate results. It is reasonable as mentioned in the previous section, when the bed voidage is greater than 0.85, the Wen-Yu drag model [12] is used and it does not take the shape factor into consideration. Therefore, the Gidaspow drag model [14] is not suitable for the irregular LSCFB system. As for the adjusted Syamlal O'Brien drag model [16] and the irregular particle drag model, they are obtained by the same concept, which is by implementing the velocity-voidage function to the single particle drag correlation to obtain the drag model for multi-particle systems. For the adjusted Syamlal O'Brien drag model [16], both the single particle drag model from Dalla Valle [38] and velocity-voidage function from Garside and Al-Dibouni [37] were obtained based on spherical particles in gas or liquid-solid systems. Therefore, by modifying c_1 and d_1 which depend on particle properties, there is improvement for the adjusted Syamlal O'Brien drag model [16] compared with the Gidaspow drag model [14]. However, for the irregular particle drag model, the sphericity has been directly taken into consideration in both single particle drag model and velocity-voidage function. The single non-spherical particle drag model is adopted from Haider and Levenspiel [25] which was obtained from 419 isometric data points for $\text{Re} < 2.5 \times 10^5$ (including irregular particles like octahedrons, cubes, tetrahedrons, disks, etc.) and 408 data points for $\text{Re} < 2.6 \times 10^5$ (including spherical particles to test the applicability when the sphericity is 1). Then, the velocity-voidage function is chosen from Cleasby and Fan [30], which was obtained from the experimental studies for irregular particles such as sand, anthracite and flints, etc. Therefore, by directly taking sphericity into consideration, the irregular particle based semi-empirical drag model is more accurate than the adjusted Syamlal O'Brien drag model [16], which was based on the spherical particles.

2.6 Conclusions

A numerical study has been carried out in this work on the effects of the drag models, near-wall treatments and wall boundary conditions on the predictions of the turbulent liquid-solid two-phase flows in a fluidized bed. For the spherical particle systems, it is found that the adjusted Syamlal-O'Brien drag model [16] provides the best agreement with the experimental data at the central region while the Menter-Lechner near wall treatment gives

a more realistic solution at the near wall region. In addition, the numerical predictions are not sensitive to the specularity coefficient and restitution coefficient. For the irregular particle systems, it is concluded that by including the shape factor into the single non-spherical particle drag model and velocity-voidage function to account for the effect of the irregular particles, it can improve the agreements between the numerical and experimental results. In future works, the comprehensive numerical model proposed in this study will be adopted to investigate the influence of the superficial liquid velocity, superficial solid velocity and particle density acts on the hydrodynamics of LSCFBs

.

References

[1] Razzak, S.A. 2009, Hydrodynamic studies in liquid-solid and gas-liquid-solid circulating fluidized beds, The University of Western Ontario (Canada).

[2] A. Atta, S.A. Razzak, K.D.P. Nigam, J.X. Zhu, (Gas)–liquid–solid circulating fluidized bed reactors: characteristics and applications, Ind. Eng. Chem. Res. 48 (2009) 7876–7892.

[3] Wang, Wei, et al. "A review of multiscale CFD for gas–solid CFB modeling." International Journal of Multiphase Flow 36.2 (2010): 109-118.

[4] Hartge, Ernst-Ulrich, et al. "CFD-simulation of a circulating fluidized bed riser." Particuology 7.4 (2009): 283-296.

[5] Sinclair, J. L., and R. Jackson. "Gas-particle flow in a vertical pipe with particle-particle interactions." AIChE Journal 35.9 (1989): 1473-1486.

[6] Ding, Jianmin, and Dimitri Gidaspow. "A bubbling fluidization model using kinetic theory of granular flow." AIChE journal 36.4 (1990): 523-538.

[7] H. Enwald et al. Eulerian two phase flow theory applied to fluidization. International Journal of Multiphase Flow 22(1), pp. 2166. 1996. DOI: 10.1016/S0301-9322(96)90004X.

[8] Lewis W K, Gilliland E R and Lang P M (1962). Entrainment from fluidized bed, chem. Eng. Prog. Symp. Ser., 58(38) 65-78.

[9] van Sint Annaland M, Bokkers GA, Goldschmidt MJV, Olaofe OO, van der Hoef MA, Kuipers JAM. Development of a multi-fluid model for poly-disperse dense gas–solid fluidized beds, part II: segregation in binary particle mixtures. Chem. Eng. Sci 2009; 64:4237–46.

[10] Gibilaro LG, Di Felice R, Waldram SP, Foscolo PU. Generalized friction factor and drag coefficient correlations for fluid particle interactions. Chemical Engineering Science. 1985;40(10):181723.

[11] Richardson JF, Zaki WN. Sedimentation and fluidization: Part I. Process Safety and Environmental Protection: Transactions of the Institution of Chemical Engineers, Part B. 1997;75: S82S100.

[12] C.-Y. Wen and Y. H. Yu. "Mechanics of Fluidization". Chem. Eng. Prog. Symp. Series. 62.100-111.1966.

[13] M. Syamlal and T.J. O'Brien. The derivation of a drag coefficient formula from velocity-voidage correlations. Technical Note, U.S. Department of energy, Office of Fossil Energy, NETL, Morgantown, WV, April 1987.

[14] Gidaspow, D., 1994, Multiphase Flow and Fluidization: Continuum and Kinetic Theory Descriptions, Academy, Boston, MA.

[15] L. Huilin and D. Gidaspow. "Hydrodynamics of binary fluidization in a riser: CFD simulation using two granular temperatures". Chemical Engineering Science. 58. 3777-3792. 2003.

[16] Syamlal, M., and O'Brien, T., 2003, "Fluid Dynamic Simulation of O3 Decomposition in a Bubbling Fluidized Bed," AIChE J., 49_11_, pp. 2793–2801.

[17] Ansys Fluent. Fluent 16.0 User's Guide.

[18] P. C. Johnson and R. Jackson. "Frictional-Collisional Constitutive Relations for Granular Materials, with Application to Plane Shearing". J. Fluid Mech. 176. 67-93.1987.

[19] Wadell H (1933). Sphericity and Roundness of Rock Particles, J. Geol. 41 310-331.

[20] Heywood, H. J. Imp. Oollege Chem. Eng. Soc., 1948,4,17.

[21] Briggs, L. T., McCulloch, D. S. and Moser, F- The hydraulic shape of sand particles. Journal of Sedimentary Petrology, 32 (1962), 645-657.

[22] B. Huner, R.G. Hussey, Phys. Fluids 20 _1977. 1211.

[23] T.J. Ui, R.G. Hussey, R.P. Roger, Phys. Fluids 27 _1984. 787.

[24] R. Shail, D.J. Norton, Proc. Camb. Phil. Soc. 65 _1969. 793.

[25] Haider A and Levenspiel O. Drag coefficient and terminal velocity of spherical and nonspherical particles. Powder Technol 1989; 58: 63–70.

[26] Ganser G. A rational approach to drag prediction of spherical and nonspherical particles. Powder Technol 1993; 77: 143–152.

[27] P.K. Swamee, C.P. Ojha, J. Hyd. Eng. 117 _1991. 660.

[28] Chien S. Settling velocity of irregularly shaped particles. Soc Petrol Eng Drilling Completion 1994; 9: 281–289.

[29] Tran-Cong S, Gay M and Michaelides E. Drag coefficients of irregularly shaped particles. Powder Technol 2004; 139: 21–32.

[30] Cleasby, J. L. and Fan, K. S. Predicting fluidization and expansion of filter media. Journal of the Sanitary Engineering Division, American Society of Civil Engineers, 107 (1981), 455-471.

[31] Dharmarajah, Anthonisamy Herman, "Effect of particle shape on prediction of velocity-voidage relationship in fluidized solid-liquid systems " (1982). Retrospective Theses and Dissertations. 7535.

[32] Sang L. Particle fluidization in upward and inverse liquid-solid circulating fluidized bed [dissertation]. London, Ont: School of Graduate and Postdoctoral Studies, University of Western Ontario; 2013.

[33] Dadashi A, Zhu J, Zhang C. A computational fluid dynamics study on the flow field in a liquid-solid circulating fluidized bed riser. POWDER TECHNOLOGY. 2014;260:528.

[34] Lun, C.K.K., Savage, S.B., Jeffrey, D.J. and Chepurniy, N., 1984, Kinetic theories for granular flow: inelastic particles in Couette flow and slightly inelastic particles in a general flow field, J Fluid Mech, 140: 223.

[35] Syamlal, M., W. Rogers and T. J. O′Brien, "MFIX Documentation Theory Guide," U.S. Department of Energy Office of Fossil Energy Morgantown Energy Technology Center, Morgantown, WV (1993).

[36] D.G. Schaeffer, Instability in the evolution equations describing incompressible granular flow, J. Diff. Eqs. 66 (1987) 19–50.

[37] J. M. Dalla Valle. Micromeritics. Pitman, London. 1948.

[38] Garside, J. and M. R. Al-Dibouni, "Velocity–Voidage Relationship for Fluidization and Sedimentation," Ind. Eng. Chem. Proc. Des. Dev. 16(2), 206–214 (1977).

[39] Y. Cheng and J. Zhu, "CFD Modelling and Simulation of Hydrodynamics in Liquid‐Solid Circulating Fluidized Beds," The Canadian Journal of Chemical Engineering, vol. 83, pp. 177-185, 2005.

Chapter 3

3 Numerical Investigations of Hydrodynamics in Liquid-Solid Circulating Fluidized Beds under Different Operating Conditions

3.1 Introduction

Fluidization is characterized as an operation in which solid particles are suspended in gas or liquid flows and converted from the solid-like state to the fluid-like state. Based on the characterization of fluid medias, fluidization can be cataloged as gas-solid fluidization, liquid-solid fluidization and gas-liquid-solid fluidization. The liquid-solid fluidization is formed when the solid particles are fluidized by the lift effect of vertical upward liquid flows. With the unique liquid-solid contacting features of the particle suspension, numerous advantages are introduced in the liquid-solid fluidized bed, such as higher contact efficiency, excellent mass and heat transfer and so on. With decades of development, the liquid-solid fluidized bed (LSFB) reactors have obtained extensive attractions in diverse fields of industrial process, such as in biochemical technology, wastewater treatment, petroleum and metallurgical industries [1].

For the liquid-solid fluidized bed, with the increase of liquid velocity, the fluidization will go through the fixed bed regime, the conventional fluidization regime, the circulating fluidization regime and the dilute transport regime. For a suspension of a bed of particles, the drag force acting on particles should balance their weights, which is defined as the minimum fluidization velocity condition, U_{mf}. For the liquid velocity lower than U_{mf}, it is within the fixed bed regime. Increasing the liquid velocity beyond the U_{mf} leads to the suspension of particles and the conventional fluidization regime is obtained. Further increasing liquid velocity, it reaches the circulating fluidization regime where most of particles can be entrained out of the bed and needed to recirculate back to the bottom of the bed. With further increase of liquid flow rate, the dilute transport regime is formed.

The hydrodynamics of each fluidization regime are different. The conventional fluidized bed has been studied extensively by lots of researchers. In terms of the flow structures, it

is widely observed that there is a clear boundary between the dense region at the bottom and the freeboard region at the top of the bed. With the increase of the liquid flow rate, the boundary between dense and dilute region raises with the homogeneous expansion of the bed. In 1985, Couderc [2] found the conventional fluidization can be considered as a dispersed homogenous fluidization where particles are uniformly distributed in both the axial and radial directions in the dense phase.

Few works have been concentrated on the hydrodynamics of the liquid-solid circulating fluidized bed (LSCFB). For the axial hydrodynamic behaviors, Liang et al. [3], Zheng [4] and Razzak [5] reported the uniform axial solids holdup distribution under different operating conditions for light particles. However, it can be observed the non-uniformity of axial distribution increases with the increase of particle density. In addition, the overall cross-sectional average solid holdup increases with the increase of particle diameter and decreases with the increase of superficial liquid velocity. For the radial hydrodynamic behaviors, the radial non-uniformity of solids holdup distribution for glass beads is found by Liang and Zhu [6] and Roy et al. [7], which is presented as lower solids concentration at the central region and higher solids holdup near the wall. Zheng [8], Razzak [5] and Sang [9] extended the investigations for different operating conditions and particle properties, it is found the radial non-uniformity decreases with the increase of superficial liquid velocity and increases with the increase of superficial solid velocity. Besides, the particle size, density and sphericity have considerable influence on the hydrodynamics in LSCFB as well. All in all, although there are some radial or axial nonuniformities exist in LSCFB under some operating conditions, the flow structures of liquid-solid circulating fluidized bed are more homogeneous than the distributions in gas-solid circulating fluidized bed.

To properly design and apply a liquid-solid circulating fluidized bed (LSCFB) for industrial purpose, it is necessary to model and scale up the hydrodynamics of LSCFBs. Start from 1950s, a series of mathematical models has been proposed, such as the two-phase model for conventional fluidized beds and core-annulus model for circulating fluidized beds. However, those models cannot correctly and comprehensively solve the flow field of a complex system in fluidized beds. Therefore, the computational fluid dynamics (CFD) modeling has become an effective tool to investigate the hydrodynamics

inside a CFB riser with the fast development of computer technology and multiphase flow models [10-13].

Generally, there are two major theories of describing gas-solid and liquid-solid two-phase flows: (1) the Eulerian-Lagrangian (E-L) approach where the particulate trajectory model is used for the solid-phase and the particle-particle interactions are neglected and (2) the Eulerian-Eulerian (E-E) approach where two-fluid model is used for both phases. In this work, the Eulerian-Eulerian approach is employed since the solid volume fraction in LSCFBs is high and the interactions between particles need to be considered. By incorporating kinetic theory of granular phase (KTGP), the Eulerian-Eulerian based CFD model considers both fluid and solid phases as the interpenetrating continuum, and solves Mass and Momentum governing equations which are closed by the constitutive equations within a fixed control volume containing both phases [14].

A few numerical studies have been conducted on the liquid-solid multiphase flows recently. Roy et al [15] simulated the flow field in LSCFB by the Eulerian two-phase flow model with the KTGP and examined the model with the experimental data. Cheng [16] did a parametric study on the particle-particle and particle-wall restitution coefficients for LSCFBs in 2005. Later, Cornelissen [17] worked on the conventional fluidized bed and investigated the influence of the inlet distributor, restitution coefficients and two different drag models. In 2014, Abbas [18] investigated the influence of three different k-ε turbulence models for LSCFBs. Nevertheless, more numerical studies are required to systematically investigate and improve the CFD models. Therefore, in previous chapter, a detailed study is conducted on the drag models, near wall treatments and boundary conditions due to the lack of studies in past years.

In this work, a numerical study on the hydrodynamics of LSCFBs under different operating conditions and particle properties is carried out. The proposed CFD model from Chapter 2 is applied. The numerical results for the influence of different superficial solid velocities and particle densities are compared with the available experimental data from Razzak [5] and Sang [9], and the influence of different superficial liquid velocities is discussed with the previous experimental observations.

3.2   Experimental setup of the LSCFB system

The experimental studies on the liquid-solid two-phase flows in LSCFB by Razzak [5] and Sang [9] are simulated in the present work to investigate the hydrodynamic behaviors of the LSCFB riser and compared with experimental data.

The schematic diagram of the experimental setup is presented in Fig 3.1. It consists of two main sections: riser and downer. The riser is made of Plexiglas with 5.4m in height and 0.0762m in diameter, and the downer is made of Plexiglas as well with 5.05m in height and 0.2m in diameter. The liquid-solid separator is located at the top of the riser for separating the entrained solids from the liquid and the solids circulation rate measurement device is located near the top of the downer. At the bottom of the riser, there are two liquid distributors, the seven primary liquid distributors are occupying 19.5% of the cross-sectional bed area and extending 0.2m into the riser, and the auxiliary liquid distributor at the bottom is a porous plate with 4.8% of opening area and controls the recirculating particles flow rate.

The particles are injected from the solids feed pipe, by adjusting the auxiliary flow rate, the quantity of recirculating particles from the storage vessel can be controlled, that is when auxiliary liquid velocity is zero, there will be no particles enter the riser. Introducing the auxiliary liquid flow to start feeding particles and with the lifting effect from both auxiliary liquid and primary liquid, all particles can be fluidized and entrained out of the riser. Then they are separated from the liquid in the liquid-solid separator, and ejected into the downer, finally reach to the solids feed pipe again and complete the circulation.
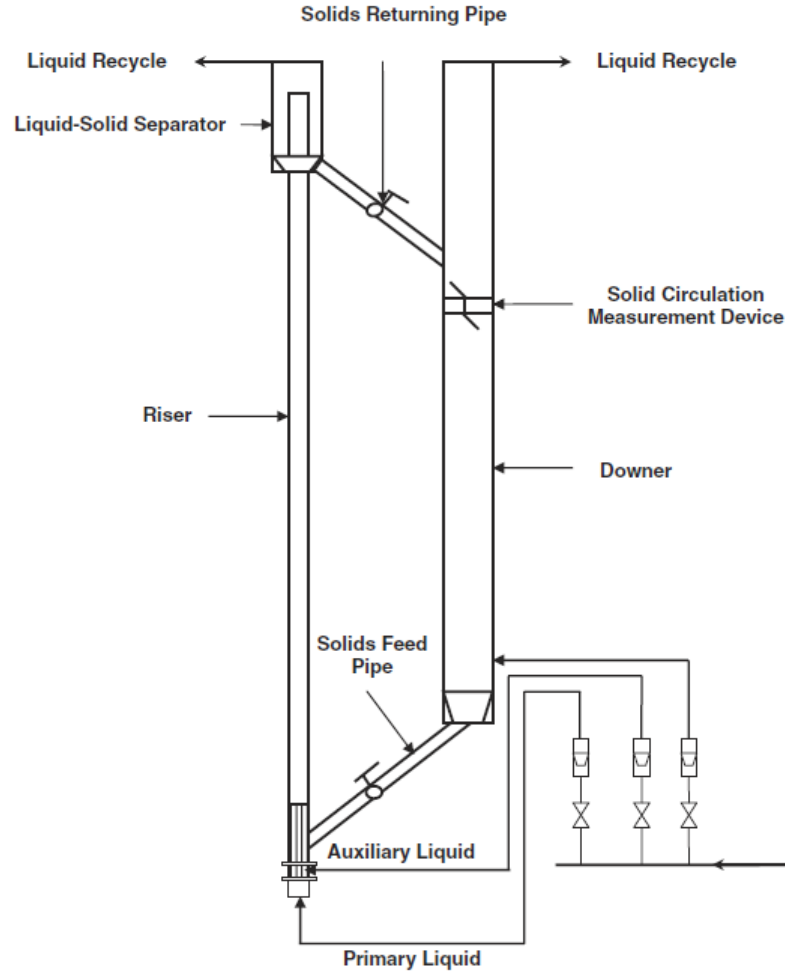
Figure 3.1: Experimental setup for the LSCFB riser

In this study, experiments under different operating conditions are simulated to study the general hydrodynamics and flow patterns of hydrodynamic behaviors for the LSCFB riser. The detailed operating conditions and physical properties of the particles and liquid are listed in Table 3.1. All the simulations are conducted under the ambient temperature and tap water. The operating condition under U_l=11.2cm/s and U_s=0.95cm/s has been chosen as anchoring point. By varying the superficial solid velocity, the hydrodynamics from numerical predictions are compared with experimental data from Razzak [5], by varying the superficial liquid velocity, the numerical results are discussed with the expected hydrodynamics. Furthermore, the influence of particle density is investigated under the operating condition U_l=28cm/s and U_s=0.4cm/s by Sang [9]. It should be noted the operating condition under U_l=11.2cm/s, U_s=0.978cm/s is regarded as U_s=0.95 cm/s since the difference can be neglected.

Table 3.1 Operation conditions and physical properties of the particles and liquid

	U_l (cm/s)	U_s (cm/s)	Liquid phase density (kg/m^3)	Liquid phase viscosity (kg/m^{-s})	Particle diameter (mm)	Particle density (kg/m^3)	Particle sphericity
Razzak [5] - glass beads	11.2	0.747	998.2	0.001003	0.5	2500	1
		0.95					
		1.121					
	35	1.193					
		1.718					
	8.4	0.95					
	11.2						
	22.4						
Sang [9] - plastic beads	28	0.4			0.58	1330	0.7
						1520	

3.3 Numerical models

The Eulerian-Eulerian based CFD model is used to solve the governing equations of both continuous liquid phase and discrete solid phase. The governing equation for the continuous liquid phase is closed by the k-ε turbulence model and the governing equation for the discrete solid phase is closed by the models based on kinetic theory of granular phase (KTGP). Those constitutive equations are derived based on different theoretical assumptions and empirical equations.

3.3.1 Governing equations

The continuity and momentum equations are given as:

$$\frac{\partial}{\partial t}\left(\alpha_q \rho_q\right)+\nabla\bullet\left(\alpha_q \rho_q \vec{v_q}\right)=0, \ \sum_q \alpha_q =1 \tag{1}$$

$$\frac{\partial}{\partial t}\left(\alpha_l \rho_l \vec{v_l}\right)+\nabla\bullet\left(\alpha_l \rho_l \vec{v_l}^2\right)=-\alpha_l \nabla p +\nabla\bullet\overline{\overline{\tau_l}}+\alpha_l \rho_l \vec{g}+K_{sl}\left(\vec{v_s}-\vec{v_l}\right)$$

$$\overline{\overline{\tau_l}}=\alpha_l \mu_l \left(\nabla\bullet\vec{v_l}+\nabla\bullet\vec{v_l}^T\right)$$

$$\frac{\partial}{\partial t}\left(\alpha_s \rho_s \vec{v_s}\right)+\nabla\bullet\left(\alpha_s \rho_s \vec{v_s}^2\right)=-\alpha_s \nabla p +\nabla p_s +\nabla\bullet\overline{\overline{\tau_s}}+\alpha_s \rho_s \vec{g}+K_{ls}\left(\vec{v_l}-\vec{v_s}\right)$$

$$\overline{\overline{\tau_s}}=\alpha_s \mu_s \left(\nabla\bullet\vec{v_s}+\nabla\bullet\vec{v_s}^T\right)+\alpha_s \left(\lambda_s -\frac{2}{3}\mu_s\right)\nabla\bullet\vec{v_s}\overline{\overline{I}} \tag{2}$$

Where α_q is the volume fraction of phase q.

For the continuous liquid phase, a k-ε turbulence model is employed to close the governing equations. Since the dispersed k-ε model for the liquid phase is computationally less expensive and it predicts the hydrodynamic quantities equally well as the per-phase turbulence model [17], it is used in the simulations and is given as

$$\frac{\partial}{\partial t}\left(\alpha_l \rho_l k_l\right)+\nabla\bullet\left(\alpha_l \rho_l \vec{v_l} k_l\right)=\nabla\bullet\left(\alpha_l \frac{\mu_{t,l}}{\sigma_k}\nabla k_l\right)+\alpha_l G_{k,q}-\alpha_l \rho_l \varepsilon_l -K_{sl}\left(2k_l -\sqrt{2k_l}\sqrt{3\Theta_s}\right)$$

$$\frac{\partial}{\partial t}\left(\alpha_l \rho_l \varepsilon_l\right)+\nabla\bullet\left(\alpha_l \rho_l \vec{v_l}\varepsilon_l\right)=\nabla\bullet\left(\alpha_l \frac{\mu_{t,l}}{\sigma_\varepsilon}\nabla\varepsilon_l\right)+\alpha_l \frac{\varepsilon_l}{k_l}\left(C_{1\varepsilon}G_{k,l}-C_{2\varepsilon}\rho_l \varepsilon_l\right)-C_{2\varepsilon}\frac{\varepsilon_l}{k_l}K_{ls}\left(2k_l -\sqrt{2k_l}\sqrt{3\Theta_s}\right) \tag{3}$$

For the solid phase, the kinetic theory of granular phase (KTGP) is employed to model the viscosity, stresses and pressure of the solid phase used in the momentum conservation equation. Based on the KTGP, the viscosity, pressure and stresses for the solid phase can be determined by the granular temperature, which is the mean square of a random particle velocity. Thus, the inter-particle interactions can be described theoretically and calculated. The constitutive equations for the solid phase are summarized in Table 3.2.

Table 3.2 The constitutive correlations for the transport equations

Solids pressure	$P_s = \alpha_s \rho_s \Theta_s + 2\rho_s \left(1+e_{ss}\right)\alpha_s^2 g_{O,ss}\Theta_s$	(Lun et al. [18])
Radial distribution function	$g_{O,ss} = \left[1-\left(\dfrac{\alpha_s}{\alpha_{s,\max}}\right)^{1/3}\right]^{-1}$	(Ding and Gidaspow [13])
Solids shear stress	$\mu_s = \mu_{s,col} + \mu_{s,kin} + \mu_{s,fr}$	
Collisional viscosity	$\mu_{s,col} = \dfrac{4}{5}\alpha_s \rho_s d_s g_{O,ss}\left(1+e_{ss}\right)\sqrt{\dfrac{\Theta_s}{\pi}}$	(Gidaspow et al. [20])
Kinetic viscosity	$\mu_{s,kin} = \dfrac{\alpha_s \rho_s d_s \sqrt{\Theta_s \pi}}{6\left(3+e_{ss}\right)}\left[1+\dfrac{2}{5}\left(1+e_{ss}\right)\left(3e_{ss}-1\right)\alpha_s g_{O,ss}\right]$	(Syamlal et al. [21])
Frictional viscosity	$\mu_{s,fr} = \dfrac{P_s \sin\phi}{2\sqrt{I_{2D}}}$	(Schaeffer [22])
Bulk viscosity	$\lambda_s = \dfrac{4}{3}\alpha_s^2 \rho_s d_s g_{O,ss}\left(1+e_{ss}\right)\sqrt{\dfrac{\Theta_s}{\pi}}$	(Lun et al. [19])
Granular conductivity	$k_{\Theta s} = \dfrac{15 d_s \rho \alpha_s \sqrt{\Theta_s \pi}}{4\left(41-33\eta\right)}\left[1+\dfrac{12}{5}\eta^2\left(4\eta-3\right)\alpha_s g_{O,ss} + \dfrac{16}{15\pi}\left(41-33\eta\right)\eta \alpha_s g_{O,ss}\right]$ $\eta = \dfrac{1}{2}\left(1+e_{ss}\right)$	(Syamlal et al. [21])
Collisional dissipation of energy	$\gamma_{\Theta s} = \dfrac{12\left(1-e_{ss}^2\right)g_{O,ss}}{d_s \sqrt{\pi}}\rho_s \alpha_s^2 \Theta_s^{3/2}$	(Lun et al. [19])

3.3.2   Drag models

The drag force is one of the dominate terms in momentum equations and represents the momentum exchange between phases. According to the investigations for drag models in chapter 2, the adjusted Syamlal O'Brien drag model [26] and irregular particle drag model are most suitable for the spherical and irregular particles in LSCFB systems respectively. The derivations and equations are presented below.

Syamlal O'Brien drag model [23]:

Both adjusted Syamlal O'Brien drag model [26] and irregular particle drag model are based on modifications upon Syamlal O'Brien drag model [23]. The Syamlal O'Brien drag model correlated the drag models for multi-particle system and single particle system by the velocity-voidage function.

For several separated particles flow separately in a fluid within a control volume, the fluid-solid exchange coefficient can be written as:

$$K_{ls} = \frac{3\rho_g \alpha_g \left(1-\alpha_g\right)}{4d_p} C_D \left|\vec{u_s} - \vec{u_g}\right| \tag{4}$$

However, this equation doesn't take particle interactions into consideration, while the fluidized bed is a multi-particle system which is far more complicated than the individual particulate flow. Therefore, Syamlal O'Brien introduce the velocity-voidage function V_r to bridge the two different systems as follow:

$$C_D(\mathrm{Re}, \varepsilon) = \frac{C_{Ds}(\mathrm{Re}/V_r)}{V_r^2} \tag{5}$$

Here the C_{Ds} stands for drag coefficient of single particle system while the C_D represents drag coefficient for multi-particle system. In Syamlal O'Brien drag model, the drag coefficient from Dalla Valle [24] and velocity-vodiage function form Garside and Al-Dibouni [25] are adopted. Therefore, the final drag correlation is presented as follow.

The fluid-solid exchange coefficient K_{ls} is defined as

$$K_{sl} = \frac{3\alpha_s \alpha_l \rho_l}{4 v_{r,s}^2 d_s} C_D \left(\frac{\text{Re}_s}{v_{r,s}} \right) \left| \vec{v_s} - \vec{v_l} \right|$$

(6)

where the drag coefficient is brought by Dalla Valle [24]

$$C_D = \left(0.63 + \frac{4.8}{\sqrt{\text{Re}_s / v_{r.s}}} \right)^2$$

(7)

And the relative Reynolds number has the form as

$$\text{Re}_s = \frac{\rho_l d_s \left| \vec{v_s} - \vec{v_l} \right|}{\mu_l}$$

(8)

The velocity-voidage correlation $v_{r,s}$ is from Garside and Al-Dibouni [25]

$$\frac{v_{r,s} - A}{B - v_{r,s}} = 0.06 \,\text{Re}_s$$

(9)

where

$$A = \alpha_l^{4.14}$$

$$B = \begin{cases} c_1 \alpha_l^{1.28} & \alpha_l \leq 0.85 & c_1 = 0.8 \\ \alpha_l^{d_1} & \alpha_l > 0.85 & d_1 = 2.65 \end{cases}$$

By substituting $v_{r,s} = \text{Re}/\text{Re}_s$ in Eq. (9), we get

$$v_{r,s} = 0.5 \left(A - 0.06 \,\text{Re} + \sqrt{\left(0.06 \,\text{Re} \right)^2 + 0.12 \,\text{Re} \left(2B - A \right) + A^2} \right)$$

(10)

Adjusted Syamlal-Obrien drag model [26]:

With wide use of the Syamlal-O'Brien drag model [23], people encountered the situation that some operating conditions are remarkably differed from the original experimental conditions. To extend its applicability, the Syamlal-O'Brien drag model [23] can be adjusted by matching the predicted minimum fluidization velocity with the experimental data and the constants c_1 and d_1 can be modified correspondingly:

Under the minimum fluidization conditions, the Eq. (9) can be rewritten as

$$\text{Re}_{mf} = \text{Re}_{mfs} \left[\frac{A + 0.06 B \text{Re}_{mfs}}{1 + 0.06 \text{Re}_{mfs}} \right] \tag{11}$$

The minimum fluidization condition and terminal settling condition can be considered the same for a single particle. Therefore, the terminal settling Reynolds number Re_{ts} is defined as

$$\text{Re}_{ts} = \left[\frac{\left(4.8^2 + 2.52\sqrt{4Ar/3} \right)^{0.5} - 4.8}{1.26} \right]^2 \tag{12}$$

where the Archimedes number is related to the drag coefficient and the Reynolds number by

$$Ar = \frac{\rho_l}{\mu_l^2} d_s^{\;3} \left(\rho_s - \rho_l \right) g \tag{13}$$

The minimum fluidization Reynolds number for multi-particle system Re_{mf} can be determined by the experimental measuring data. Furthermore, the drag coefficient and velocity-voidage correlation are the same as those in the Syamlal-O'Brien drag model [23] and the relationship between coefficient c_1 and d_1 is defined as follow to ensure the continuity of B.

$$d_1 = 1.28 + \frac{\log_{10}^{\;c1}}{\log_{10}^{\;0.85}} \tag{14}$$

For most cases, once the particle properties and the minimum fluidization velocity are known, c_1 and d_1 can be determined.

Irregular particle drag model:

The drag force between the liquid and solid is mainly depended on the local slip velocity, bed voidage, liquid properties, and solid properties, including particle density, size, and shape. However, the adjusted Syamlal O'Brien drag model [26] is derived based on

spherical particles, it is essential to take the sphericity into consideration for the irregular particle cases.

Since the Syamlal-O'Brien drag model [13] is based on the single particle drag model and the velocity-voidage function for spherical particles, the idea of modification is to replace them by the correlations for irregular particles.

The shape factor and single non-spherical particle drag coefficient proposed by Haider and Levenspiel [27] are employed in this research.

$$C_D = \frac{24}{\mathrm{Re}}\left[1+\left\{8.1716\exp\left(-4.0655\psi\right)\right\}\times\mathrm{Re}^{(0.0964+0.5565\psi)}\right]+\frac{73.69\,\mathrm{Re}\exp\left(-5.0748\psi\right)}{\mathrm{Re}+5.378\exp\left(6.2122\psi\right)} \quad (15)$$

The shape factor $\psi = \dfrac{s}{S}$, where s is the surface area of a sphere having the same volume as the irregular particle, and S is the actual surface area of the irregular particle [28].

The correlation for the velocity-voidage function, which is a function of the shape factor, is from Cleasby and Fan [29].

$$V_r = \frac{U}{U_t} = \varepsilon^{n-1}$$

where $n = n_{sperical}\times\left(\psi\right)^{\gamma}$ and $\gamma = -2.9237\,\mathrm{Re}t^{-0.363}\left(\psi\right)^{0.884}$. The $n_{spherical}$ is the "n" value form RZ equation [30].

$$\begin{cases} n_{sperical} = 4.65+20d\,/\,D & \mathrm{Re}t \le 0.2 \\ n_{sperical} = (4.4+18d\,/\,D)\,\mathrm{Re}t^{-0.03} & 0.2 < \mathrm{Re}t \le 1 \\ n_{sperical} = (4.4+18d\,/\,d)\,\mathrm{Re}t & 1 < \mathrm{Re}t \le 200 \\ n_{sperical} = 4.4\,\mathrm{Re}t^{-0.1} & 200 < \mathrm{Re}t \le 500 \\ n_{sperical} = 2.4 & \mathrm{Re}t > 500 \end{cases} \quad (16)$$

Therefore, by applying Eq. (5), the drag coefficient for irregular multi-particle systems can be obtained.

$$C_D = \frac{24}{\mathrm{Re}\,Vr}\left\{1+\left[8.1716\exp(-4.0655\psi)\right]\times\left(\frac{\mathrm{Re}}{Vr}\right)^{0.0964+0.5565\psi}\right\}+\frac{73.69\,\mathrm{Re}\exp(-5.0748\psi)}{Vr^2\,\mathrm{Re}+5.378Vr^3\exp(6.2122\psi)}$$

$$(17)$$

3.3.3   Near wall treatments

By referring the investigations of different near wall treatments in chapter 2, the Menter-Lechner [31] provides the best core-annulus structure which presents higher solids concentration at the near wall region while lower solids holdup at the central region. Therefore, in this study, the Menter-Lechner near wall treatment [31] is chosen for the simulations of all cases.

Menter-Lechner ε - Equation [31]:

To avoid the drawbacks of the enhanced wall treatment, such as mistreat low values of turbulence kinetic energy region at the near wall region, the errors with pressure gradient flows and the oscillating problem if a coarse first mesh with y+ near the switching locations. Menter-Lechner wall treatment adds a source term to the k-ε transport equation instead of using ε and turbulent viscosity from separate equations.

3.4   Numerical methodology

To simulate the two-phase flows in the LSCFB shown in Fig 3.1, the riser is simplified to a 2D planar as shown in Fig 3.2 and the mesh information can be seen from Table 3.3. Due to the potential instantaneous non-axisymmetric flow structures within LSCFBs, the 2D planar mesh is created and the results are time averaged for 20s. At the inlet region, the mesh has been refined with an expand ratio of 1.05 to correctly represent the complex flow structures. As for the wall region, although the Y^+ independent Menter-Lechner near wall treatment [31] is used, the $Y^+ \leq 1$ condition is still applied to resolve the near wall region and the mesh has an expand ratio of 1.05 as well.

The boundary conditions for the simulation can be seen in Fig 3.2. At the inlet, which is located at the bottom of the riser, both liquid and particles are of uniform velocities. At the outlet, outflow condition is used due to the fully developed flow condition at the outlet. On

the wall, the no-slip condition is used for the liquid phase, and partial slip Johnson and Jackson [32] boundary condition with the specularity coefficient of 0.0005 and the particle-wall restitution coefficient of 0.95 are used for the solid phase.

For the liquid phase, the dispersed k-ε turbulence model is used. For solid phase, the kinetic theory of granular phase is employed and the particle-particle collision restitution coefficient is set as 0.95. As for the interactions between phases, the adjusted Syamlal O'Brien drag model [26] and irregular particle drag model are used for spherical and irregular particles, respectively. Since the sphericity for irregular plastic beads [9] is 0.7, the parameters for irregular particle drag model can be determined, and the irregular particle drag model is compiled into Fluent by User Defined Function (UDF), the UDF file can be seen from Appendix B.

The phase coupled SIMPLE scheme is used for the pressure-velocity coupling, the power law is chosen to discretize the convection terms for the k-ε turbulence model and granular temperature while the QUICK is chosen for mass and momentum governing equations. The time step size is set as 1×10^{-04} s and the convergence criteria is set as 5×10^{-05}.
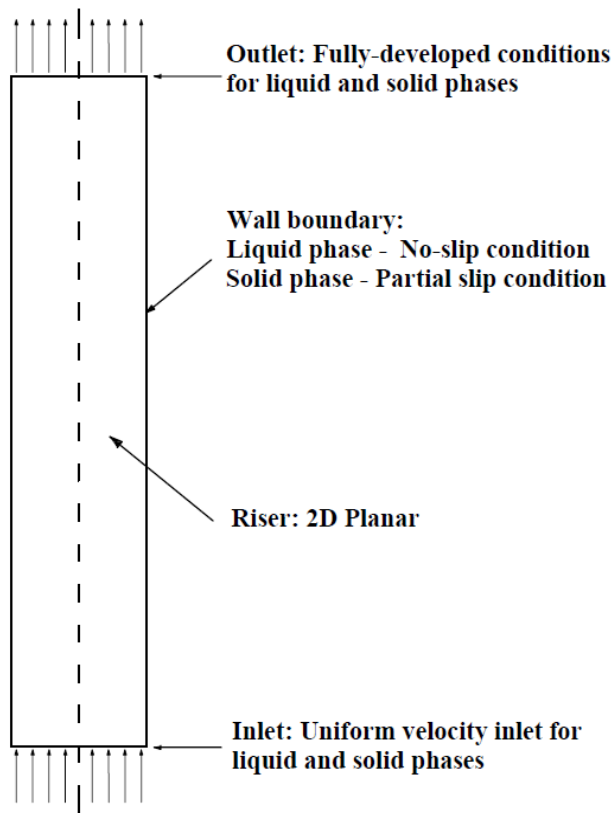
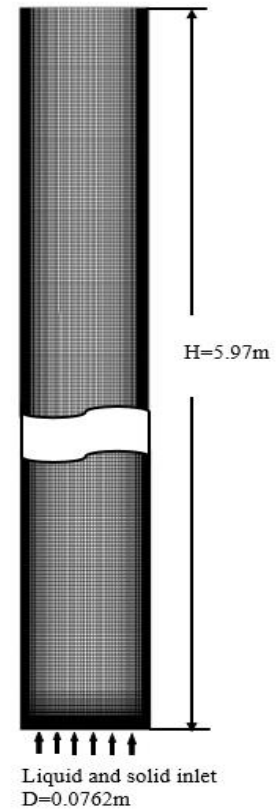**Figure 3.2: Schematics of the LSCFB riser**

Figure 3.3: Diagram of the mesh created for simulations

Table 3.3 Mesh information for different operating conditions

Parameters	Domain size (m)	Number of grids	Wall spacing for first grid (width and length, m)	Increasing ratio along radius	Increasing ratio along axis	Maximum aspect ratio
U_l=11.2cm/s U_s=0.747, 0.95, 1.121cm/s	0.0762×5.97	100×2500	0.00015	1.05	1.05	16.73
U_l=35cm/s U_s=1.193, 1.718cm/s	0.0381×5.97	100×2500	0.000052	1.05	1.05	41.12
U_l=28cm/s U_s=0.4cm/s	0.0762×5.2	100×2500	0.000064	1.05	1.05	29.48
U_l=8.4cm/s U_s=0.95cm/s	0.0762×5.77	85×2500	0.000196	1.1	1.1	10.45
U_l=22.4cm/s U_s=0.95cm/s	0.0762×5.77	80×2500	0.000079	1.15	1.15	29.89

3.5   Results and discussion

The detailed numerical studies on different drag models, near wall treatments and boundary conditions are carried out in the previous chapter. Therefore, in this chapter, the proposed numerical models described in the previous chapter are employed to predict the flow field and hydrodynamics for a LSCFB riser under different operating conditions. The numerical results are compared with the experimental data. The general hydrodynamics and flow patterns in the LSCFBs are studied.

3.5.1   General hydrodynamics of LSCFB

The LSCFB riser under the operating condition of U_l=22.4 cm/s and U_s=0.95 cm/s is simulated and the general hydrodynamic behaviors are discussed in this section. The cross-sectional averaged solids velocity and concentration are shown in Figs 3.4 and 3.5, respectively.
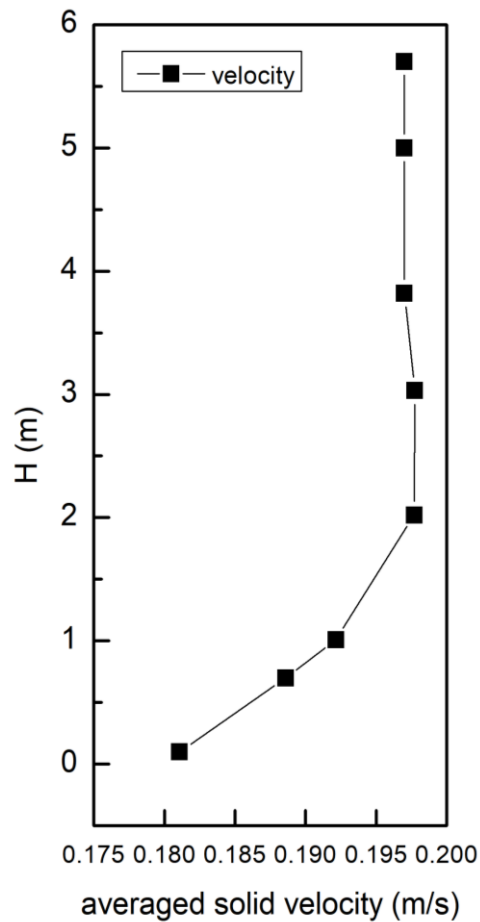
Figure 3.4: Axial distribution of the cross-sectional averaged solids velocity
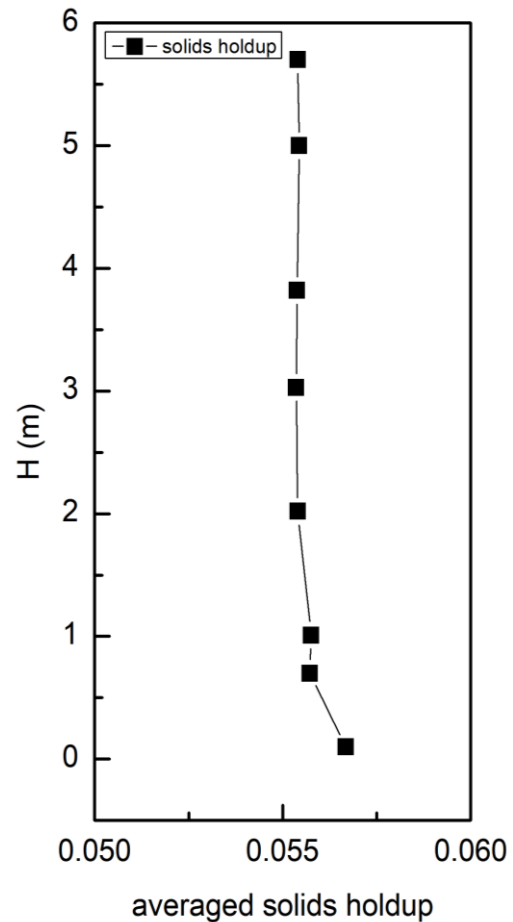

Figure 3.5: Axial distribution of the cross-sectional averaged solids holdup

It can be seen in Fig 3.4 the averaged solids velocity increases first and then remain constant along the axis of the bed, which indicates with the lift effect due to the velocity difference between liquid and solid phase, the solids will go through the acceleration process until the slip velocity remain unchanged. The same phenomenon can be seen in Fig 3.5 that the averaged solids concentration along the axis decreases during the acceleration process then remain uniform. However, the non-uniformity for the averaged solid concentration along axis is small, which matches with the previous experimental observations from Liang et al. [3] and Zheng [4] for lighter particles, such as glass beads, the axial profiles can be considered as uniform throughout the whole riser in LSCFBs.
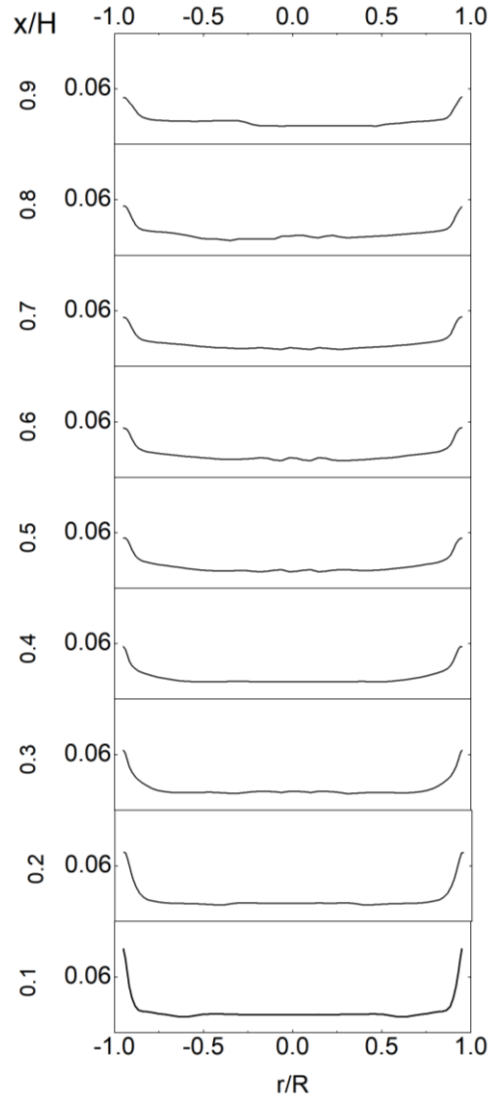
Figure 3.6: Radial distributions of the solids holdup at different axial locations

The solids holdup distributions along the radial direction at different bed heights are presented in Fig 3.6 and the comparison with the experimental data is given in Fig 3.7. The radial non-uniformity, dense in the near wall region and dilute in the center, can be clearly observed for solids holdup at each bed height. This nonuniform phenomenon might be explained by the theory of momentum balance for particles in the bed. Due to the wall effect, the liquid velocity along the radial direction is higher in the center and lower near the wall, likewise, the particles will accelerate to the same velocity profile as the liquid. To maintain the momentum balance for the cross-sectional area, a net particle transfer from the central region to the wall region is formed. Therefore, results in the lower solids

concentration at the core region, increases towards to the wall and reaches the maximum value near the wall as shown in Figs 3.6 and 3.7. Besides, it is shown the radial non-uniformity is higher at the lower part of the bed and decreases at higher part of the bed, which was also observed by Razzak [5], indicating the more uniform radial profiles of the solids holdup at the top of the riser due to the well-established flow structures. Furthermore, it is clear from the Fig 3.7 that the agreement between numerical predictions and experimental data is good for the solids holdup.
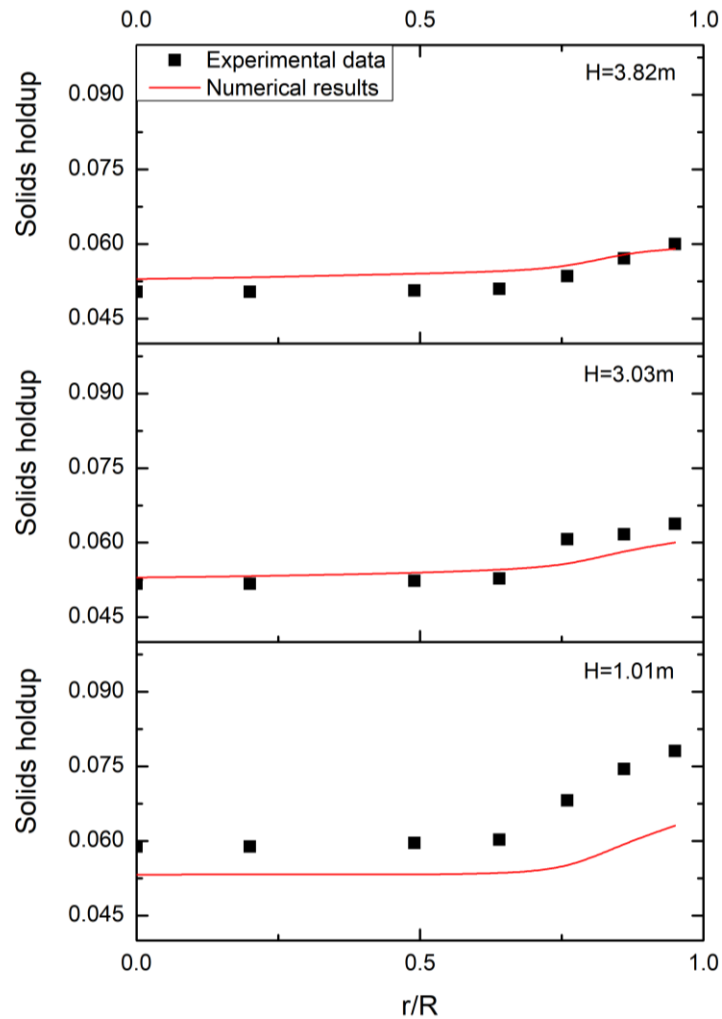

Figure 3.7: Comparisons of the radial distributions of the solids holdup between the experimental and numerical results at different axial locations under U_l= 22.4cm/s and U_s= 0.95cm/s
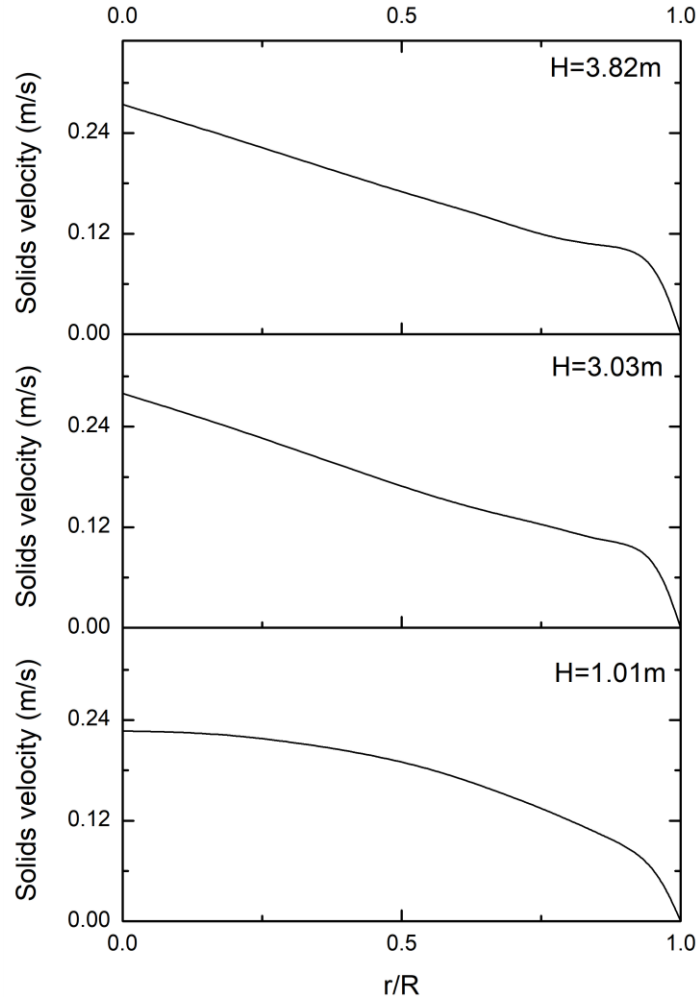
Figure 3.8: Radial distributions of the solids velocity at different axial locations under U_l= 22.4cm/s and U_s= 0.95cm/s

The distribution of the solids velocity along the radial direction at different bed heights is shown in Fig 3.8. Associated with the solids holdup distribution along the radial direction, the solids velocity is higher at the core region and decreases due to the shear effects near the wall.

3.5.2   Effects of U_s under the same U_l

The influence of the superficial solid velocity under the same superficial liquid velocity is investigated in this section. The simulations using two groups of operating conditions from Razzak [5] are carried out. The average solids holdup along the axial direction for glass beads under U_l=11.2 cm/s and 35cm/s at different solids flow rates are shown in Fig 3.9.
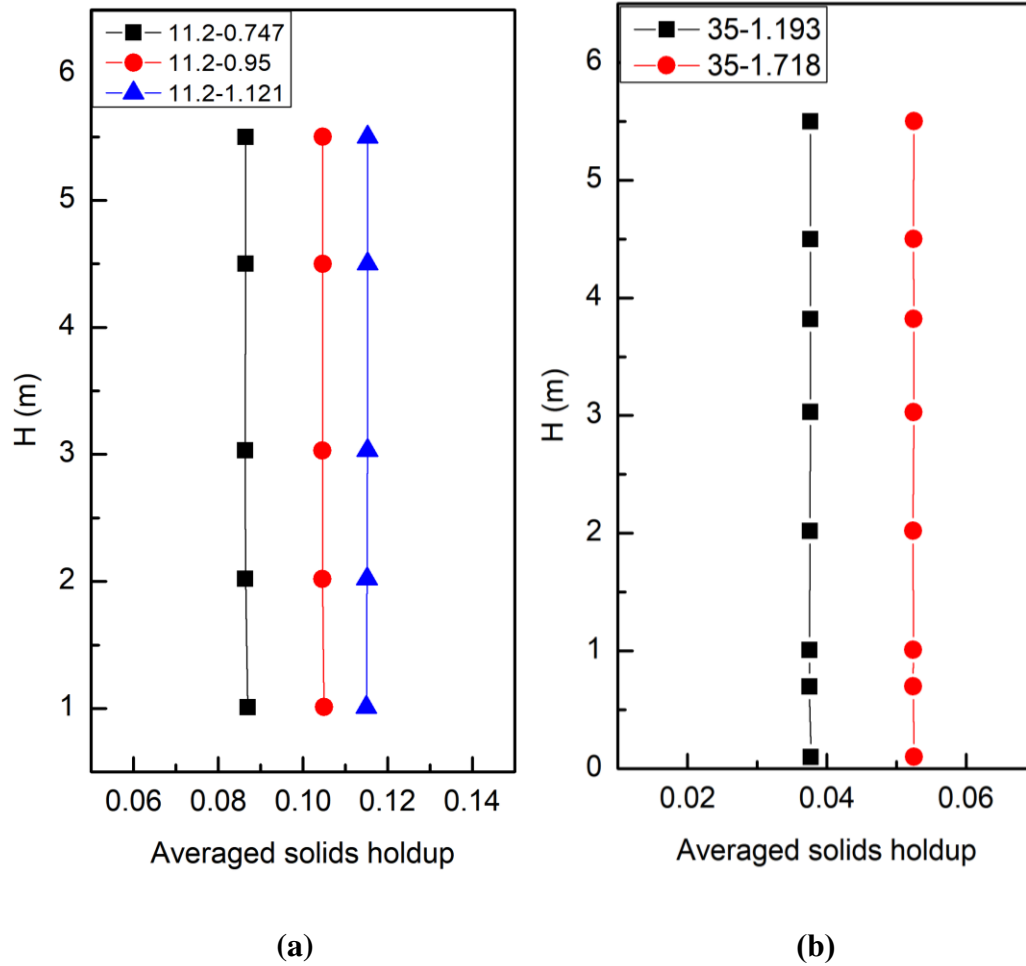
Figure 3.9: Comparison of the axial distributions of the cross-sectional averaged solids holdup under different operating conditions

(a) U_l=11.2cm/s and U_s=0.747,0.95 and 1.121cm/s

(b) U_l=35cm/s and U_s=1.193 and 1.718 cm/s

Same as the phenomenon observed both in the experiments and previous numerical simulations, after the superficial liquid velocity reaches the critical transition velocity, the fluidized bed system enters circulating fluidization regime. It is widely observed the axial profiles are uniform for lighter particle systems, except for the locations close to the inlet of the bed, where the solid concentrations are higher before the flow reaches fully developed. At the same time, it is clear that by increasing the solids flow rate, the overall bed solids holdup will increase since more particles are introduced into the bed.
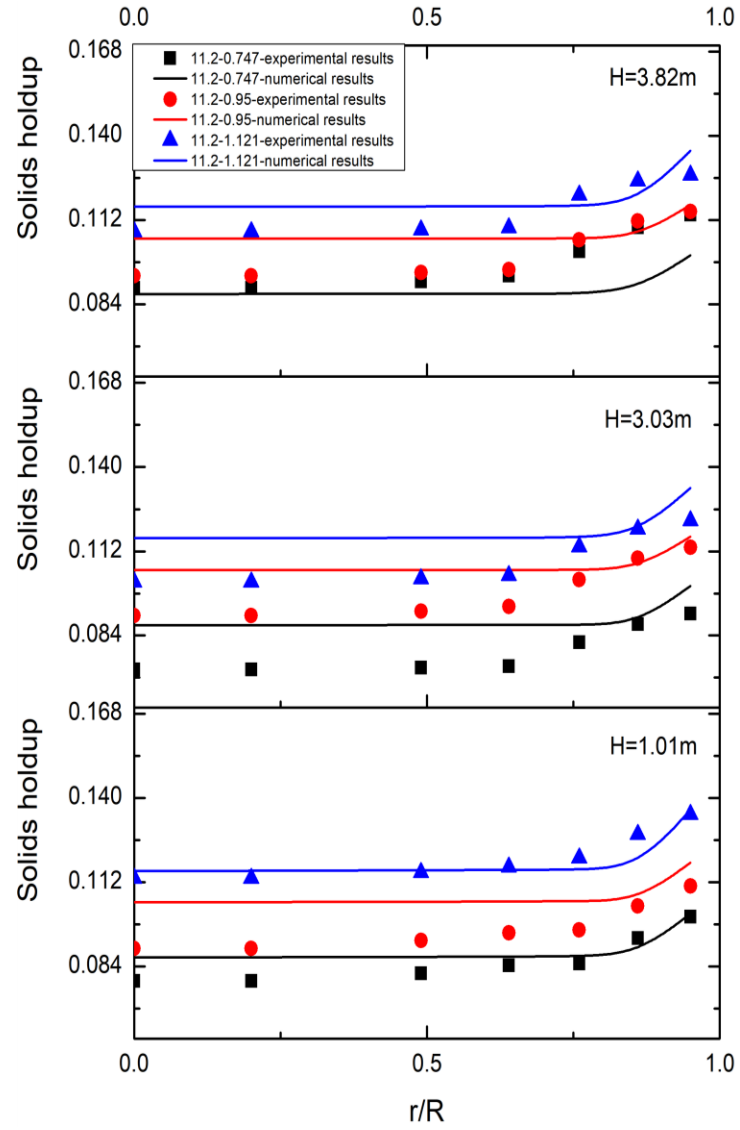
Figure 3.10: Comparisons of the radial distributions of the solids holdup between the experimental and numerical results at different axial locations under U$_l$=11.2cm/s and U$_s$=0.747,0.951 and 1.121cm/s
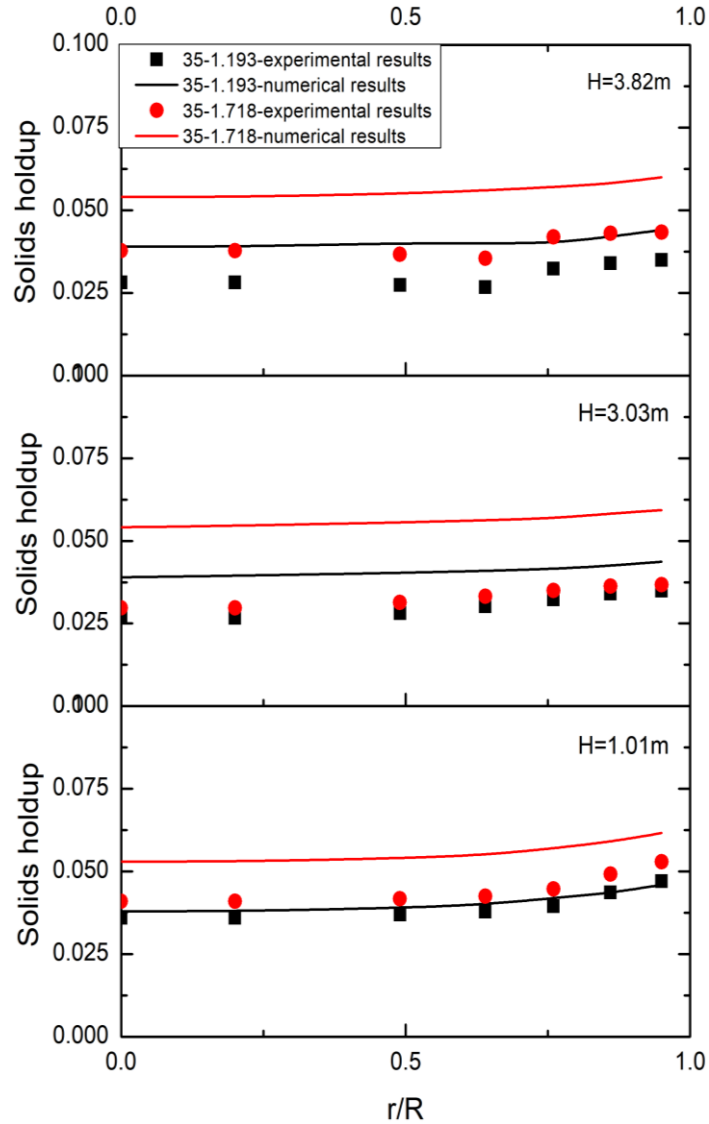
Figure 3.11: Comparisons of the radial distributions of the solids holdup between the experimental and numerical results at different axial locations under U_l=35cm/s and U_s=1.193 and 1.718 cm/s

The radial solids holdup comparisons between numerical predictions and experimental data for two groups of operating conditions are shown in Figs 3.10 and 3.11. For both operating conditions, the numerical model can successfully represent the flow structures in the LSCFB riser and the agreements with the experimental data are good. The radial non-uniformity appears in both operating conditions at each bed height, which reflects the general radial profiles for LSCFB risers. However, it can be observed that with the increase

in the solids flow rate, the radial non-uniformity increases as well. This is expected due to the momentum balance for the particles in the riser. When the solid circulation rate increases, more particles are fluidized in the riser and distributed as less particles at the central region and more particles at the near wall region as well, which results in a steeper solids holdup profile.
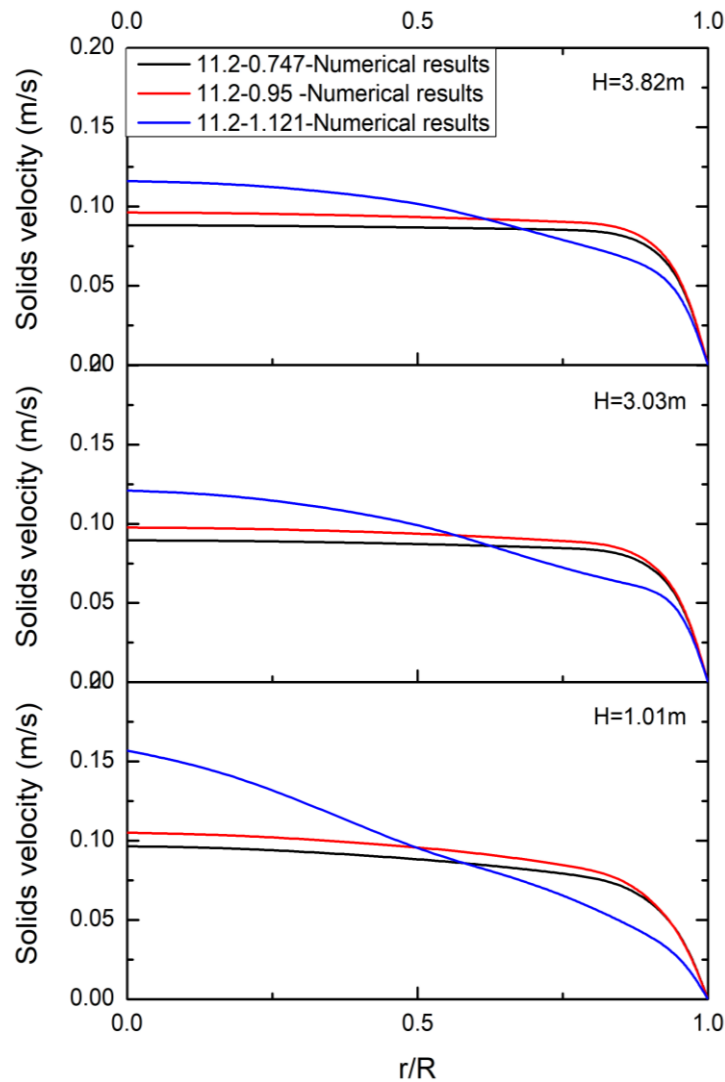

Figure 3.11: Comparison of the radial distributions of the solids velocity at different axial locations under U_l=11.2cm/s and U_s=0.747,0.951,1.121cm/s
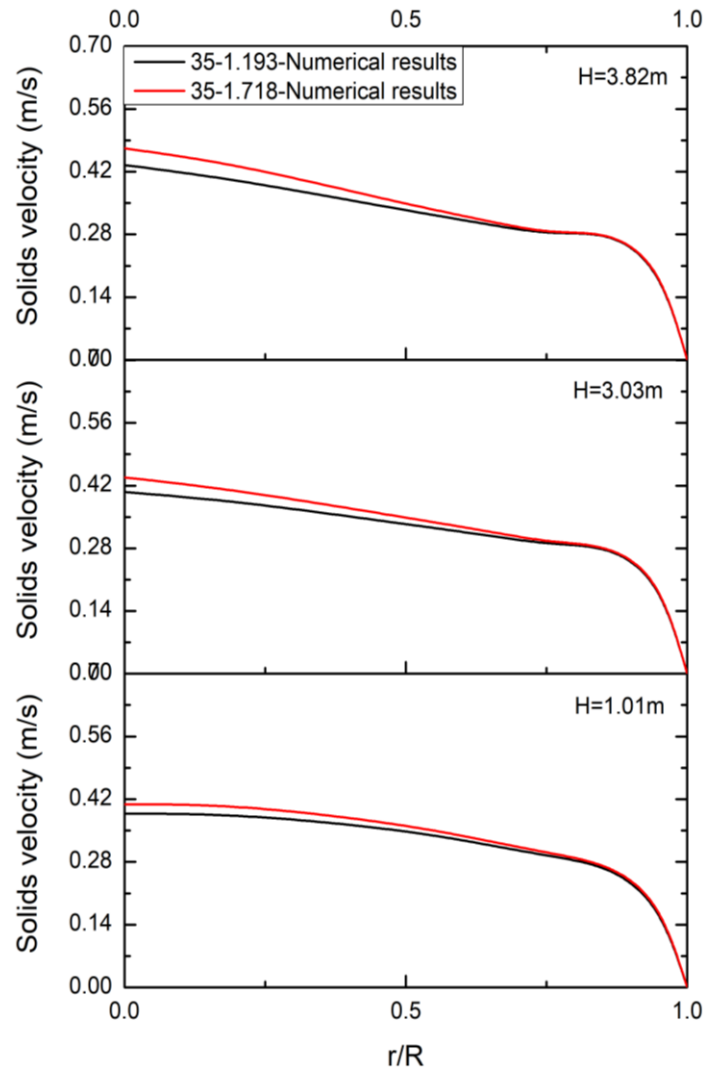
Figure 3.12: Comparison of the radial distributions of the solids velocity at different axial locations under U_l=35cm/s and U_s=1.193, 1.718 cm/s

The solids velocity distributions along the radial direction are presented in Figs 3.12 and 3.13 for the two groups of operating conditions. The solid velocity is higher at the center and lower at the near wall region of the bed for all operating conditions. As described before, due to the shear effect of the wall, both liquid and the accelerated particles will have this velocity distribution in the radial direction. Besides, it can be seen with the increase in the solids flow rate, the solids velocity distribution in the radial direction has a steeper profile, which is reasonable since the solids holdup radial non-uniformity increases with the increase in the solids flow rate.

3.5.3   Effects of U_l under the same U_s

The influence of the superficial liquid velocity under the same superficial solid velocity is investigated in this section. The simulations for one group of operating conditions from Razzak [5] are carried out. The experimental data for U_s=0.95cm/s and U_l=8.4cm/s is not available, therefore, the numerical results are discussed with the expected hydrodynamic behaviors. The axial and radial solid profiles for glass beads under U_s=0.95cm/s and different liquid flow rates are shown in Fig 3.14 and 3.15.
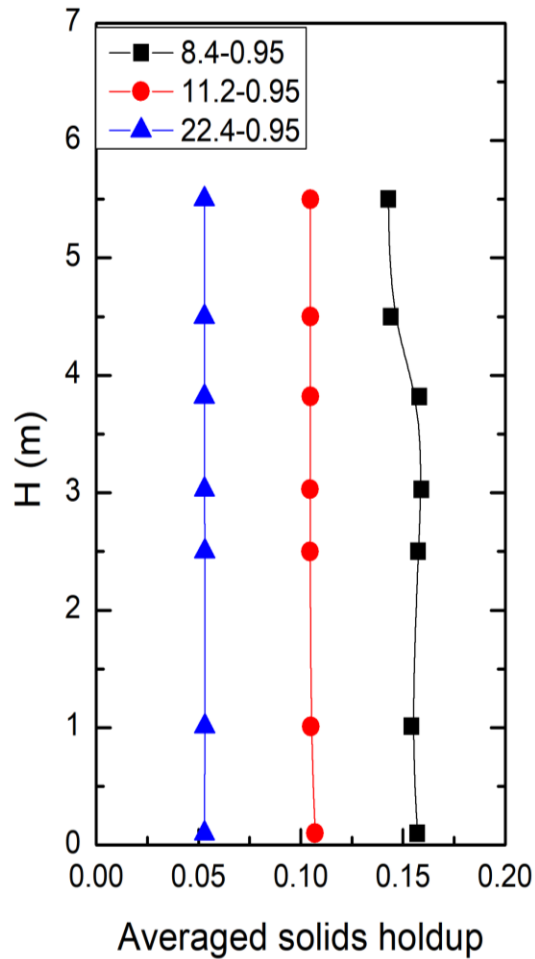

Figure 3.13: Axial distributions of the cross-sectional averaged solids holdup under U_s=0.95 cm/s while U_l=8.4, 11.2, 22.4 cm/s
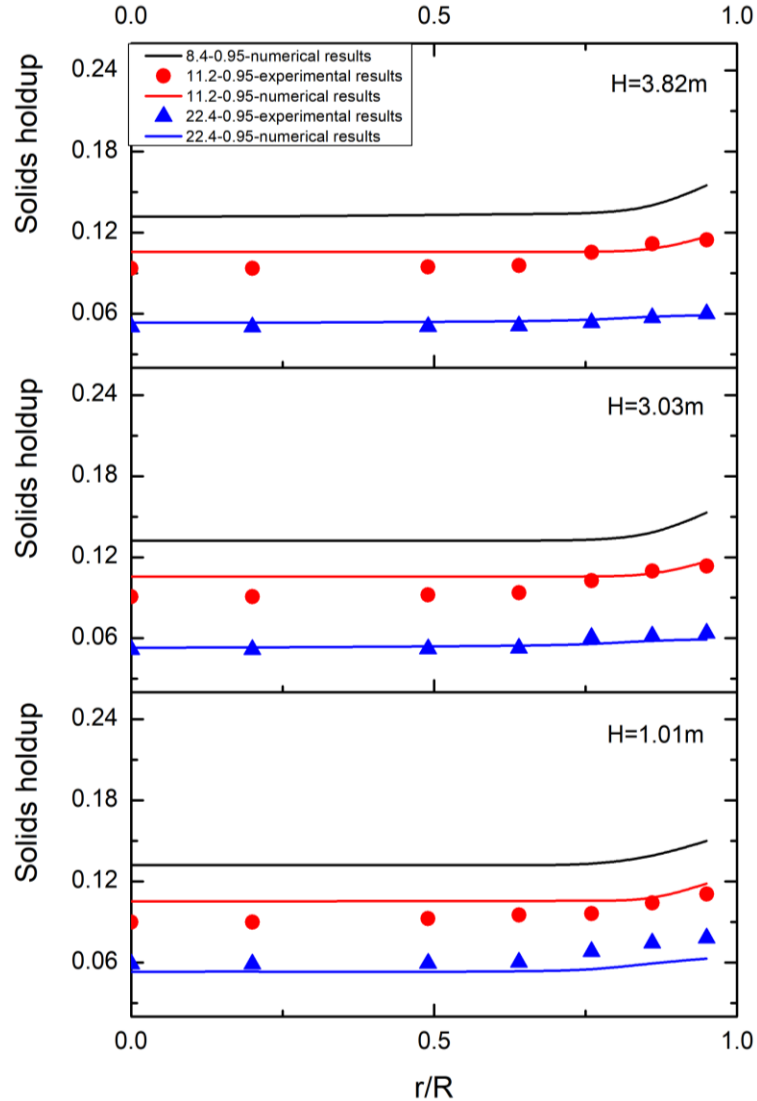
Figure 3.14: Comparisons of the radial distributions of the solids holdup between experimental and numerical results at different axial locations under U_s=0.95 cm/s, and U_l= 8.4, 11.2 and 22.4 cm/s

It is clearly from Fig 3.14 the cross-sectional averaged solids holdup along the axial direction is uniform for all operating conditions. For a higher liquid flow rate under the same solids flow rate, more particles can be carried out of riser, thus, the averaged solids holdup is lower.

As for the solids holdup profile along the radial direction, it can be seen from Fig 3.15 the radial non-uniformity is clear at each bed height under all operating conditions, which

indicates the lower solids velocity at the wall region due to the shear effects of the wall. As discussed before, increasing the superficial solid velocity under the same liquid flow rate results in a steeper radial solids holdup distribution. Correspondingly, increasing the superficial liquid velocity under the same solids circulation rate will lead to the opposite trend. As shown in Fig 3.15, there is not much change by increasing from U_l=8.4 cm/s to U_l=11.2 cm/s. However, the radial non-uniformity flattens by further increasing U_l to 22.4 cm/s, which indicates the bed is more homogeneous under a higher liquid flow rate. This phenomenon is also observed by Zheng [8] and Liang and Zhu [6]. Within the circulating fluidization regime, the nonuniformity might even increase with the increase in the superficial liquid velocity. Further increasing U_l will lead to the nonuniformity decreases significantly, which indicates the fluidized bed might begin the transition from the fully developed circulating fluidization regime to the dilute transport regime [6].

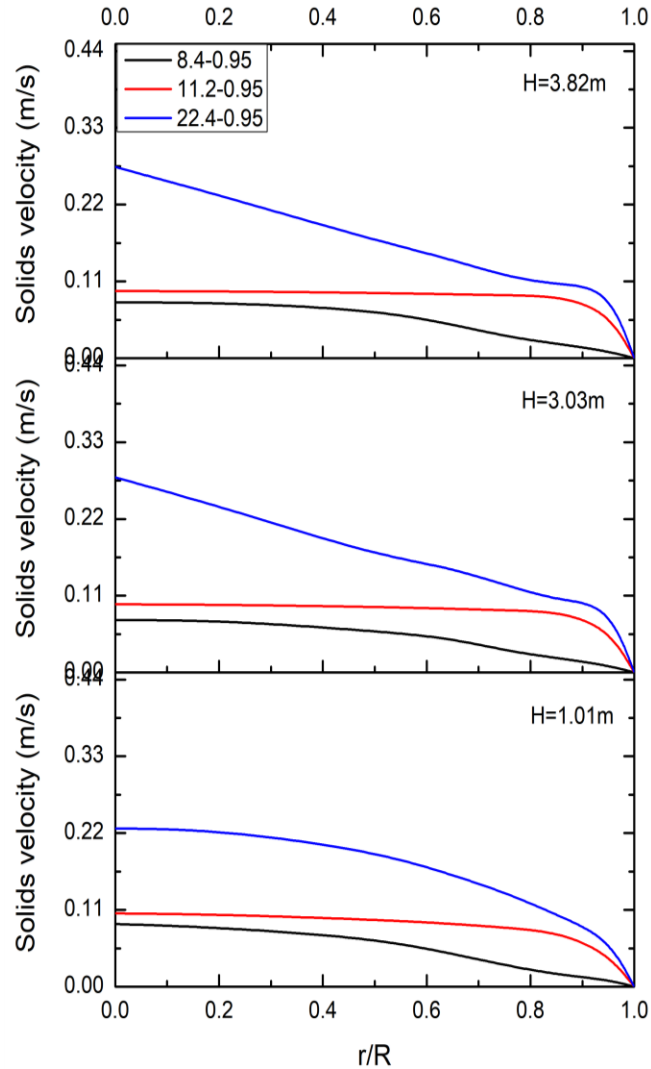**Figure 3.15: Radial distributions of the solids velocity at different axial locations under U_s=0.95 cm/s, and U_l= 8.4, 11.2 and 22.4 cm/s**

The solids velocity profile along the radial direction is presented in Fig 3.16. All the velocity profiles show higher velocity at the central region and low velocity at the near wall region. Furthermore, it can be seen the radial non-uniformity on velocity distribution will increase with the increase in the liquid flow rate, which is reasonable due to the no slip condition for liquid at the wall. A higher superficial liquid velocity leads to a steeper decrease trend in the velocity distribution along the radial direction to ensure the lowest liquid velocity at the wall.

3.5.4 Effects of particle density for irregular particles

The influence of particle density on the hydrodynamics for LSCFB riser is studied and the results are compared with the experimental data from Sang [9]. The LSCFB riser using plastic beads with diameter 0.58mm, sphericity 0.7, density 1520kg/m^3 and 1330kg/m^3 under operating condition as U_l=28cm/s and U_s= 0.4cm/s are investigated.
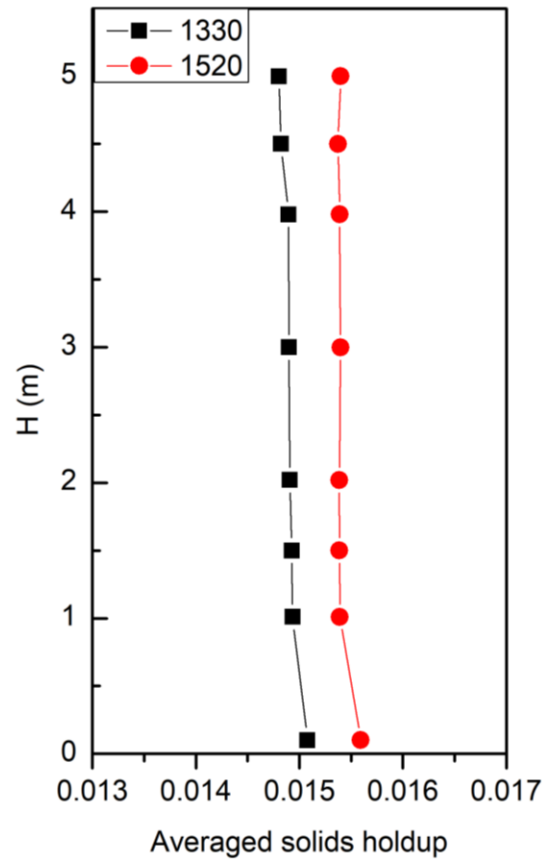

Figure 3.16: Axial distributions of the cross-sectional averaged solids holdup for
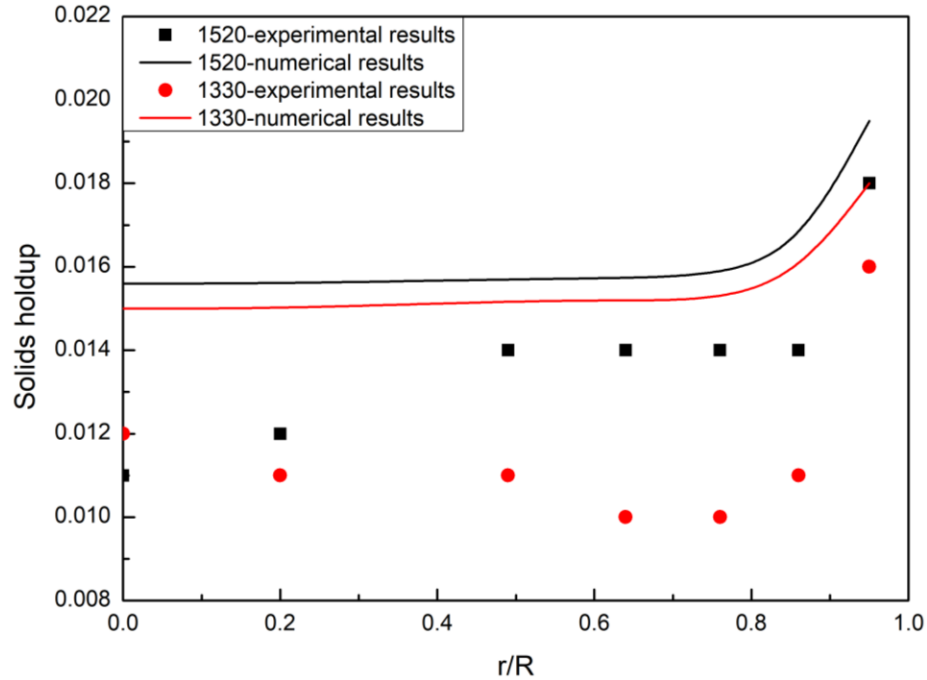
ρ_p **=1330kg/m3, 1520kg/m3**

Figure 3.17: Comparisons of the radial distributions of the solids holdup between experimental and numerical results at H=3.98m for ρ_p =1330kg/m³ and 1520kg/m³

The axial cross-sectional averages solids holdup is shown in Fig 3.17. The solids acceleration process can be clearly seen for both operating conditions. Since the particles are feed into the riser at the bottom, they will go through the process that being accelerated by the up flowing liquid until the velocity reaches unchanged. Therefore, with the increase in the solids velocity in the accelerating region, the average solids holdup will decrease. After reaching the state where the drag force balances the gravitational force, the velocity and solids holdup remain constant.

The radial solids holdup profile at H=3.98m for two different particles are shown in Fig 3.18. Both numerical predictions and experimental data show radial non-uniformity where higher solids concentration at the wall and dilute in the central region. However, the experimental solids holdup profile for irregular plastic beads is not as uniform as spherical glass beads one. It might because the irregular particles result in a more chaotic flow field. Besides, it is noticed from both Figs 3.17 and 3.18 that by decreasing the particle density, both axial and radial solids holdup decrease, which is expected since the lower particle

density leads to lower gravity. So, it is easier to fluidize the particles and entrain out of the bed, which results in a higher overall bed voidage.

3.6 Conclusions

A numerical study has been carried out in this work on the hydrodynamic behaviors of the LSCFB riser. The predictions for different operating conditions are compared with previous experimental observations. The hydrodynamics for the LSCFB riser under all operating conditions have similar features. The radial flow structures at different bed heights are identical and the cross-sectional averaged solids concentrations are almost the same along the axis of the bed, which indicates the uniform axial flow structures for LSCFB risers. For the flow structures in the radial direction, due to the shear effect of the wall, the solids concentration profile is not uniform in the radial direction. It is lower and almost uniform at the core region and higher near the wall, which is opposite to the velocity distribution. The operating condition under U_l=11.2cm/s and U_s=0.95cm/s has been chosen as anchoring point to investigate the influence of different superficial liquid and solid velocity on the hydrodynamics. The results show that with the increase in the solid flow rate, both average solids holdup and radial non-uniformity increase. However, with the increase in the liquid flow rate, the average solids holdup decreases and the radial non-uniformity decreases indicating it might transfer to the dilute transport regime. The particle density is also a crucial factor affects the flow structures. With higher particle density under same operating conditions, the solids holdup increases. All in all, despite there is non-uniformity exists, both the axial and radial flow structures in the LSCFB riser are more uniform than in the GSCFB.

References

[1] A. Atta, S.A. Razzak, K.D.P. Nigam, J.X. Zhu, (Gas)–liquid–solid circulating fluidized bed reactors: characteristics and applications, Ind. Eng. Chem. Res. 48 (2009) 7876–7892.

[2] Couderc J.-P., 1985, Incipient fluidization and particulate systems,' Chapter 1 in Fluidization, 2nd edn., eds. J. F. Davidson, R. Clift and D. Harrison, Academic Press, London, pp. 1-46

[3] Liang, W. G., Zhang, S. L., Zhu, J. X., Yu, Z. Q., Jin, Y., & Wang, Z. W. (1997). Flow characteristics of the liquid-solid circulating fluidized bed. Powder Tech., 90, 95–102.

[4] Zheng Y. Flow structure in a liquid-solids circulating fluidized bed [dissertation]. London, Ont: Faculty of Graduate Studies, University of Western Ontario; 1999.

[5] Razzak, S.A. 2009, Hydrodynamic studies in liquid-solid and gas-liquid-solid circulating fluidized beds, The University of Western Ontario (Canada).

[6] Liang, W.-G., Y. Zhang, J. -X. Zhu, Y. Jin, Z. -W, Wang, Radial non uniformity of flow structure in a liquid-solid circulating fluidized bed, Chem. Eng. Sci., 1996, 77, 2001-2010.

[7] Roy S., Chen J.-W., Kunar S.B., Al-Dahhan M.H. and Dudukovic M.P., 1997, Tomographie and particle tracking studies in a liquid-solid riser, Ind. Eng. Chem. Res., 36,46664669-

[8] Zheng, Y., Zhu, J. X., Marwaha, N., & Bassi, A. S. (2002). Radial solid flow structure in a liquid-solid circulating fluidized bed. Chem Eng J., 88, 141–150.

[9] Sang L. Particle fluidization in upward and inverse liquid-solid circulating fluidized bed [dissertation]. London, Ont: School of Graduate and Postdoctoral Studies, University of Western Ontario; 2013.

[10] Wang, Wei, et al. "A review of multiscale CFD for gas–solid CFB modeling." International Journal of Multiphase Flow 36.2 (2010): 109-118.

[11] Hartge, Ernst-Ulrich, et al. "CFD-simulation of a circulating fluidized bed riser." Particuology 7.4 (2009): 283-296.

[12] Sinclair, J. L., and R. Jackson. "Gas-particle flow in a vertical pipe with particle-particle interactions." AIChE Journal 35.9 (1989): 1473-1486.

[13] Ding, Jianmin, and Dimitri Gidaspow. "A bubbling fluidization model using kinetic theory of granular flow." AIChE journal 36.4 (1990): 523-538.

[14] H. Enwald et al. Eulerian two phase flow theory applied to fluidization. International Journal of Multiphase Flow 22(1), pp. 2166. 1996. DOI: 10.1016/S0301-9322(96)90004X.

[15] Roy, S.,& Dudukovic, M. P. (2001). Flow Mapping and Modeling of Liquid-Solid Risers. Ind. Eng. Chem. Res., 40, 5440-5454.

[16] Y. Cheng and J. Zhu, "CFD Modelling and Simulation of Hydrodynamics in Liquid‑Solid Circulating Fluidized Beds," The Canadian Journal of Chemical Engineering, vol. 83, pp. 177-185, 2005.

[17] J. T. Cornelissen et al, "CFD modelling of a liquid–solid fluidized bed," Chemical Engineering Science, vol. 62, pp. 6334-6348, 2007.

[18] Dadashi A, Zhu J, Zhang C. A computational fluid dynamics study on the flow field in a liquid-solid circulating fluidized bed riser. POWDER TECHNOLOGY. 2014;260:528.

[19] Lun, C.K.K., Savage, S.B., Jeffrey, D.J. and Chepurniy, N., 1984, Kinetic theories for granular flow: inelastic particles in Couette flow and slightly inelastic particles in a general flow field, J Fluid Mech, 140: 223.

[20] Gidaspow, D., 1994, Multiphase Flow and Fluidization: Continuum and Kinetic Theory Descriptions, Academy, Boston, MA.

[21] Syamlal, M., W. Rogers and T. J. O'Brien, "MFIX Documentation Theory Guide," U.S. Department of Energy Office of Fossil Energy Morgantown Energy Technology Center, Morgantown, WV (1993).

[22] D.G. Schaeffer, Instability in the evolution equations describing incompressible granular flow, J. Diff. Eqs. 66 (1987) 19‑50.

[23] M. Syamlal and T.J. O'Brien. The derivation of a drag coefficient formula from velocity-voidage correlations. Technical Note, U.S. Department of energy, Office of Fossil Energy, NETL, Morgantown, WV, April 1987.

[24] J. M. Dalla Valle. Micromeritics. Pitman, London. 1948.

[25] Garside, J. and M. R. Al-Dibouni, "Velocity–Voidage Relationship for Fluidization and Sedimentation," Ind. Eng. Chem. Proc. Des. Dev. 16(2), 206–214 (1977).

[26] Syamlal, M., and O'Brien, T., 2003, "Fluid Dynamic Simulation of O3 Decomposition in a Bubbling Fluidized Bed," AIChE J., 49_11_, pp. 2793–2801.

[27] Haider A and Levenspiel O. Drag coefficient and terminal velocity of spherical and nonspherical particles. Powder Technol 1989; 58: 63–70.

[28] Wadell H (1933). Sphericity and Roundness of Rock Particles, J. Geol. 41 310-331.

[29] Cleasby, J. L. and Fan, K. S. Predicting fluidization and expansion of filter media. Journal of the Sanitary Engineering Division, American Society of Civil Engineers, 107 (1981), 455-471.

[30] Richardson JF, Zaki WN. Sedimentation and fluidization: Part I. Process Safety and Environmental Protection: Transactions of the Institution of Chemical Engineers, Part B. 1997;75: S82S100.

[31] Ansys Fluent. Fluent 16.0 User's Guide.

[32] P. C. Johnson and R. Jackson. "Frictional-Collisional Constitutive Relations for Granular Materials, with Application to Plane Shearing". J. Fluid Mech. 176. 67-93.1987.

Chapter 4

4 Conclusions and Recommendations

4.1 Conclusions

Liquid-solid fluidization has been extensively applied in various industrial processes such as the wastewater treatment and biochemical processes due to its unique liquid-solid contacting features. It is important to study the hydrodynamic behaviors of LSCFBs for the design and scale-up purposes. In this study, the evaluations of the CFD models are conducted to simulate the hydrodynamics of LSCFBs. A comprehensive investigation of the hydrodynamics under different operating conditions of the LSCFB is also carried out by employing the proposed CFD model.

The applicability of existing widely used drag models, the performance of near wall treatments for the liquid phase and the influence of boundary conditions for the solid phase are investigated. By comparing the numerical results with the experimental data, it is found the adjusted Syamlal O'Brien drag model provides a better overall agreement with the experimental data for the two-phase flows in LSCFBs with spherical particles and the Menter-Lechner near wall treatment can significantly improve the numerical solutions at the near wall region. In addition, by applying different specularity and restitution coefficients in the granular boundary condition, it is found the numerical results are insensitive to these coefficients within the elastic collision range. Furthermore, the effect of non-spherical particle on the performance of the LSCFB has been investigated. A more accurate drag model for irregular particles is proposed by replacing the single particle drag correlation and velocity-voidage function which are based on spherical particle systems by the irregular particle ones. Besides, the granular temperature is also studied.

The hydrodynamic behaviors of the LSCFB riser under different operating conditions, including the different superficial liquid velocities, superficial solid velocities and particle densities are studied. It is found that the flow patterns in LSCFBs under different operating conditions are similar and they are different from the conventional fluidized bed. It is also found that there is radial non-uniformity in the flow structure, with lower and uniform

solids concentration in the core region and higher in the near wall region. This non-uniformity can be observed at all bed heights under different operating conditions. As for the axial direction, the identical solids profiles at different bed heights and the same average solids holdup along the axis could be observed, indicating the uniform axial flow structures for LSCFBs. In addition, it is found the average solids holdup and radial non-uniformity increase with the increase in the superficial solid velocity, and decrease with the increase in superficial liquid velocity. Besides, the solids holdup decreases with the decrease in the particle density. However, all the flow distributions in the radial and axial directions in LSCFBs are more uniform than those in GSCFBs.

In conclusion, it is demonstrated that the numerical predictions from the proposed CFD model are reliable. It can become an effective tool to design and scale up the LSCFB system for industrial applications or to investigate the specific small-scale flow field of LSCFBs to have a better understanding of the complicated multi-phase flow fields.

4.2   Recommendations

This study provides comprehensive numerical results and systematic investigations on the hydrodynamic behaviors in LSCFBs. However, some aspects still need to be investigated in future works:

(1) The particle properties are significant factors affecting the hydrodynamics in LSCFBs. In this study, only two types of light particles with different densities are investigated. Therefore, more types of particles with wide range of densities and sizes are needed to investigate the effects of particle properties on the performance of LSCFBs.

(2) There are always reactions exist in LSCFBs for industrial applications, such as wastewater treatment and biochemical technology. Based on the hydrodynamic models, the reaction models, mass and heat transfer can be taken into consideration in further works.

(3) In this study, the effect of the structure of main and auxiliary liquid distributors at the inlet is ignored, which should be investigated in the future.

(4) Only two-phase fluidization is considered in this study. Based on the two-phase Eulerian-Eulerian model, the gas phase could be introduced for the simulation of Gas-Liquid-Solid Circulating Fluidized Bed (GLSCFB) in future works.

Appendices

Appendix A

The optical fiber probe system is used to measure the local solids concentration during the experimental studies by Razzak and Sang. It is approximately 4mm in diameter and consists of around 8000 emitting and receiving quartz fibers. The measuring principles of optical fiber is shown in Fig - A as below. It has an active measuring area approximately 1.5 mm^2 at the center of probe tip. Therefore, considering the potential experimental operating errors, we could obtain and average the data within 2mm as the value at a certain point and compare with experimental data.
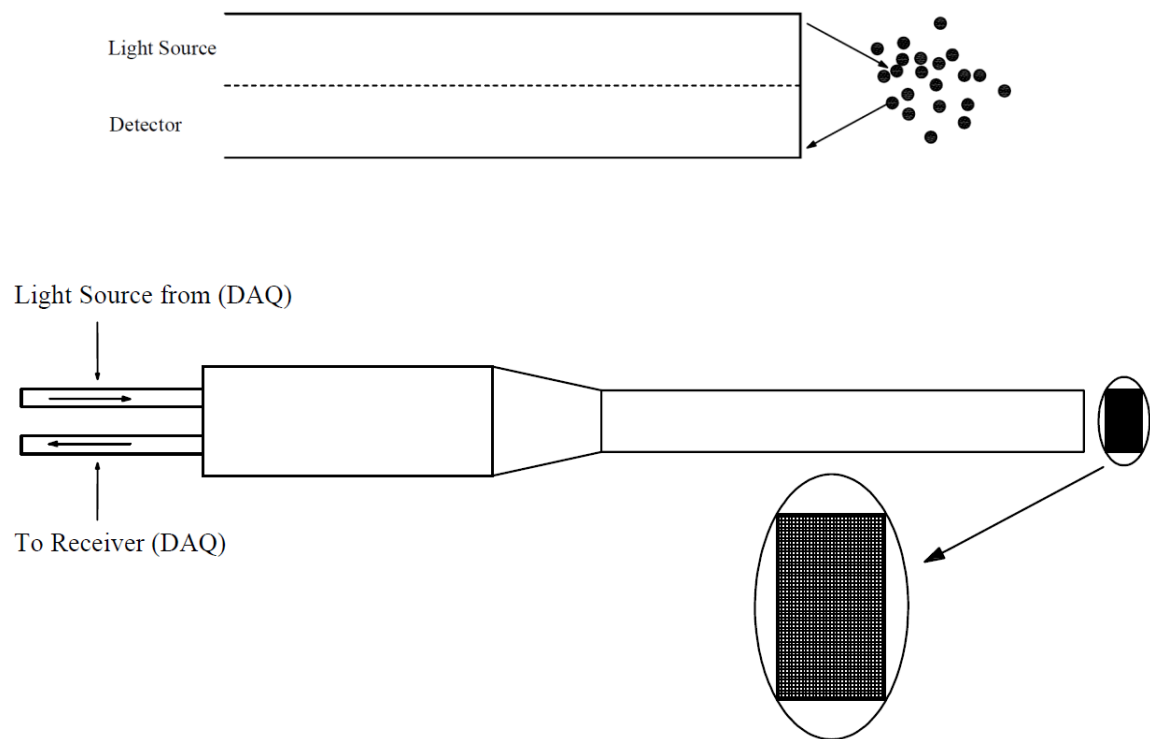


Figure - A: Schematic diagram of optical fiber probe system

As the shown in Fig - B is the plot of experimental data, numerical predictions and post process results. The data at certain location is obtained by time and space averaged within

10s and 2mm except for the last point near the wall. As we know, it'd be more difficult and more errors to determine the flow structures at the near wall region during the experimental studies, especially the area really close to wall, therefore, the last point is at the r/R=0.95. However, in the numerical predictions, at the wall region, it always presents a decreasing trend for solids holdup. Sometimes the inflection point is beyond 0.95 and it might also slightly before 0.95 sometimes. It might due to the collisions between the particles and the wall, makes the rebounded particles finally obtained the lowest solids velocity at the near wall region which results in the highest solids concentration. Besides, due to the finer mesh at the wall region and the relatively large particle size, Eulerian-Eulerian might give unrealistic results if the grid is not large enough for containing a few particles. Therefore, the highest point within the range of 2mm around r/R=0.95 is chosen for the last point and the other data from the near wall region is ignored.
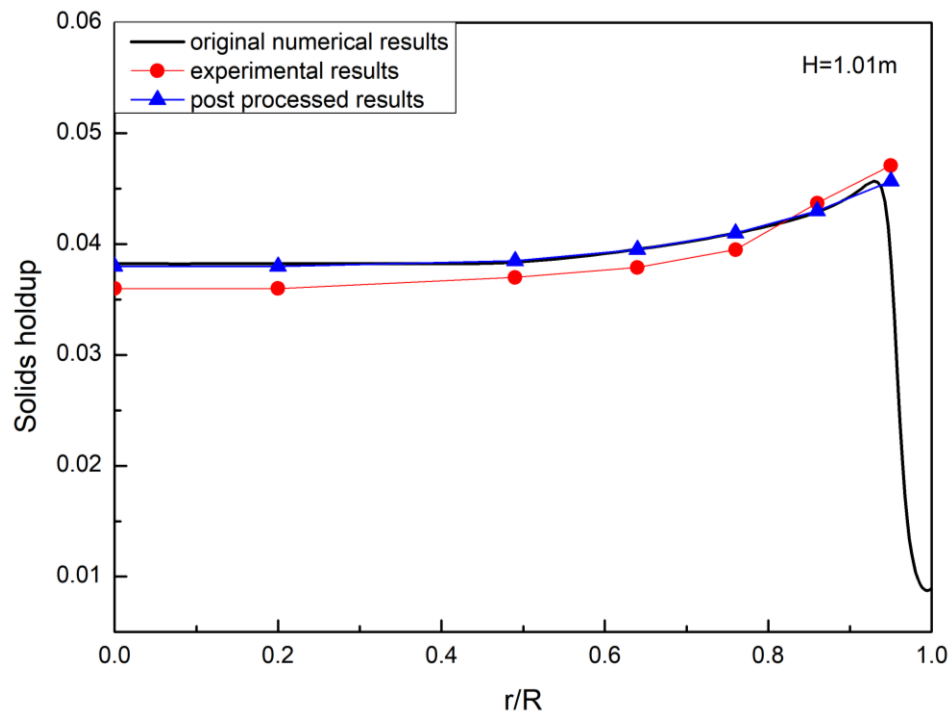
Figure - B: Radial solids holdup comparisons at H=1.01m under U_l =35cm/s, U_s =1.193cm/s

Appendix B

```
#include "udf.h"

#define pi 4.*atan(1.)
#define diam2 5.8e-4

DEFINE_EXCHANGE_PROPERTY(irregular_drag,cell,mix_thread,s_col,f_col)

{
Thread *thread_l, *thread_s;

real x_vel_l, x_vel_s, y_vel_l, y_vel_s, abs_v, slip_x, slip_y,
    rho_l, rho_s, mu_l, reyp, reys, vfac, corr, nn, nnn, vrn, cdls,
    void_l, void_s, k_l_s, vf;
int counter;

thread_l = THREAD_SUB_THREAD(mix_thread, s_col);
thread_s = THREAD_SUB_THREAD(mix_thread, f_col);

x_vel_l = C_U(cell, thread_l);
y_vel_l = C_V(cell, thread_l);
x_vel_s = C_U(cell, thread_s);
y_vel_s = C_V(cell, thread_s);
slip_x = x_vel_l - x_vel_s;
slip_y = y_vel_l - y_vel_s;
rho_l = C_R(cell, thread_l);
rho_s = C_R(cell, thread_s);
mu_l = C_MU_L(cell, thread_l);

abs_v = sqrt(slip_x*slip_x + slip_y*slip_y);

reyp = rho_l*abs_v*diam2/mu_l;

void_l = C_VOF(cell, thread_l);
void_s = C_VOF(cell, thread_s);

/*Calculating Richardson Zaki parameters for vr*/

vfac = 1.;
corr = 1.;
counter = 1;

while (corr>0.0001)
{
```

```
reys = reyp/(vfac+SMALL);

if (reys<=0.2)
nn = 4.798815789;

else if (reys>0.2&&reys<=1.)
nn = 4.483552632*pow(reys,-0.03);

else if (reys>1.&&reys<=200.)
nn = 4.587368421*pow(reys,-0.1);

else if (reys>200.&&reys<=500.)
nn = 4.45*pow(reys,-0.1);

else
nn = 2.4;

vrn = pow(void_l,nn-1.);
corr = sqrt((vfac-vrn)*(vfac-vrn));
vfac = vrn;

counter++;
}

nnn = nn * pow(0.7,-2.133042335*pow(reys,-0.363));
vf = pow (void_l,nnn-1.);

cdls =
(1.+0.4746463532*pow((reyp/(vf+SMALL)),0.48595))*24./(reyp*(vf+SMALL))+2.111
72913*reyp/((vf+SMALL)*(vf+SMALL)*reyp+416.0712659*(vf+SMALL)*(vf+SMAL
L)*(vf+SMALL));

k_l_s = 3.*rho_l*void_l*void_s*cdls*abs_v/(4.*diam2);

return k_l_s;
}
```

Curriculum Vitae

Name: Hao Luo

**Post-secondary   China University of Petroleum - Beijing
Education and   Changping, Beijing, China
Degrees:**   2011-2015 B.Eng.

                    The University of Western Ontario
                    London, Ontario, Canada
                    2015-2017 M.E, Sc.

**Honors and   Excellent student scholarship, China University of Petroleum
Awards:**   2011-2014

**Related Work   Teaching Assistant
Experience**   The University of Western Ontario
                    2016-2017

                    Research Assistant
                    The University of Western Ontario
                    2016-2017